HOKKAIDO UNIVERSITY

Title	Liquid-Phase Synthesis of Li2S-P2S5 Solid Electrolytes for All-Solid-State Batteries
Author(s)	Cecilia Marcela Calpa Ortiz
Degree Grantor	北海道大学
Degree Name	博士(工学)
Dissertation Number	甲第14015号
Issue Date	2020-03-25
DOI	https://doi.org/10.14943/doctoral.k14015
Doc URL	https://hdl.handle.net/2115/80088
Type	doctoral thesis
File Information	Cecilia_Marcela_Calpa_Ortiz.pdf

Hokkaido University Collection of Scholarly and Academic Papers : HUSCAP

Liquid-Phase Synthesis of Li_2S-P_2S_5 Solid Electrolytes for All-Solid-State Batteries

全固体電池用 Li_2S-P_2S_5 系固体電解質の液相合成

Cecilia Marcela Calpa Ortiz

Doctoral Thesis at Hokkaido University

January 2020

Table of contents

General introduction 1

PART I – Liquid-phase synthesis of sulfide solid electrolytes in the Li_2S-P_2S_5 system

Introduction 19

Experimental 24

Results and discussion 27

1. Preparation of Li_2S-P_2S_5 solid electrolytes by a liquid-phase process 27
    - Crystal phase and local structure 30
    - Morphology 33
    - Ionic conductivity 35
    - Discussion and summary 35
2. Crystallization process of Li_2S-P_2S_5 solid electrolytes through liquid-phase synthesis 38
    - Crystal phase and local structure 38
    - Morphology 43

Ionic conductivity 43

Discussion and summary 48

3. The search for the stoichiometry 50

Effect of the mass concentration 50

Effect of the ultrasonic irradiation 54

Discussion and summary 56

4. Formation mechanism of the $Li_7P_3S_{11}$ crystal phase through liquid-phase synthesis 59

Precursors solubility 61

Formation of the *meta*-thiodiphosphate $P_2S_6^{2-}$ anion 63

Formation of the *ortho*-thiophosphate PS_4^{3-} anion 72

Formation of the *pyro*-thiodiphosphate $P_2S_7^{4-}$ anion 74

Discussion and Summary 76

Summary 79

References 82

PART II – Application of $Li_7P_3S_{11}$ solid electrolyte as ionic conductive additive in the composite cathode of all-solid-state batteries

Introduction 91

Experimental 93

Results and discussion 97

1. $Li_7P_3S_{11}$ solid electrolyte prepared by mechanical milling and liquid-phase 97

Crystal phase and local structure 97

Morphology 99

Impedance analysis 101

Discussion and summary 101

2. Morphology of the electrode composites 104

3. Electrochemical characterization of the all-solid-state cells 106

Galvanostatic measurements 106

Impedance analysis 108

4. Electrochemical characterization under high charge-end voltage 112

Galvanostatic measurements 112

Impedance analysis 114

5. Study of the local structure stability of the solid electrolyte 117

Summary 120

References 122

General Conclusions 127

List of publications 131

To my Family

General introduction

Global warming and the growing energy demand require a shift in electricity production, from burning fuels to sustainable energy sources, such as wind, solar and tidal energy. Moving transportation toward electrical propulsion is also necessary to reduce the use of fossil fuels and the related carbon emissions. In this context, the development of good energy storage systems that enable the use of renewable energy and electric vehicles is essential to meet environmental constraints [1-3]. Lithium-ion batteries are promising candidates because they offer the high energy density required [4]. However, conventional Lithium-ion batteries possess safety issues concerns because of the use of flammable organic liquid electrolytes [5, 6]. All-solid-state lithium-ion batteries that use inorganic solid electrolytes instead of liquid electrolytes are expected to meet the energy density and safety required [7, 8].

Inorganic solid electrolytes with wider voltage windows make possible the operation of all-solid-state batteries with Lithium-metal [8-11], as well with high voltage [12, 13] and high-capacity [14, 15] cathode materials. On the other hand, the non-liquid nature of the electrolyte allows the stacking of the battery cells in a single package without an ionic short circuit [16]. These characteristics give the potential to the all-solid-state batteries to provide the high energy and power density required.

Li-ion conductive solid electrolytes are mainly classified into oxide-based and sulfide-based solid electrolytes. Oxide-based electrolytes such as perovskites [17], NASICON-type [18-21] and garnet-type [22-26] structures have high ionic

conductivities of around 10^{-3} Scm^{-1}; however, they require high temperature for the synthesis and subsequent co-sintering to achieve good contact with active materials in the composite cathode of the bulk-type all-solid-state batteries. Sulfide solid electrolytes in the Li_2S-GeS_2-P_2S_5 and Li_2S-P_2S_5 systems, such as $Li_{10}GeP_2S_{12}$ [27], $Li_{9.54}Si_{1.74}P_{1.44}S_{11.7}Cl_{0.3}$ [12] and $Li_7P_3S_{11}$ [28] glass-ceramics, exhibit high ionic conductivities over 10^{-3} S cm^{-1}. In addition, they also have good ductility [29, 30] that facilitates intimate contact with electrode materials. Therefore, sulfide electrolytes with high ionic conductivity and good mechanical properties would be more suitable solid electrolytes for their application to the all-solid-state battery.

Sulfide solid electrolytes in the Li_2S-P_2S_5 system have been extensively studied for the application to the all-solid-state battery during the last years. The synthesis of Li_2S-P_2S_5 solid electrolytes often involves the preparation of mother glasses by a mechanical milling process and subsequent heat treatment to promote the crystallization of high ionic conductive phases. Mizuno et al. [28, 31] found that the crystalline phases are controlled by the Li_2S content in the Li_2S-P_2S_5 sulfide electrolytes. While crystallization of phases such as the $Li_7P_3S_{11}$ phase producing an enhancement of the conductivity up to 10^{-3} S cm^{-1} at room temperature is desirable, crystallization of phases such as the $Li_4P_2S_6$ phase is usually avoided because it produces a negative effect on the ionic conductivity; a decrease down to two orders of magnitude has been reported (1.1×10^{-6} S cm^{-1} at room temperature) [32].

Sulfide solid electrolytes in the Li_2S-P_2S_5 system are composed of Li^+ cations and thiophosphate anions. Upon crystallization, the thiophosphate anions organize into the different crystalline phases. Table 1 indicates the common

crystal phases and the corresponding thiophosphate anions conforming the local structure.

As illustrated in Table 1, the thiophosphate anions can take several forms. Isolated PS_4^{3-} tetrahedra (ortho-thiophosphate units), corner-sharing PS_4 tetrahedra ($P_2S_7^{4-}$ pyro-thiophosphate units), edge-sharing PS_4 tetrahedra ($P_2S_6^{2-}$ meta-thiodiphosphate units) and PS_3 units containing a P-P bond in between ($P_2S_6^{4-}$ Hypo-thiodiphosphate units).

The Li-S bond, in the sulfide solid electrolytes, with low bond energy and being relatively covalent in character, may allow the rotation and diffusion of the $P_xS_y^{z-}$ ions under the application of stress. It has been thought to be the reason for the small-scale plasticity that sulfide solid electrolytes exhibit [30]. As mentioned above, a solid electrolyte with good deformability is essential to develop favorable electrode-electrolyte interfaces in bulk-type all-solid-state batteries [33].

Bulk-type all-solid-state batteries use composite electrodes with a powder mixture of active materials and solid electrolytes. A large interfacial contact area between the active material and electrolyte particles and efficient ion-conductive pathways are necessary to obtain a good cell performance [33, 34].

Several approaches have been taken to develop favorable solid-solid interfaces. For example, sulfide solid electrolyte coating on active materials by using Pulser Laser Deposition (PLD) has been proven to be effective in obtaining high capacity and good performance in the all-solid-state-cells, due to the formation of intimate electrode-electrolyte contacts [35]. However, a scale-up of the PLD technique for a commercial application is not practical.

Table 1. Common crystal phases in the Li_2S-P_2S_5 solid electrolytes

Li_2S content (mol%)	Crystal phase	Thiophosphate units		Ref
50	$Li_2P_2S_6$	$P_2S_6^{2-}$	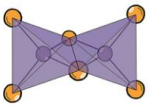	[36]
67	$Li_4P_2S_6$	$P_2S_6^{4-}$	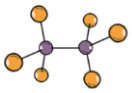	[37]
70	$Li_7P_3S_{11}$	PS_4^{3-}, $P_2S_7^{4-}$	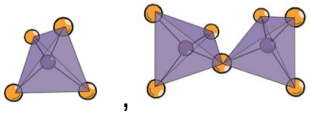	[38]
75	Li_3PS_4	PS_4^{3-}	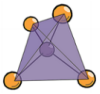	[39]

The use of small-sized solid electrolyte particles has also been reported to be effective to obtain dense and homogeneous electrode layers with an effective lithium-ion conduction pathway and large electrode-electrolyte interfacial contact areas [40]. Sulfide solid electrolytes that are typically prepared by the mechanical milling process are subsequently pulverized by using smaller diameter balls [40]. However, synthesis and pulverization, carried out by the ball milling process, require high energy and a long time.

During the last years, the preparation of sulfide solid electrolytes by a liquid-phase process, using organic solvents to promote the reactions, has been investigated as an alternative to the mechanical milling route. The liquid-phase synthesis has many advantages in relation to the main challenges in the all-solid-state battery. It offers the possibility to form intimate contacts and high surface coverage by the direct precipitation of solid electrolytes on the electrode materials, as well as the preparation of thin membranes [41]. Furthermore, it has been found that the morphology of the sulfide solid electrolytes can be controlled by the solvent selection [41-45]. Figure 1 shows the morphology of Li_3PS_4 solid electrolytes prepared by liquid-phase using different solvents. Sulfide solid electrolytes with particle size in the nanometer range can be obtained by liquid-phase (Figure 1c). In contrast, sulfide solid electrolytes with a particle size around 10 μm are obtained by the mechanical milling process (Figure 1d). The liquid-phase process not only offers the possibility to synthesize high ionic conductive sulfide solid electrolytes with control of their morphology, but it is also more favorable for the industrial scaling-up.

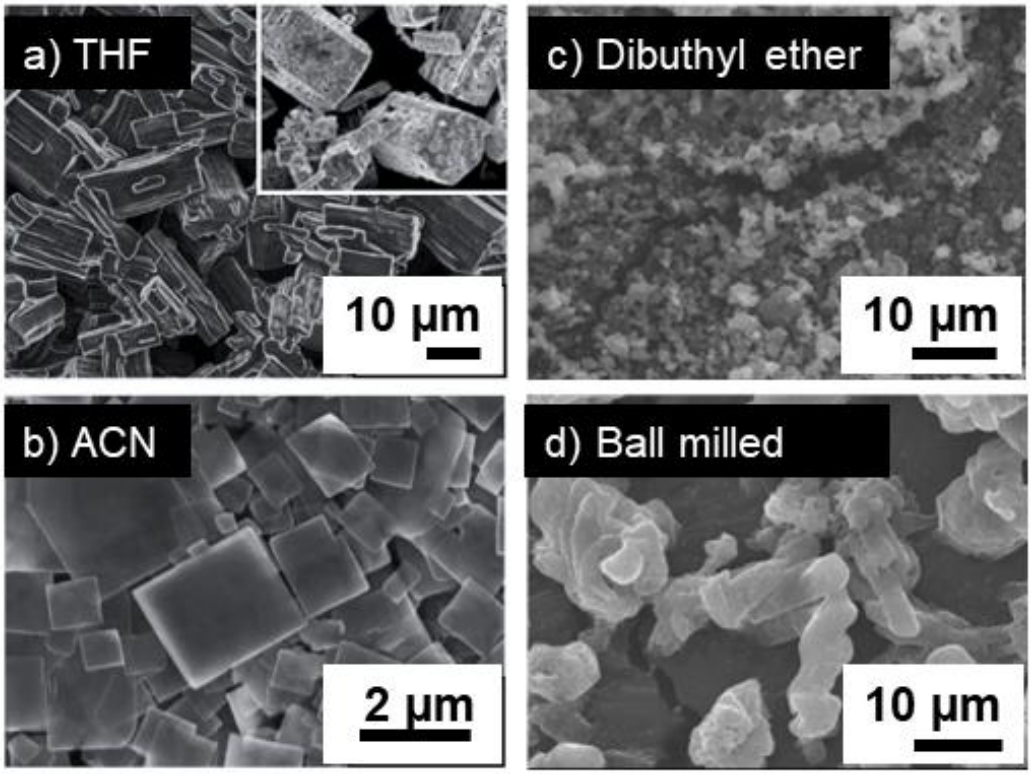

Figure 1. Morphology of Li_3PS_4 synthesized by liquid-phase using **a)** Tetrahydrofuran [42], **b)** Acetonitrile [41] and **c)** Dibuthyl ether [45] as solvents. **d)** Morphology of Li_3PS_4 synthesized by mechanical milling.

Although the liquid-phase synthesis of sulfide solid electrolytes has attracted great attention during the last years, the reaction mechanisms that take place during the synthesis have not yet been elucidated. On the other hand, the testing of the sulfide solid electrolytes prepared by liquid-phase in the all-solid-state battery is almost an unexplored area.

The present study is focused on the liquid-phase synthesis of sulfide solid electrolytes in the Li_2S-P_2S_5 system and their application to the all-solid-state battery, with the following main objectives:

1. For the application to the all-solid-state battery, the development of a solid electrolyte with high ionic conductivity and small particle size is the main challenge. For the industrial scaling up, a simple and efficient protocol is required. Thus, this work addresses the development of sulfide-based solid electrolytes in the Li_2S-P_2S_5 system, with high ionic conductivity and small particle size, using a simple liquid-phase process.

2. The liquid-phase synthesis provides additional parameters that may open a new door for the designing of the reaction pathways. However, a deep understanding of the reaction mechanisms is necessary. In this work, the formation mechanism of the fundamental $P_xS_y^{z-}$ anions by the liquid-phase synthesis is proposed.

3. The application to the all-solid-state battery is necessary to examine the suitability of the solid electrolytes prepared by liquid-phase. In this work, the electrochemical performance of all-solid-state batteries using a solid electrolyte synthesized by liquid-phase was evaluated.

This doctoral thesis consists of two main parts:

Part I – Liquid-phase synthesis of sulfide solid electrolyte in the Li_2S-P_2S_5 system

This section reports the preparation of sulfide solid electrolytes with high ionic conductivity and small particle size by liquid-phase synthesis. The crystallization process and reaction mechanisms that take place in the liquid-phase synthesis are specially discussed

First, a simple and efficient preparation of sulfide solid electrolytes is reported in the Li_2S–P_2S_5 system with Li_2S content from 70 to 75 mol%, by a liquid-phase process under ultrasonic irradiation, using acetonitrile as the medium for the reaction.

Second, the crystallization process that took place in the liquid-phase synthesis was investigated by examining the crystal and local structure, morphology and ionic conductivity of the solid electrolyte with Li_2S content of 74 mol%, after each step of the synthesis.

Third, the effect of the mass concentration and the effect of the time for the ultrasonic irradiation were optimized to avoid impurities from unreacted precursors in the solid electrolytes.

Fourth, the focus was placed on the Li_2S and P_2S_5 precursors and their reaction in 50:50 mol% to understand the initial chemical reactions that trigger the formation of the $P_xS_y^{z-}$ thiophosphate units. In light of the results founded, the

possible reaction pathways for the formation of the different $P_xS_y^{z-}$ thiophosphate units and the potential reaction pathway for the formation of the high ionic conductive $Li_7P_3S_{11}$ crystal phase in $Li_2S–P_2S_5$ solid electrolytes synthesized by liquid-phase were hypothesized.

PART II – Application of $Li_7P_3S_{11}$ solid electrolyte as an ionic conductive additive in the composite cathode of all-solid-state batteries

In this section, the electrochemical performance of an all-solid-state battery using NCM ($LiNbO_3$-coated $LiNi_{1/3}Co_{1/3}Mn_{1/3}O_2$) as a high voltage cathode material and the solid electrolyte containing the $Li_7P_3S_{11}$ crystal phase, prepared by liquid-phase under ultrasonic irradiation, as the ionic conductor in the composite cathode, was investigated and compared it to that of the all-solid-state battery using a solid electrolyte containing the $Li_7P_3S_{11}$ crystal phase but prepared by mechanical milling.

First, the structure and properties of the sulfide solid electrolytes prepared by liquid-phase and mechanical milling processes were evaluated.

Second, the morphology of the composite cathodes using the solid electrolyte containing the $Li_7P_3S_{11}$ crystal phase, prepared by liquid-phase and mechanical milling as the ionic conductive additive, were evaluated by SEM.

Third, the electrochemical characterization of the all-solid-state cells was evaluated by using galvanostatic measurements and impedance analysis.

Forth, the electrochemical behavior of the all-solid-state cell with the composite cathode using the solid electrolyte containing the $Li_7P_3S_{11}$ crystal phase, prepared by liquid-phase, was investigated under high charge-end voltages of 4.6 V vs. Li.

Fifth, the local structure stability of the $Li_7P_3S_{11}$ solid electrolyte was analyzed by using ex-situ Raman spectroscopy of the composite cathode of the all-solid-state cell after charge-discharge measurements with high charge-end voltages (4.6 V vs. Li).

In the general conclusions section, all the conclusions derived from this thesis are summarized.

References

[1] B. Dunn, H. Kamath, J.M. Tarascon, Electrical Energy Storage for the Grid: A Battery of Choices, Science 334(6058) (2011) 928-935.

[2] D. Larcher, J.M. Tarascon, Towards greener and more sustainable batteries for electrical energy storage, Nature Chemistry 7(1) (2015) 19-29.

[3] S. Chu, A. Majumdar, Opportunities and challenges for a sustainable energy future, Nature 488(7411) (2012) 294.

[4] J.-M. Tarascon, M. Armand, Issues and challenges facing rechargeable lithium batteries, Materials for Sustainable Energy: A Collection of Peer-Reviewed Research and Review Articles from Nature Publishing Group, World Scientific (2011), pp. 171-179.

[5] M. Armand, J.-M. Tarascon, Building better batteries, Nature 451(7179) (2008) 652.

[6] J.B. Goodenough, Y. Kim, Challenges for rechargeable Li batteries, Chem. Mater. 22(3) (2009) 587-603.

[7] K. Takada, Progress and prospective of solid-state lithium batteries, Acta Mater. 61(3) (2013) 759-770.

[8] A. Hayashi, A. Sakuda, M. Tatsumisago, Development of sulfide solid electrolytes and interface formation processes for bulk-type all-solid-state Li and Na batteries, Frontiers in Energy Research 4 (2016) 25.

[9] X. Han, Y. Gong, K.K. Fu, X. He, G.T. Hitz, J. Dai, A. Pearse, B. Liu, H. Wang, G. Rubloff, Negating interfacial impedance in garnet-based solid-state Li metal batteries, Nat. Mater. 16(5) (2017) 572.

[10] A. Kato, M. Suyama, C. Hotehama, H. Kowada, A. Sakuda, A. Hayashi, M. Tatsumisago, High-Temperature Performance of All-Solid-State Lithium-Metal Batteries Having Li/Li_3PS_4 Interfaces Modified with Au Thin Films, J. Electrochem. Soc. 165(9) (2018) A1950-A1954.

[11] M. Nagao, A. Hayashi, M. Tatsumisago, Fabrication of favorable interface between sulfide solid electrolyte and Li metal electrode for bulk-type solid-state Li/S battery, Electrochem. Commun. 22 (2012) 177-180.

[12] Y. Kato, S. Hori, T. Saito, K. Suzuki, M. Hirayama, A. Mitsui, M. Yonemura, H. Iba, R. Kanno, High-power all-solid-state batteries using sulfide superionic conductors, Nat. Energy 1 (2016) 7.

[13] J.C. Li, C. Ma, M.F. Chi, C.D. Liang, N.J. Dudney, Solid Electrolyte: the Key for High-Voltage Lithium Batteries, Adv. Energy Mater 5(4) (2015) 1-6.

[14] H. Nagata, Y. Chikusa, A lithium sulfur battery with high power density, J. Power Sources 264 (2014) 206-210.

[15] N. Tanibata, H. Tsukasaki, M. Deguchi, S. Mori, A. Hayashi, M. Tatsumisago, A novel discharge–charge mechanism of a S–P_2S_5 composite electrode without electrolytes in all-solid-state Li/S batteries, J. Mater. Chem. A 5(22) (2017) 11224-11228.

[16] N. Takami, K. Yoshima, Y. Harada, 12 V-Class Bipolar Lithium-Ion Batteries Using $Li_4Ti_5O_{12}$ Anode for Low-Voltage System Applications, J. Electrochem. Soc. 164(1) (2017) A6254-A6259.

[17] M. Itoh, Y. Inaguma, W.H. Jung, L.Q. Chen, T. Nakamura, High lithium ion conductivity in the perovskite-type compounds $Ln_{1/2}Li_{1/2}TiO_3$(Ln=La,Pr,Nd,Sm), Solid State Ionics 70 (1994) 203-207.

[18] C.R. Mariappan, C. Yada, F. Rosciano, B. Roling, Correlation between micro-structural properties and ionic conductivity of $Li_{1.5}Al_{0.5}Ge_{1.5}(PO_4)_3$ ceramics, J. Power Sources 196(15) (2011) 6456-6464.

[19] M. Gellert, K.I. Gries, C. Yada, F. Rosciano, K. Volz, B. Roling, Grain Boundaries in a Lithium Aluminum Titanium Phosphate-Type Fast Lithium Ion Conducting Glass Ceramic: Microstructure and Nonlinear Ion Transport Properties, J. Phys. Chem. C 116(43) (2012) 22675-22678.

[20] J.S. Thokchom, N. Gupta, B. Kumar, Superionic Conductivity in a Lithium Aluminum Germanium Phosphate Glass-Ceramic, J. Electrochem. Soc. 155(12) (2008) A915-A920.

[21] P. Hartmann, T. Leichtweiss, M.R. Busche, M. Schneider, M. Reich, J. Sann, P. Adelhelm, J. Janek, Degradation of NASICON-Type Materials in Contact with Lithium Metal: Formation of Mixed Conducting Interphases (MCI) on Solid Electrolytes, J. Phys. Chem. C 117(41) (2013) 21064-21074.

[22] V. Thangadurai, H. Kaack, W.J.F. Weppner, Novel fast lithium ion conduction in garnet-type $Li_5La_3M_2O_{12}$ (M = Nb, Ta), J. Am. Ceram. Soc. 86(3) (2003) 437-440.

[23] V. Thangadurai, W. Weppner, $Li_6ALa_2Ta_2O_{12}$ (A=Sr, Ba): Novel garnet-like oxides for fast lithium ion conduction, Adv. Funct. Mater. 15(1) (2005) 107-112.

[24] R. Murugan, V. Thangadurai, W. Weppner, Fast lithium ion conduction in garnet-type $Li_7La_3Zr_2O_{12}$, Angew. Chem. Int. Ed. 46(41) (2007) 7778-7781.

[25] H. Buschmann, J. Dolle, S. Berendts, A. Kuhn, P. Bottke, M. Wilkening, P. Heitjans, A. Senyshyn, H. Ehrenberg, A. Lotnyk, V. Duppel, L. Kienle, J. Janek, Structure and dynamics of the fast lithium ion conductor "$Li_7La_3Zr_2O_{12}$", Phys. Chem. Chem. Phys 13(43) (2011) 19378-19392.

[26] N.C. Rosero-Navarro, T. Yamashita, A. Miura, M. Higuchi, K. Tadanaga, Effect of Sintering Additives on Relative Density and Li-ion Conductivity of Nb-Doped $Li_7La_3ZrO_{12}$ Solid Electrolyte, J. Am. Ceram. Soc. 100(1) (2017) 276-285.

[27] N. Kamaya, K. Homma, Y. Yamakawa, M. Hirayama, R. Kanno, M. Yonemura, T. Kamiyama, Y. Kato, S. Hama, K. Kawamoto, A. Mitsui, A lithium superionic conductor, Nat. Mater. 10(9) (2011) 682-686.

[28] F. Mizuno, A. Hayashi, K. Tadanaga, M. Tatsumisago, High lithium ion conducting glass-ceramics in the system Li_2S-P_2S_5, Solid State Ionics 177(26-32) (2006) 2721-2725.

[29] A. Kato, M. Nose, M. Yamamoto, A. Sakuda, A. Hayashi, M. Tatsumisago, Mechanical properties of sulfide glasses in all-solid-state batteries, J. Ceram. Soc. Jpn. 126(9) (2018) 719-727.

[30] A. Sakuda, A. Hayashi, M. Tatsumisago, Sulfide Solid Electrolyte with Favorable Mechanical Property for All-Solid-State Lithium Battery, Sci Rep 3 (2013) 1-5.

[31] F. Mizuno, A. Hayashi, K. Tadanaga, M. Tatsumisago, New, highly ion-conductive crystals precipitated from Li_2S-P_2S_5 glasses, Adv. Mater. 17(7) (2005) 918-+.

[32] A. Hayashi, K. Minami, M. Tatsumisago, Development of sulfide glass-ceramic electrolytes for all-solid-state lithium rechargeable batteries, J. Solid State Electrochem. 14(10) (2010) 1761-1767.

[33] A. Sakuda, A. Hayashi, M. Tatsumisago, Recent progress on interface formation in all-solid-state batteries, Curr. Opin. Electrochem. 6(1) (2017) 108-114.

[34] A. Hayashi, A. Sakuda, M. Tatsumisago, Development of Sulfide Solid Electrolytes and Interface Formation Processes for Bulk-Type All-Solid-State Li and Na Batteries, Front. Energy Res. 4 (2016) 13.

[35] Y. Ito, M. Otoyama, A. Hayashi, T. Ohtomo, M. Tatsumisago, Electrochemical and structural evaluation for bulk-type all-solid-state batteries using Li_4GeS_4-Li_3PS_4 electrolyte coating on $LiCoO_2$ particles, Journal of Power Sources 360 (2017) 328-335.

[36] C. Dietrich, D.A. Weber, S. Culver, A. Senyshyn, S.J. Sedlmaier, S. Indris, J.r. Janek, W.G. Zeier, Synthesis, structural characterization, and lithium ion conductivity of the lithium thiophosphate $Li_2P_2S_6$, Inorg. Chem. 56(11) (2017) 6681-6687.

[37] R. Mercier, J. Malugani, B. Fahys, J. Douglande, G. Robert, Synthese, structure cristalline et analyse vibrationnelle de l'hexathiohypodiphosphate de lithium $Li_4P_2S_6$, J. Solid State Chem. 43(2) (1982) 151-162.

[38] H. Yamane, M. Shibata, Y. Shimane, T. Junke, Y. Seino, S. Adams, K. Minami, A. Hayashi, M. Tatsumisago, Crystal structure of a superionic conductor, $Li_7P_3S_{11}$, Solid State Ionics 178(15-18) (2007) 1163-1167.

[39] R. Mercier, J.-P. Malugani, B. Fahys, G. Robert, J. Douglade, Structure du tetrathiophosphate de lithium, Acta Crystallographica Section B: Structural Crystallography and Crystal Chemistry 38(7) (1982) 1887-1890.

[40] A. Sakuda, T. Takeuchi, H. Kobayashi, Electrode morphology in all-solid-state lithium secondary batteries consisting of $LiNi_{1/3}Co_{1/3}Mn_{1/3}O_2$ and Li_2S-P_2S_5 solid electrolytes, Solid State Ionics 285 (2016) 112-117.

[41] Z.D. Hood, H. Wang, A.S. Pandian, R. Peng, K.D. Gilroy, M. Chi, C. Liang, Y. Xia, Fabrication of Sub-Micrometer-Thick Solid Electrolyte Membranes of β-

Li_3PS_4 via Tiled Assembly of Nanoscale, Plate-Like Building Blocks, Adv. Energy Mater 8(21) (2018) 1800014.

[42] Z.C. Liu, W.J. Fu, E.A. Payzant, X. Yu, Z.L. Wu, N.J. Dudney, J. Kiggans, K.L. Hong, A.J. Rondinone, C.D. Liang, Anomalous High Ionic Conductivity of Nanoporous β-Li_3PS_4, J. Am. Chem. Soc. 135(3) (2013) 975-978.

[43] N.H.H. Phuc, K. Morikawa, T. Mitsuhiro, H. Muto, A. Matsuda, Synthesis of plate-like Li_3PS_4 solid electrolyte via liquid-phase shaking for all-solid-state lithium batteries, Ionics (2017) 1-7.

[44] H. Wang, Z.D. Hood, Y.N. Xia, C.D. Liang, Fabrication of ultrathin solid electrolyte membranes of β-Li_3PS_4 nanoflakes by evaporation-induced self-assembly for all-solid-state batteries, J. Mater. Chem. A 4(21) (2016) 8091-8096.

[45] S. Choi, S. Lee, J. Park, W.T. Nichols, D. Shin, Facile synthesis of Li_2S-P_2S_5 glass-ceramics electrolyte with micron range particles for all-solid-state batteries via a low-temperature solution technique (LTST), Appl. Surf. Sci. 444 (2018) 10-14.

PART I

Liquid-phase synthesis of sulfide solid

electrolytes in the Li_2S-P_2S_5 system

Around 1981, Mercier et al. reported the preparation of Li_2S-P_2S_5 glasses by melt-quenching [1], and the synthesis of crystalline ionic conductors Li_3PS_4 and $Li_4P_2S_6$ by using solid-state reaction [2, 3]. Melt-quenching and solid-state reaction remained as the main explored syntheses for two decades. In 2001, Hayashi et al. reported the preparation of Li_2S-P_2S_5 glasses by mechanical milling [4]. In the mechanical-milling, the movement of the jar transfers kinetic energy to the balls, which collide with the solid particles inside, resulting in a mechanochemical reaction. The required time to complete the reaction is dependent on several parameters, such as the material type of the balls, jar, and reagents, as well as their respective volumetric ratios [5]. Often, glassy materials are obtained by mechanical-milling. Subsequent heat treatment to the glass materials can enhance the ionic conductivity by the precipitation of high ion conductive crystals [6]. The solid-state reaction and the mechanical-milling technique have been useful for the discovery and design of novel materials [7-9]. However, the sealing requirements for the solid-state synthesis or the jar size and the long-time required (8-50 hours) for the mechanical-milling technique, limit the industrial scaling-up. Recently, the development of solution-based approaches for the synthesis of thiophosphate electrolytes has been addressed. In 2013, Liang et al. [10] reported, for the first time, the liquid-phase synthesis of a sulfide solid electrolyte. Li_2S and P_2S_5 were used as the precursors, and tetrahydrofuran as the medium for the reaction. The magnetic stirring of the starting materials, following by heat treatment at the temperature of 140°C, produced β-Li_3PS_4 with high ionic conductivity of $1.6x10^{-4}$ Scm^{-1} at

room temperature. In the solid-state reaction, the γ-Li_3PS_4 phase is usually obtained. The γ-Li_3PS_4 phase is converted to the β-Li_3PS_4 phase at temperatures around 300 °C. However, it reverts to the γ-phase at temperatures below 195 °C [11, 12]. Surprisingly, the synthesis by liquid-phase stabilized the β-Li_3PS_4 phase at room temperature, revealing the potential of the liquid-phase synthesis to provide access to metastable phases.

In classic solid-state syntheses, the main parameters to control the reaction are temperature and time, and it often results in producing the most thermodynamically stable products. In comparison, solvent-assisted syntheses offer many more reaction parameters, such as solvent properties (polarity, dielectric constant, structure, etc.), precursors concentrations, possible complexes formation, as well temperature and time. The additional parameters provided by the liquid-phase synthesis gives the possibility for the designing of the reaction pathway to obtain the desired products. Hence the liquid-phase synthesis is an exciting field of research not only from the industrial point of view but also for the discovering of new materials with superior properties.

Table 1.1 lists the liquid-phase synthesis of Li-ion conductive sulfide solid electrolytes in the Li_2S-P_2S_5 system reported so far. Most of the liquid-phase synthesis of sulfide solid electrolytes involves the reaction between Li_2S and P_2S_5 as starting materials. Solid electrolytes containing the β-Li_3PS_4 crystal phase have been the most studied until now. The structure of the β-Li_3PS_4 crystal phase is composed only of Li^+ ions and PS_4^{3-} units. The PS_4^{3-} units have been found to be successfully produced with the mediation of solvents such as tetrahydrofuran (THF), ethyl acetate (EA), acetonitrile (ACN), dimethyl

Table 1.1 Liquid-phase synthesis of sulfide-based solid electrolytes

Product	Precursors	Solvent	Reaction time	Temperature (°C)	σ (mS cm^{-1})	Refs
β-Li_3PS_4	Li_2S, P_2S_5	THF	~24 h	140	0.16	[10]
β-Li_3PS_4	Li_2S, P_2S_5	EA	24 h	160	0.33	[13]
β-Li_3PS_4	Li_2S, P_2S_5	ACN	48 h	200	0.12	[14]
Li_3PS_4	Li_2S, P_2S_5	DMC	5 h	190	0.0064	[15]
Li_3PS_4	Li_2S, P_2S_5	NMF/n-hx	~6 h	180	0.0023	[16]
β-Li_3PS_4	Li_2S, P_2S_5	EP	6 h	170	0.2	[17]
Li_3PS_4	Li_2S, P_2S_5	MPK	24 h	160	0.0003	[18]
$Li_7P_3S_{11}$	Li_2S, P_2S_5	ACN	30 min	220	1	This study
$Li_7P_3S_{11}$	Li_2S, P_2S_5	DME	72 h	250	0.27	[19]
$Li_7P_3S_{11}$	Li_2S, P_2S_5	THF	24 h	250	0.23	[20]
$Li_7P_3S_{11}$	Li_2S, P_2S_5	THF/ACN	24 h	250	0.4	[20]
$Li_7P_3S_{11}$	Li_2S, P_2S_5	ACN	24 h	250	0.97	[20]
$Li_7P_3S_{11}$	Li_2S, P_2S_5	ACN	24 h	260	1.5	[21]

carbonate (DMC), N-methyl formamide/n-hexane (NMF/n-hexane), ethyl propionate (EP) and methyl propyl ketone (MPK). PS_4^{3-} units are not only the main building units of the β-Li_3PS_4 crystal phase, but also for many other phases such as argyrodites (containing Li^+, PS_4^{3-} and X^- ions, X: Cl, Br, I), Li_4PS_4I/$Li_7P_2S_8I$ crystal phases (containing Li^+, PS_4^{3-} and I^- ions) and $Li_7P_3S_{11}$ crystal phase(containing Li^+, PS_4^{3-} and $P_2S_7^{4-}$ ions).

The $Li_7P_3S_{11}$ crystal phase is particularly interesting because it exhibits very high ionic conductivity over 10^{-2} Scm^{-1} [7]. Solid electrolytes containing the $Li_7P_3S_{11}$ crystal phase have been synthesized using ACN, ACN-THF mixture, THF and DME as solvents. In all reported cases, magnetic stirring from one to three days was necessary (Table 1.1). After the evaporation of the solvent, subsequent heat treatment was required for the crystallization of the $Li_7P_3S_{11}$ phase. Although similar processes were used, the solid electrolytes exhibited differences in the ionic conductivity, according to the solvent used. The ionic conductivities were reported to be 9.7 x 10^{-4} Scm^{-1} [20], 4 x 10^{-4} Scm^{-1} [20], 2.3 x 10^{-4} Scm^{-1} [20] and 2.7 x 10^{-4} Scm^{-1} [19], when ACN, ACN-THF mixture, THF and DME were used as the solvent, respectively. Ideally, the solvent is only the medium for the reaction. However, it has been found that the solvent also plays a fundamental part in the reaction mechanism that takes place during the liquid-phase synthesis. Complex formation with solvent molecules and formation of intermediates may largely influence the final properties of the solid electrolytes. Particularly, acetonitrile has enabled to obtain sulfide solid electrolytes with higher ionic conductivity [20].

The liquid-phase synthesis of sulfide solid electrolytes is promising to stabilize metastable materials that often exhibit superior properties. However, the

reaction mechanism that takes place during the liquid-phase synthesis has not yet been elucidated. Clarification of the reaction mechanisms is necessary to push forward this exciting field of research.

In this work, the objective is to elucidate the reaction mechanisms that take place in the liquid-phase synthesis of sulfide solid electrolytes in the Li_2S-P_2S_5 system when acetonitrile is used as the solvent. Although acetonitrile is chosen as the referent solvent, the elucidation of the reaction mechanism can provide a better understanding of the reaction mechanisms that take place for different solvents.

Preparation of Li_2S-P_2S_5 solid electrolytes

In the vast majority of reported synthesis, Li_2S and P_2S_5 are used as the precursors for the preparation of Li_2S-P_2S_5 sulfide solid electrolytes. The liquid-phase synthesis of sulfide solid electrolytes usually involves the mixing of the precursors in a certain solvent, following by magnetic stirring for one to three days [20, 21], and subsequent drying and heat treatment to obtain the desirable crystal phases.

Ultrasonic irradiation is a useful technique to increase chemical reactivity in a solid-liquid system [22, 23]. The implosion of cavitation bubbles during ultrasonication generates local high temperatures and pressures, and this large amount of energy stimulates chemical activity. Thus, in this work, ultrasonic irradiation was used to accelerate the reaction.

Scheme 1.1 shows the synthesis procedure. Li_2S (Mitsuwa Chemical, 99.9%) and P_2S_5 (Aldrich, 99%), in stoichiometry compositions, were mixed in anhydrous acetonitrile (Wako Pure Chemical Industries). Each mixture was ultrasonicated under 28 kHz using an ultrasonic bath (Shimadzu SUS-103) for a certain time. The ultrasonication process formed a white suspension in all samples. The suspension was dried at 180 °C for three hours under

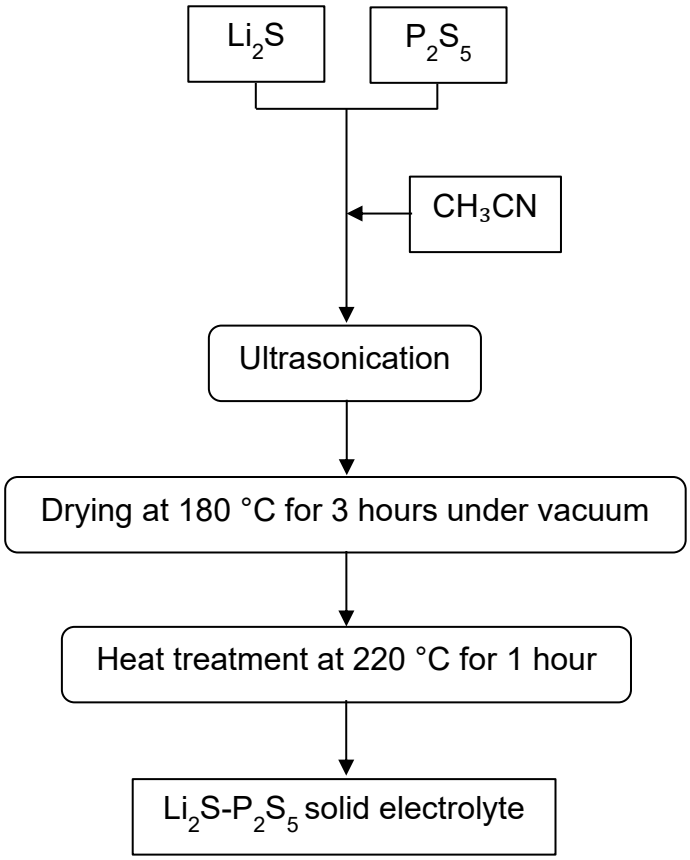

Scheme 1.1 Experimental procedure for the liquid-phase synthesis of sulfide solid electrolytes in the Li_2S-P_2S_5 system.

vacuum to remove the solvent and obtain solid powders. The solid electrolytes powders were manually ground, using an agate mortar. Subsequently, the powders were heat-treated at the temperature of 220 °C.

Characterization

The crystal phase and local structure of the solid electrolytes were studied by using X-ray diffraction (XRD) and Raman spectroscopy. XRD measurements were performed using CuKα radiation with an X-ray diffractometer (Miniflex 600, Rigaku). Diffraction data were collected at 0.01° steps from 10° to 40° in 2θ.

Raman spectroscopy was performed using a Raman spectrometer (HORIBA XploRA PLUS Scientific). Raman spectra were recorded between 300 and 3000 cm^{-1}.

The morphology of the sulfide solid electrolyte particles was observed by scanning electron microscopy (SEM) performed on a JIB-4600F Multibeam SEM-FIB Scanning Electron Microscope.

The ionic conductivity of pelletized samples was evaluated by electrochemical impedance spectroscopy (EIS). The solid electrolyte powders (80 mg) were pressed under 360 MPa (at room temperature) in a polycarbonate tube, with a 10 mm diameter; two stainless steel (SS) disks were used as current collectors. EIS was measured using an impedance analyzer (SI 1260, Solartron) to assess the ohmic resistance of the pellet.

1. Preparation of $Li_2S–P_2S_5$ solid electrolytes by a liquid-phase process

To explore the liquid-phase synthesis of sulfide solid electrolytes in the $Li_2S–P_2S_5$ systems, solid electrolytes with Li_2S content of 70, 71, 72, 73, 74 and 75 mol% were prepared by following the synthesis procedure illustrated in Scheme 1.1. Table 1.2 shows the settled parameters for the liquid-phase synthesis.

Figure 1.1 shows photographs of the material after each step of the synthesis. After adding acetonitrile to the Li_2S-P_2S_5 mixture, a white precipitate and a yellowish solution were observed (a). After 30 minutes of ultrasonic irradiation, the white precipitate and yellowish solution turned into a white suspension (b). After the ultrasonic irradiation, the solvent was immediately evaporated under vacuum at 180 °C. A slightly yellowish powder was then collected (c). After subsequent heat treatment at 220 °C, the powder turned slightly brown (d). The same characteristics were observed for all the studied compositions.

Table 1.2. Parameters used for the liquid-phase synthesis (Section 1)

Parameter	Value
Mass concentration	50 g/L
Ultrasonication time	30 min

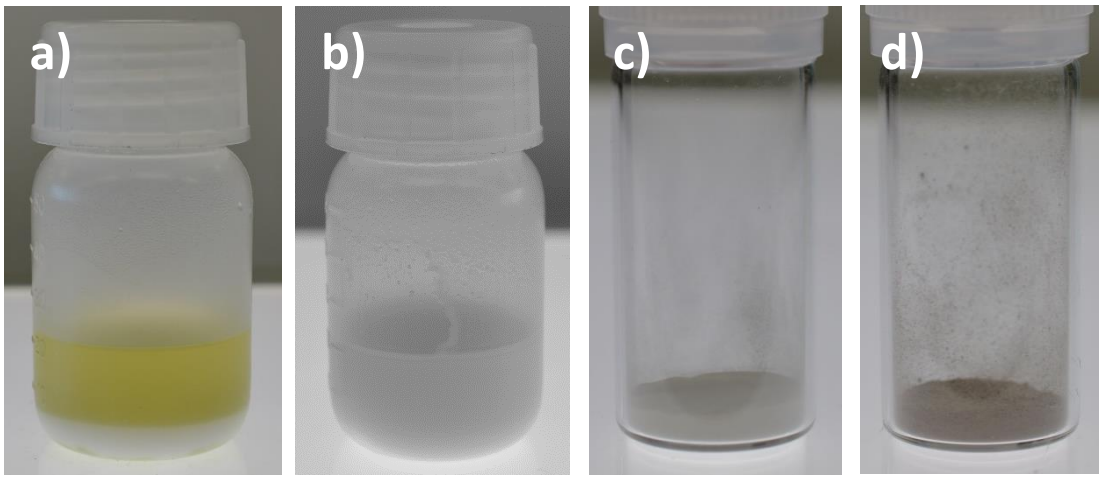

Figure 1.1 Photographs of the material state after each step of the synthesis. **a)** Before and **b)** after ultrasonic irradiation for 30 min**, c)** after removing the solvent at 180 °C under vacuum, and **d)** after heat treatment at 220 °C.

Crystal phase and local structure

After the heat treatment at 220 °C, the crystal phase and local structure of each composition were examined by using X-ray diffraction and Raman spectroscopy.

Figure 1.2 shows the X-ray diffraction pattern of the $xLi_2S{\cdot}(100\text{-}x)P_2S_5$ solid electrolytes with x Li_2S content from 70 to 75 mol%. The indexed diffraction pattern of the $Li_7P_3S_{11}$ (ICSD:157564), $Li_4P_2S_6$ (ICSD: 80319) and γ-Li_3PS_4 (ICD: 180318) crystal phases are shown for comparison.

Peaks corresponding to the $Li_7P_3S_{11}$ crystal phase were observed in the XRD patterns of all the studied compositions. Formation of $Li_4P_2S_6$ and ɤ-Li_3PS_4 phases were observed in the solid electrolytes with Li_2S content of 70 and 71 mol%. Additional peaks corresponding to an unknown crystal phase were also observed at these compositions. The peak at around 2θ=27°, observed in all compositions, could be assigned to the Li_2S precursor.

Figure 1.3 shows the Raman spectra of the $xLi_2S{\cdot}(100\text{-}x)P_2S_5$ solid electrolytes with x Li_2S content from 70 to 75 mol%. The Raman spectrum of the solid electrolyte with Li_2S content of 75 mol% shows two bands located at 428 cm^{-1} and 405 cm^{-1} assigned to PS_4^{3-} and $P_2S_7^{4-}$ units [12], respectively. The Raman spectrum of the solid electrolyte with Li_2S content of 74 mol% shows a wide band centered at 405 cm^{-1} corresponding mainly to $P_2S_7^{4-}$ units. The Raman spectrum of the solid electrolyte with Li_2S content of 73 mol%

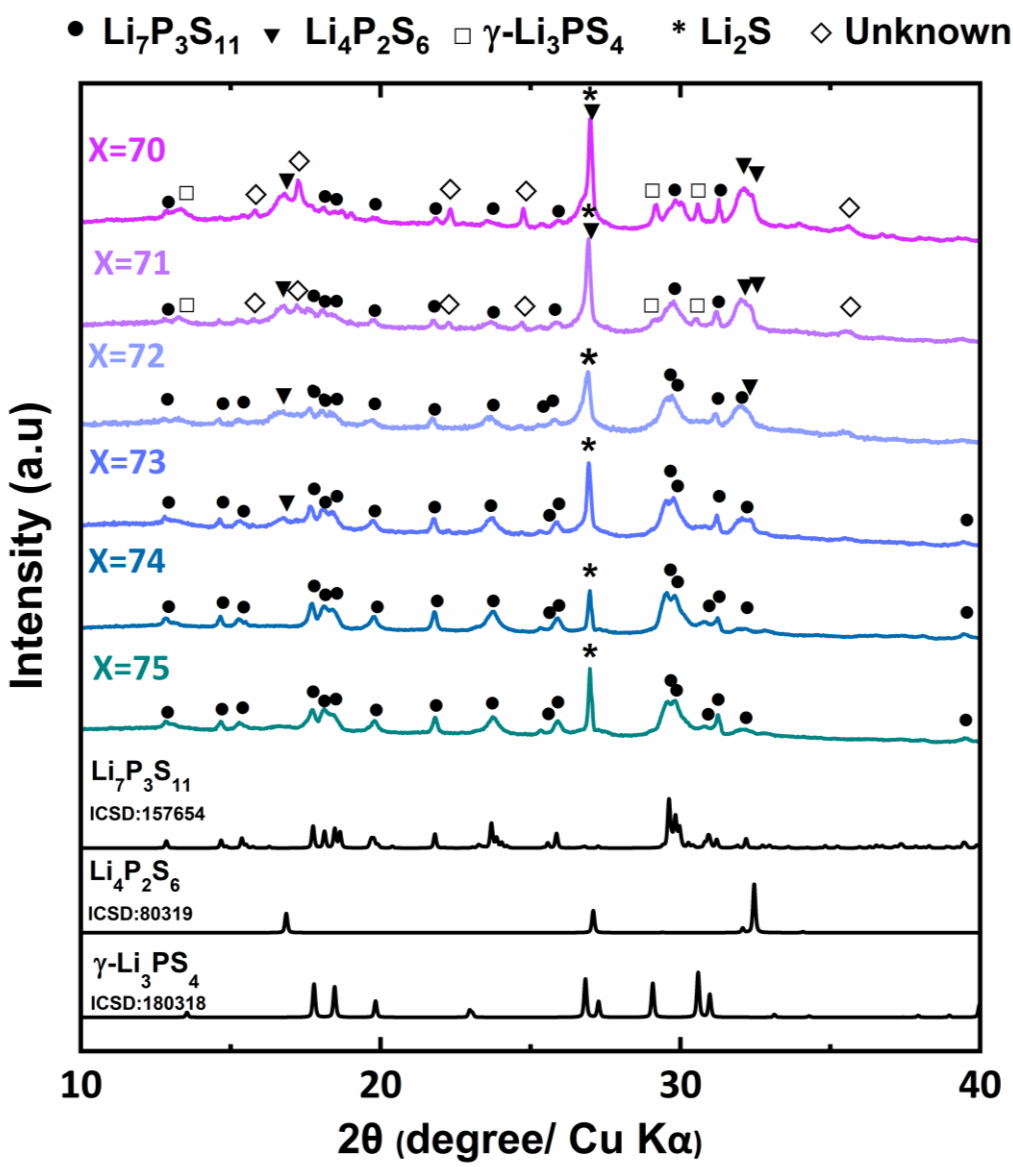

Figure 1.2 XRD patterns of $xLi_2S{\cdot}(100\text{-}x)P_2S_5$ solid electrolytes synthesized by liquid-phase. Indexed diffraction pattern of the $Li_7P_3S_{11}$ (ICSD:157564), $Li_4P_2S_6$ (ICSD: 80319) and γ-Li_3PS_4 (ICD: 180318) crystal phases are shown for comparison.

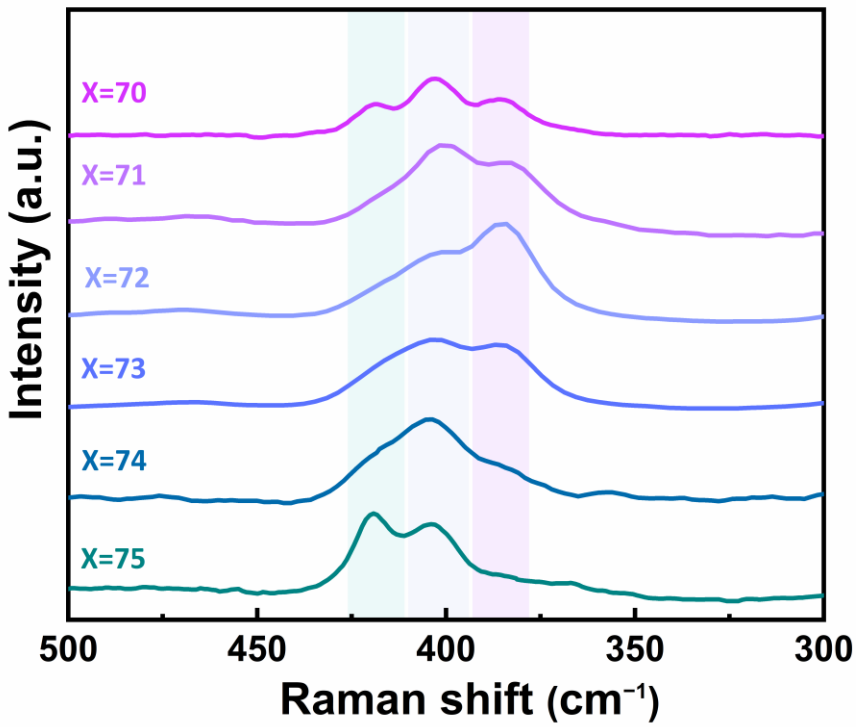

Figure 1.3 Raman spectra of $xLi_2S\cdot(100-x)P_2S_5$ solid electrolytes synthesized by liquid-phase.

shows two wide bands centered at 405 cm^{-1} and 385 cm^{-1}. The Raman band at 385 cm^{-1} has been assigned to the $P_2S_6^{4-}$ units [12]. The Raman spectrum of the solid electrolyte with Li_2S content of 72 mol% shows two wide bands centered at 405 cm^{-1} and 385 cm^{-1}, corresponding to $P_2S_7^{4-}$ and $P_2S_6^{4-}$ units. The Raman spectrum of the solid electrolyte with Li_2S content of 71 mol% shows similar bands to that with Li_2S content of 72 mol%, with a slight increase of the band at 405 cm^{-1}. The Raman spectrum of the solid electrolyte with Li_2S content of 70 mol% shows three bands located at 428 cm^{-1}, 405 cm^{-1} and 385 cm^{-1} corresponding to $P_2S_6^{4-}$ units, $P_2S_7^{4-}$ and PS_4^{3-} units.

Morphology

After the heat treatment at 220 °C, the morphology of each composition was examined by Scanning electron microscopy (SEM).

Figure 1.4 shows SEM images of the $xLi_2S{\cdot}(100\text{-}x)P_2S_5$ solid electrolytes with x Li_2S content from 70 to 75 mol%. The morphology in all compositions consisted of nano-sized particles with an irregular shape.

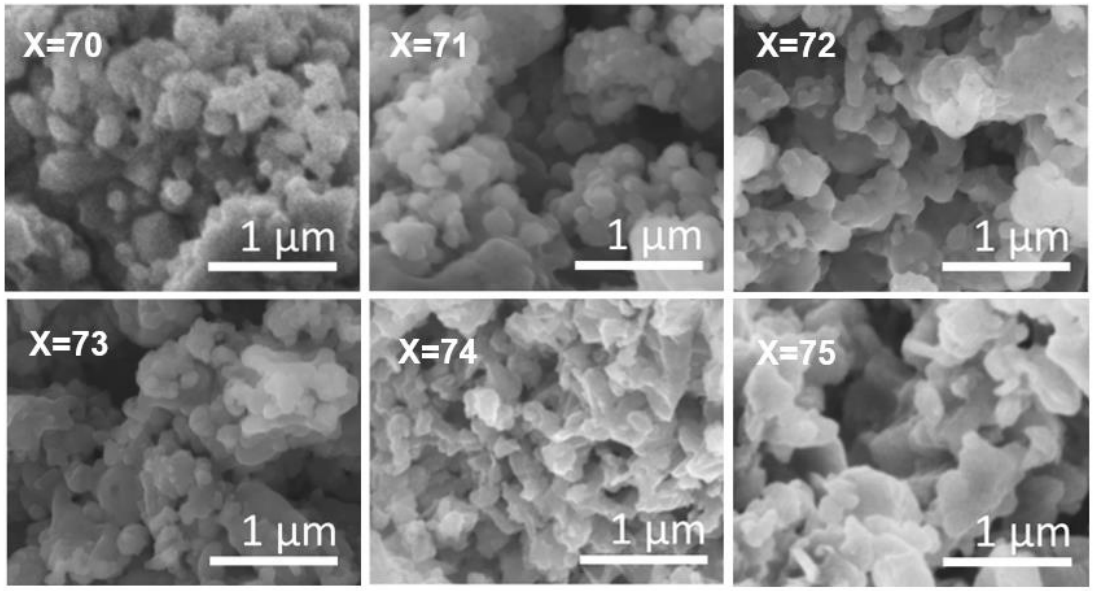

Figure 1.4 SEM images of $xLi_2S\cdot(100-x)P_2S_5$ solid electrolytes synthesized by liquid-phase.

Ionic Conductivity

After the heat treatment at 220 °C, the ionic conductivity of each composition was examined by electrochemical impedance spectroscopy (EIS). Figure 1.5 shows the ionic conductivity of the $xLi_2S{\cdot}(100\text{-}x)P_2S_5$ sulfide electrolytes.

The attained ionic conductivity of the $xLi_2S{\cdot}(100\text{-}x)P_2S_5$ sulfide electrolytes with Li_2S content of 70, 71, 72, 73, 74 and 75 mol% was 1.1 x 10^{-5} S cm^{-1}, 3.4 x 10^{-5} S cm^{-1}, 5.8 x 10^{-5} S cm^{-1}, 1.5 x 10^{-4} S cm^{-1}, 1.0 x 10^{-3} S cm^{-1} and 6.4 x 10^{-4} S cm^{-1}, respectively. The ionic conductivity increased with the Li_2S content until a maximum value of 10^{-3} S cm^{-1} with the Li_2S of 74 mol%. The difference in the ionic conductivity between the solid electrolytes in the studied compositions achieved up to two orders of magnitude.

Discussion and Summary

The study of the $xLi_2S{\cdot}(100\text{-}x)P_2S_5$ sulfide electrolytes obtained after heating at 220 °C suggests that the variation of ionic conductivity is largely influenced by the resulting crystalline phases and the local arrangement of the $P_xS_y^{z-}$ units. Although the $Li_7P_3S_{11}$ high ionic conductor was identified in all the compositions, the distribution of $P_xS_y^{z-}$ units was clearly different for each composition. Lower ionic conductivity (~10^{-5} S cm^{-1}) resulted from $xLi_2S{\cdot}(100\text{-}x)P_2S_5$ sulfide electrolytes with low content of Li_2S (x = 70-71 mol%); attributed to the presence

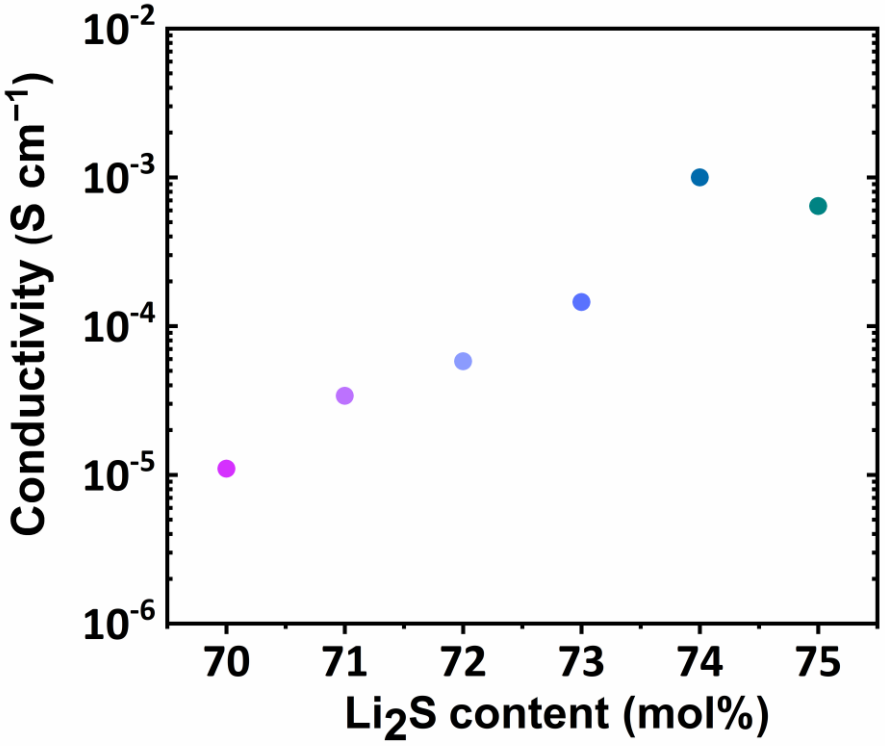

Figure 1.5 Ionic conductivity of $xLi_2S{\cdot}(100\text{-}x)P_2S_5$ solid electrolytes synthesized by liquid-phase.

of the low ionic conductive crystal phases, $Li_4P_2S_6$ and ɤ-Li_3PS_4 [11], confirmed by X-ray diffraction spectroscopy. Further, the slight increase of the Li_2S content (x = 72-73 mol%) was enough to remove the presence of the low ionic conductive phases, producing an improvement of the ionic conductivity up to one order of magnitude (~10^{-4} S cm^{-1}). The significantly higher presence of $P_2S_6^{4-}$ units in comparison with PS_4^{3-} and $P_2S_7^{4-}$ units was assumed as the main reason for the relatively low ionic conductivity. Higher content of Li_2S (x = 74-75 mol%) produced the highest ionic conductivity (~10^{-3} – 10^{-4} S cm^{-1}) in the $xLi_2S{\cdot}(100\text{-}x)P_2S_5$ solid electrolytes obtained by liquid phase process. Since the XRD patterns did not exhibit considerable changes in the $Li_7P_3S_{11}$ crystal phase, for example, between solid electrolytes with Li_2S content of 72 and 73 mol%, the high ionic conductivity can be interpreted by the optimized arrangement of the $P_xS_y^{z-}$ units. Raman spectrum of the sample with Li_2S content of 74 mol%, which exhibited the highest ionic conductivity of 10^{-3} S cm^{-1}, revealed that the presence of $P_2S_7^{4-}$ units (respect to PS_4^{3-} and $P_2S_6^{4-}$ units), is significantly higher compared to the sample with Li_2S content of 75 mol%. It can be inferred that the high content of $P_2S_7^{4-}$ units in the structure of the $xLi_2S{\cdot}(100\text{-}x)P_2S_5$ sulfide electrolytes resulted in the formation of high ionic conductive materials.

2. Crystallization process of Li_2S-P_2S_5 solid electrolytes through liquid-phase synthesis

The Li_2S-P_2S_5 solid electrolyte with Li_2S content of 74 mol% exhibited the high ionic conductivity of 10^{-3} Scm^{-1}. A solid electrolyte prepared by liquid-phase and with high ionic conductivity is a promising material for the application to the all-solid-state battery. Hence, the crystallization process that took place in the liquid-phase synthesis was investigated by examining the crystal and local structure, morphology and ionic conductivity of the solid electrolyte with Li_2S content of 74 mol%, after each step of the synthesis.

Crystal phase and local structure

Figure 1.6 shows the XRD patterns of the Li_2S-P_2S_5 solid electrolyte with Li_2S content of 74 mol% after drying at 180 °C for three hours under vacuum and after subsequent heat treatment at 220 °C for one hour. The indexed diffraction pattern of the $Li_7P_3S_{11}$ crystal phase (ICSD:157564) is shown for comparison.

After the drying process at 180°C, the XRD pattern of the sample exhibited unknown peaks. The peak at 2θ=27° could be assigned to the Li_2S precursor, but the other peaks do not correspond to the P_2S_5 precursor or any indexed solid electrolyte crystal phase. Unknown peaks were assigned as PS_4^{3-}·ACN; it will be discussed below. After subsequent heat treatment at 220 °C, XRD peaks corresponding to the $Li_7P_3S_{11}$ crystal phase were observed.

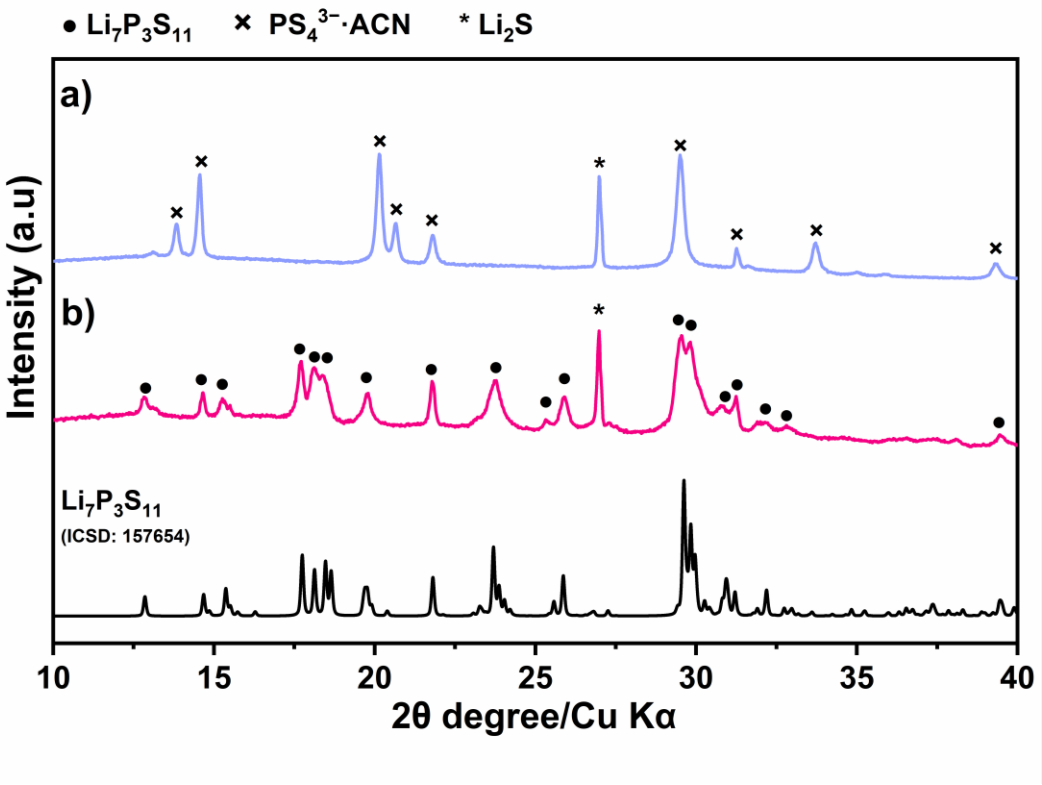

Figure 1.6 XRD patterns of the Li_2S-P_2S_5 solid electrolyte with Li_2S content of 74 mol% after drying at 180 °C for 3 h under vacuum **(a)** and after subsequent heat treatment at 220 °C for 1 h **(b)**. The indexed diffraction pattern of the $Li_7P_3S_{11}$ crystal phase (ICSD: 157564) is shown for comparison.

The local structure of the solid electrolyte after each step of the synthesis was examined by using Raman spectroscopy. Figure 1.7a shows the Raman spectra of the Li_2S-P_2S_5 solid electrolyte with Li_2S content of 74 mol%, after the ultrasonication process (corresponding to a slurry state), after drying at 180 °C for 3 h under vacuum and after subsequent heat treatment at 220 °C for 1 h.

The Raman spectrum of the sample after only 30 minutes of ultrasonication (Green line), exhibited a main band at 428 cm^{-1}, attributed to the PS_4^{3-} (*ortho*-thiophosphate) units [12]. Also, bands located around 370 cm^{-1}, 900 cm^{-1}, 2200 cm^{-1} and 2900 cm^{-1}, corresponding to C-C≡N bending, C-C stretch, C≡N stretching and symmetric C-H stretch vibrations of acetonitrile [24, 25] were identified.

The Raman spectrum of the sample after the subsequent drying at 180°C for 3 h under vacuum (Blue line), exhibited similar bands to that of the slurry obtained after the ultrasonication (Green line), revealing that the obtained powder is composed mainly by PS_4^{3-} units and remaining acetonitrile.

The Raman spectrum of the sample after subsequent heat treatment at 220 °C, exhibited only a main wide band at 405 cm^{-1}, attributed to $P_2S_7^{4-}$ (*pyro*-thiophosphate) units [12]. The bands associated with acetonitrile completely disappeared, confirming the full removal of the solvent. The heat treatment at 220 °C, to remove the remaining solvent, also promoted the formation of $P_2S_7^{4-}$ units. Figure 1.7b shows the deconvolution of the Raman band centered at 405 cm^{-1} of the sample after heat treatment at 220 °C, using a Gaussian-Lorentzian function. Two bands centered at 420 cm^{-1} and 404 cm^{-1} confirmed the

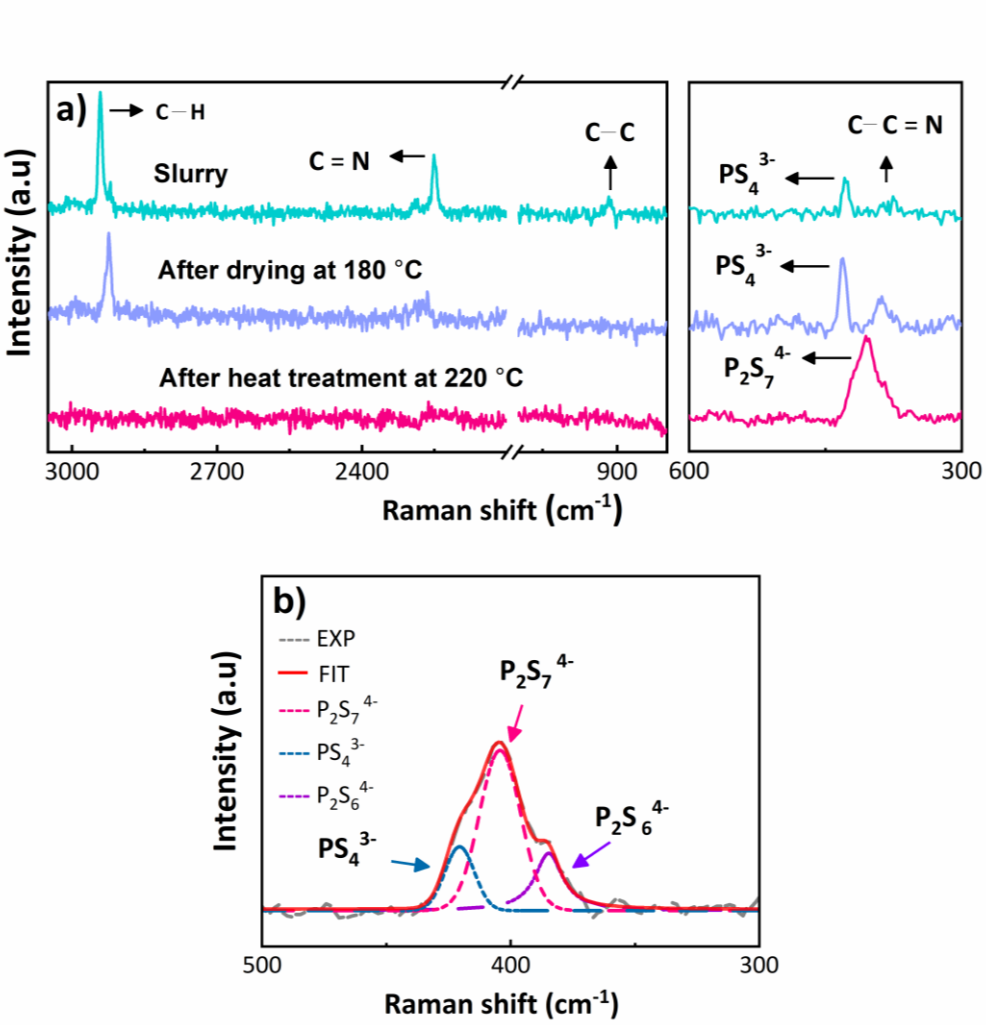

Figure 1.7 a) Raman spectra of the Li_2S-P_2S_5 solid electrolyte with Li_2S content of 74 mol% after the ultrasonication process (Slurry, green line), after drying at 180 °C for 3 h under vacuum (Blue line) and after subsequent heat treatment at 220 °C for 1 h (Pink line). **b)** Spectral decomposition of the Raman spectrum of the sample after heat treatment at 220 °C. Dashed grey line, experimental data; continuous orange line, the fitting result for all $P_xS_y^{z-}$ polyhedral; dashed blue, pink and violet lines, PS_4^{3-}, $P_2S_7^{4-}$ and $P_2S_6^{4-}$ units, correspondingly.

presence of $P_2S_7^{4-}$ and PS_4^{3-} units [12, 26], respectively. A third band centered at 385 cm^{-1} was also found and is associated with $P_2S_6^{4-}$ units. From crystal structural analysis, the $Li_7P_3S_{11}$ crystal phase consists of only PS_4^{3-} and $P_2S_7^{4-}$ units [27]. However, $P_2S_6^{4-}$ units have also been identified in solid electrolytes, containing the $Li_7P_3S_{11}$ crystal phase [28, 29], obtained by mechanical milling. Studies by using MAS-NMR (magic-angle spinning-nuclear magnetic resonance) spectroscopy, suggest that after crystallization of the $Li_7P_3S_{11}$ crystal phase, part of the $P_xS_y^{z-}$ units would remain in the amorphous phase [30]. Thus, it is assumed that the $P_2S_6^{4-}$ structural units contained in the solid electrolyte here studied would also be in the amorphous phase.

The evaluation of the crystal and local structures of the solid electrolyte after each step of the synthesis by using X-ray diffraction and Raman spectroscopy are well correlated. According to the Raman spectra, the unknow crystal phase observed after drying under vacuum at 180 °C, would correspond to the complex formation between PS_4^{3-} units and acetonitrile molecules (ACN). The complex between PS_4^{3-} units and ACN molecules was assigned as $PS_4^{3-}\cdot$ACN. The main $Li_7P_3S_{11}$ crystal phase observed after heat treatment at 220 °C, was confirmed to be composed by PS_4^{3-} and $P_2S_7^{4-}$ units, and a small content of $P_2S_6^{4-}$ units, by the Raman spectra analysis. The additional intense peak associated with the Li_2S crystal phase, observed after the drying process at 180°C and heat treatment at 220 ˚C, can be explained by the possible formation mechanism of the $Li_7P_3S_{11}$ crystal phase.

Morphology

Figure 1.8 shows the morphology of the Li_2S-P_2S_5 solid electrolyte with Li_2S content of 74 mol% after drying at 180 °C for 3 h under vacuum and after subsequent heat treatment at 220 °C for 1 h. After drying at 180°C, big agglomerates (approx. 5-20 µm) and irregular particles with a small particle size around 500 nm were observed. After subsequent heat treatment at 220 °C, the particle size was irregular but remained in the nanometric range. Inset in figure 1.8b shows smaller individual particles lower than 500 nm.

The small particle size is attributed to the interaction between solvent and particles during the synthesis process. Acetonitrile can play a surfactant function [14], leading to obtain a better dispersion of the powder during the ultrasonication and further a good control of the particle size growth during the solvent removal. In contrast, preparation of sulfide solid electrolyte by ball milling produces particle sizes greater than 10 µm [31].

Ionic conductivity

Figure 1.9a. show the impedance spectra of the Li_2S-P_2S_5 solid electrolyte with Li_2S content of 74 mol% after drying at 180 °C for 3 h under vacuum. The impedance spectra consist of a well-defined semicircle at high frequency due

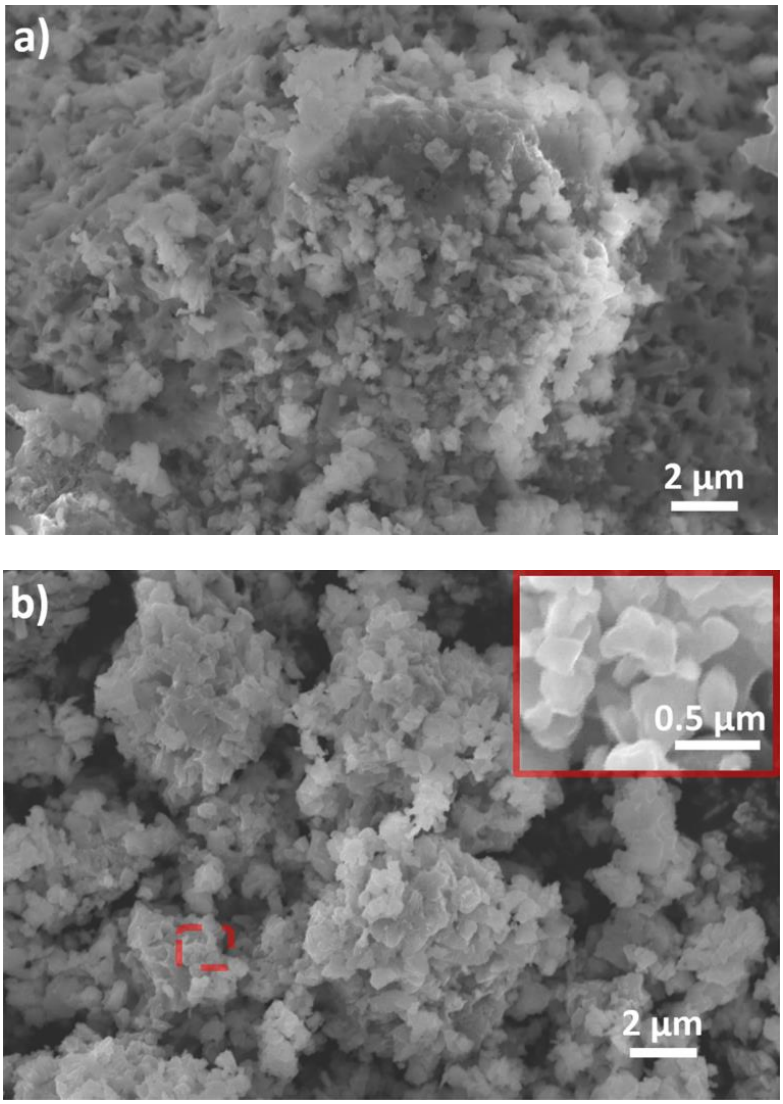

Figure 1.8 Morphology of the Li_2S-P_2S_5 solid electrolyte with Li_2S content of 74 mol% **a)** after drying at 180 °C for 3 h under vacuum and **b)** after subsequent heat treatment at 220 °C for 1 h.

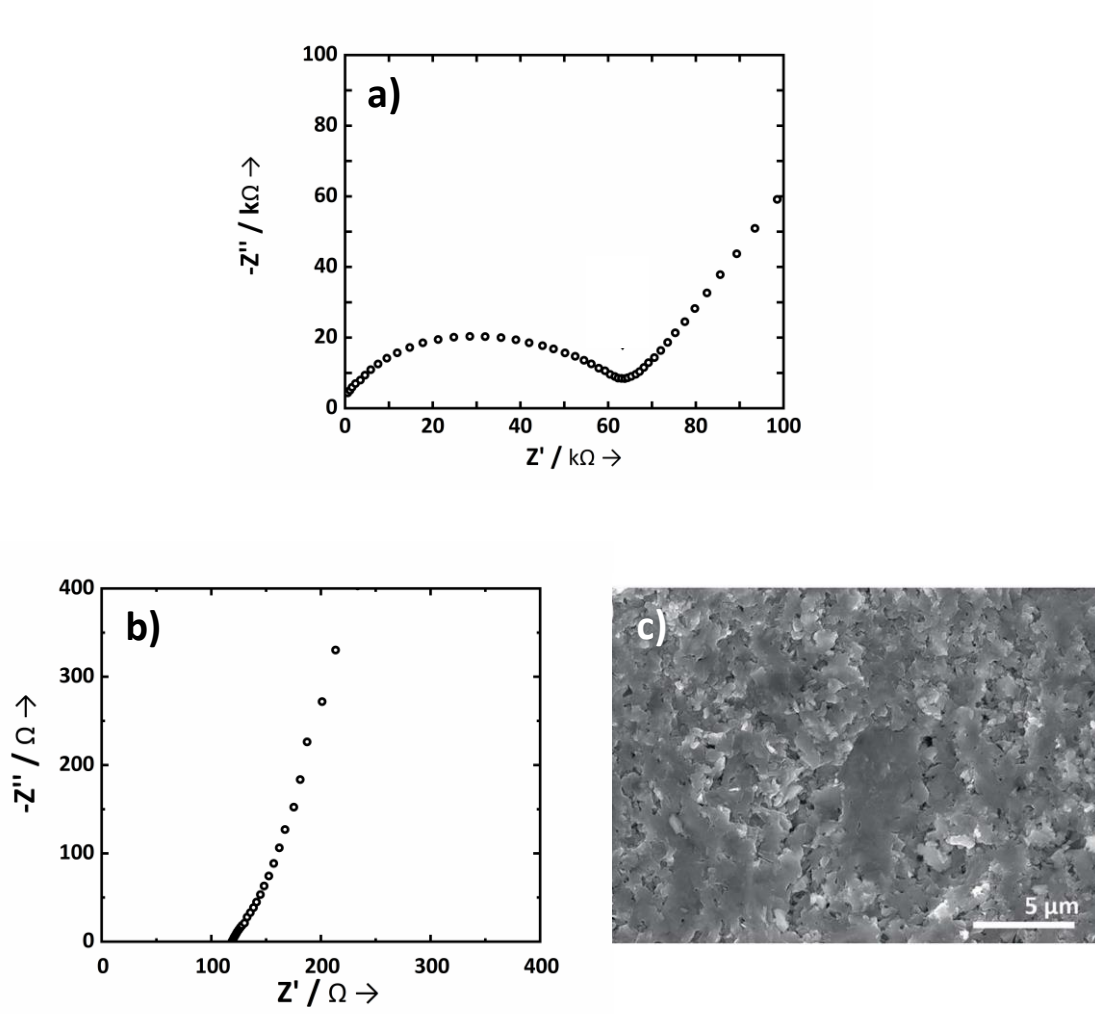

Figure 1.9 Impedance spectra of the Li_2S-P_2S_5 solid electrolyte with Li_2S content of 74 mol% **a)** after drying at 180 °C for 3 h under vacuum and **b)** after subsequent heat treatment at 220 °C for 1 h. **c)** Cross-section image of the pelletized sample in b).

to bulk and grain boundary resistances and a capacitive tail at low frequency due to the electrodes interface. The data was fitted with a simple equivalent circuit comprising a resistor in parallel with a capacitor *(R||C, C is a constant phase element)* to describe the pellet electrical behavior. In addition, a capacitor in series was used to simulate the contribution of the electrodes interface. The total resistance (bulk and grain boundary resistances), was used to calculate the ionic conductivity, attaining 1.4 x 10^{-6} S cm^{-1} (22 °C). Figure 1.9b shows the impedance spectra of the solid electrolyte obtained after the subsequent heat treatment at 220 °C for 1 h. The impedance spectra of the sample do not exhibit the full semicircle due to the lower resistance. In this case, the resistance was estimated by the value of Z' at the intercept with the real axis obtained by linear fitting. The ionic conductivity of the solid electrolyte attained 1.0 x 10^{-3} S cm^{-1} (22°C). Figure 1.9c shows the cross-section image of the solid electrolyte pellet corresponding to figure 1.9b. The cross-section image displays a compact surface with a tight contact of micronized particles. There is almost no crack, but microporous were observed.

Figure 1.10 shows the temperature dependence of the ionic conductivity of the solid electrolyte obtained after heat treatment at 220 °C. A low activation energy of 12.8 kJ mol^{-1} was calculated. In comparison, $Li_7P_3S_{11}$ solid electrolyte is reported to have an activation energy of 12 kJ mol^{-1} when the synthesis is carried out by mechanical milling [32] and 23 kJ mol^{-1} when the synthesis is carried out by liquid phase using only magnetic stirring [21].

The obtained lower activation energy, in comparison with other $Li_7P_3S_{11}$ solid electrolyte obtained by liquid phase process, is assumed to be because of the

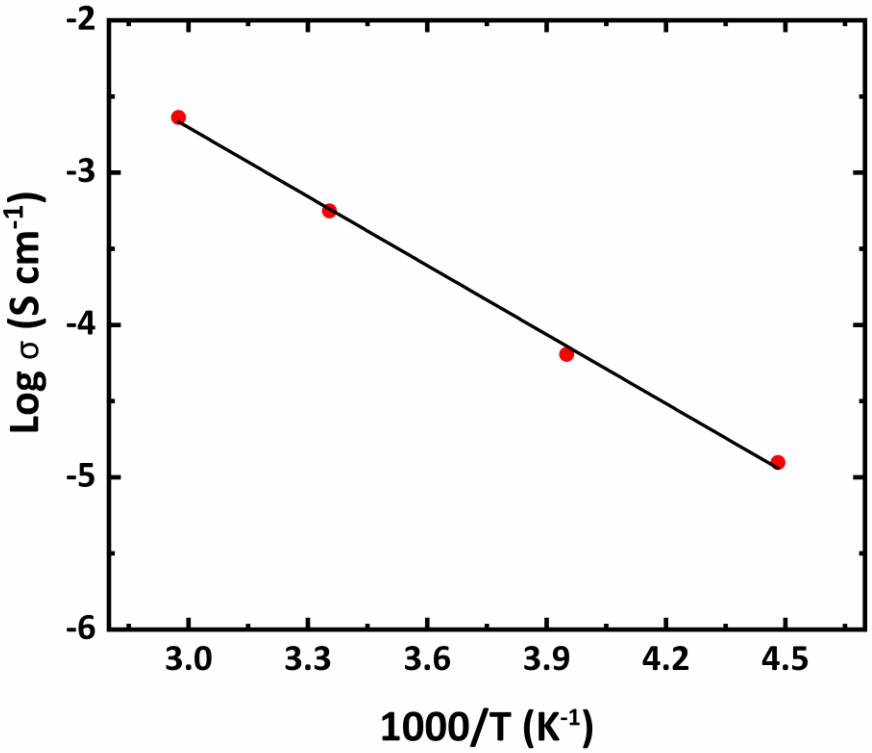

Figure 1.10 Temperature dependence of the ionic conductivity of the Li_2S-P_2S_5 solid electrolyte with Li_2S content of 74 mol% after drying at 180 °C for 3 h under vacuum and subsequent heat treatment at 220 °C for 1 h.

higher crystallization degree [32], as well as good densification because of the smaller particle size.

Discussion and Summary

The studies about crystal and local structure, morphology and impedance of the Li_2S-P_2S_5 solid electrolyte with Li_2S content of 74 mol% for each step of the synthesis are well correlated and revealed the crystallization process that takes place during the liquid phase process. The cavitation produced during the ultrasonication provides enough energy for the formation of PS_4^{3-} units after only 30 min. The X-ray spectrometry and Raman spectroscopy studies revealed the complex formation between PS_4^{3-} units and acetonitrile molecules, named here as PS_4^{3-}·ACN. The PS_4^{3-}·ACN complex was dissociated upon heating at 220 °C. The dissociation of the complex was accompanied by the formation of $P_2S_7^{4-}$ units resulting in the precipitation of the $Li_7P_3S_{11}$ crystal phase. The crystallization of the high ionic conductive $Li_7P_3S_{11}$ crystal phase was accompanied by an increase in the ionic conductivity in more of three orders of magnitude, from 1.4×10^{-6} to 1×10^{-3} Scm^{-1}.

On the other hand, the particle size of the solid electrolyte obtained by liquid-phase process is more than 10 times smaller compared with the particle size obtained by mechanical milling process (10 µm) [31]. The small particle size is attributed to the interaction between solvent and particles during the synthesis process. Acetonitrile would help to obtain a better dispersion of the powder

during the ultrasonication and further a good control of the particle size growth during the solvent removal [14].

3. The search for the stoichiometry

The preparation of high ionic conductive sulfide solid electrolytes in the Li_2S-P_2S_5 system by liquid-phase was discussed above. Particularly the Li_2S-P_2S_5 solid electrolyte with Li_2S content of 74 mol%, containing the $Li_7P_3S_{11}$ crystal phase, exhibited high ionic conductivity up to 10^{-3} Scm^{-1} and a small particle size of around 500 nm. These characteristics are advantageous for the application to the all-solid-state battery. However, from the chemistry point of view, the followed liquid-phase process (Table 1.2) resulted in a change in the stoichiometry.

Formally, the stoichiometric composition of the $Li_7P_3S_{11}$ crystal phase corresponds to a Li_2S:P_2S_5 ratio of 70:30 in mol%. In an effort to preserve the stoichiometry, the effect of the mass concentration and the effect of the ultrasonic irradiation time on the properties of the $70Li_2S$:$30P_2S_5$ solid electrolyte prepared by liquid-phase were evaluated.

Effect of the mass concentration

From the solubility point of view, the reaction between Li_2S and P_2S_5 could be favored by the use of a smaller mass concentration. Hence, the effect of the smaller mass concentration of 5 g/L was evaluated on the properties of the

$70Li_2S:30P_2S_5$ sample. Table 1.3 shows the parameters used for the liquid-phase synthesis procedure.

Figure 1.11 shows the XRD pattern of the $70Li_2S:30P_2S_5$ sample after the drying process at 180 °C and after subsequent heat treatment at 220 °C. The XRD pattern of the sample obtained after the drying process at 180 °C exhibited peaks corresponding to the PS_4^{3-}·ACN complex. Additional XRD peaks at the 2θ position of 27° and 31.25° were assigned to the Li_2S precursor. The XRD pattern of the sample obtained after subsequent heat treatment at 220 °C, exhibited peaks corresponding to the $Li_7P_3S_{11}$ crystal phase. Peaks corresponding to the Li_2S precursor were also observed after the heat treatment.

The $70Li_2S:30P_2S_5$ sample obtained using the mass concentration of 5 g/L exhibited a similar reaction state to that of the $74Li_2S:26P_2S_5$ sample obtained using the mass concentration of 50 g/L described in the first section of this part (Figure 1.6). After heat treatment at 220 °C, both samples exhibit XRD peaks corresponding to the $Li_7P_3S_{11}$ crystal phase and additional XRD peaks corresponding to the Li_2S precursor. These results elucidate the difficult incorporation of Li_2S. It is believed that the larger mass concentration of 50 g/L is not favorable for the reaction of Li_2S, and that variations in the stoichiometry can be ascribed to the difficult incorporation of the precursor Li_2S. Hence, the excess of Li_2S, for example, in the composition $74Li_2S:26P_2S_5$, is necessary to compensate its difficult incorporation when using the larger mass concentration of 50 g/L.

TABLE 1.3. Parameters used for the liquid-phase synthesis (section 3)

Parameter	Value
Mass concentration	5 g/L
Ultrasonication time	30 min

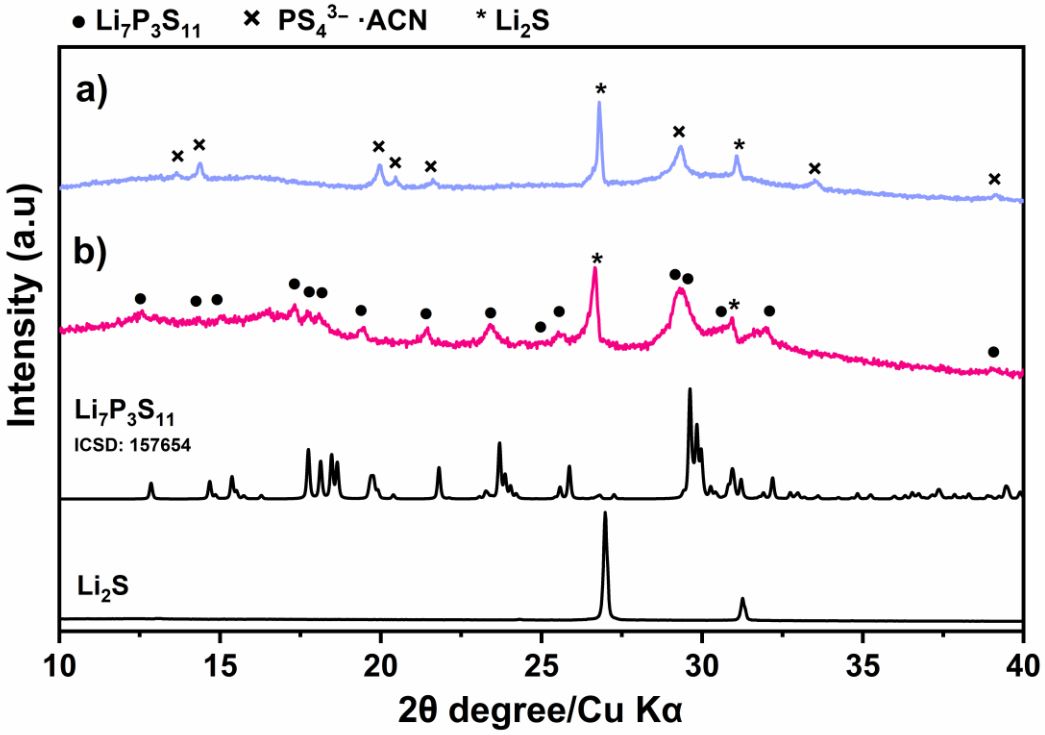

Figure 1.11 XRD patterns of the $70Li_2S{:}30P_2S_5$ solid electrolyte **a)** after the drying process at 180 °C and **b)** after subsequent heat treatment at 220 °C. The mass concentration of 5 g/L was used in the synthesis procedure.

Effect of the ultrasonic irradiation

To obtain a solid electrolyte containing the $Li_7P_3S_{11}$ crystal phase without mayor impurities derived from unreacted precursors, the ultrasonic irradiation time was studied for the synthesis using the mass concentration of 5 g/L.

Ultrasonic irradiation was applied for periods of 30 minutes until the total time of 180 minutes. After each period, the sample, corresponding to the slurry state, was evaluated by X-ray diffraction. The ultrasonic irradiation was carried out at room temperature to evaluate only its effect.

Figure 1.12a show the XRD patterns of the $70Li_2S{:}30P_2S_5$ sample obtained after 30, 60, 90, 120, 150 and 180 minutes of ultrasonic irradiation. Shifts in the XRD peaks can be attributed to the presence of acetonitrile in the slurry. After 30 min of ultrasonic irradiation, peaks corresponding to the $PS_4^{3-}{\cdot}ACN$ complex were observed. However, peaks corresponding to the Li_2S precursor were also observed. During the following periods, until reach the total ultrasonication time of 120 minutes, the intensity of the XRD peak corresponding to the Li_2S precursor was greatly reduced. Application of ultrasonic irradiation for longer time than 120 minutes did not result in a further decrease in the intensity of the XRD peak corresponding to the Li_2S precursor. The presence of unreacted Li_2S was also detected in solid electrolytes prepared by using magnetic stirring for three days [33].

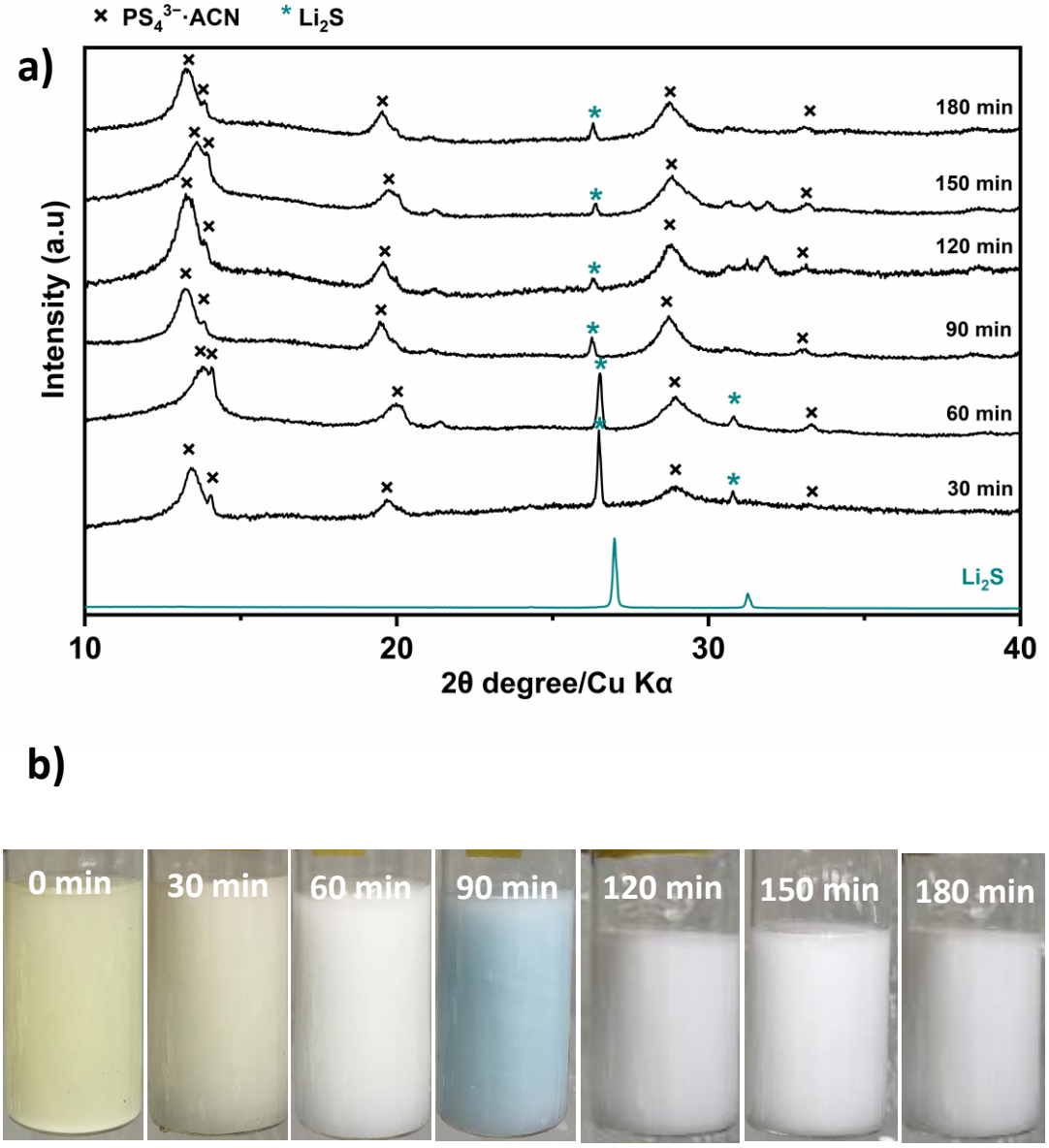

Figure 1.12 a) XRD patterns and **b)** Photographs of the material state of the $70Li_2S{:}30P_2S_5$ sample obtained after 30, 60, 90, 120, 150 and 180 minutes of ultrasonic irradiation.

Unreacted Li_2S was attributed to the possible formation of passivation layers that would prevent its complete conversion.

Figure 1.12b shows photographs of the material state after each period. Before the application of ultrasonic irradiation, the sample exhibited a white precipitate and a yellowish solution. After 30 minutes of applying ultrasonic irradiation, the sample corresponded to a yellowish suspension. After 60 min, the suspension turned white. After 90 min, the white suspension turned blue. The blue color can be associated with the possible formation of polysulfides as intermediates in the reaction pathway. After 120 minutes, the suspension turned white again and no change was observed after further application of ultrasonic irradiation, as also was not observed any change in the XRD patterns.

After 180 minutes of ultrasonic irradiation, the sample was dried under vacuum at 180 °C. Subsequently, heat treatment at 220 °C was applied. Figure 1.13 shows the XRD patterns of the solid electrolyte after drying at 180 °C, and after the subsequent heat treatment at 220 °C. The main formation of the $Li_7P_3S_{11}$ crystal phase was observed, and a minor impurity corresponding to unreacted Li_2S

Discussion and Summary

The effect of the mass concentration on favoring the reaction between Li_2S and P_2S_5 was evaluated. As expected, the smaller mass concentration of 5 g/L favored the reaction and allowed to obtain the $Li_7P_3S_{11}$ crystal phase in the solid electrolyte with a stoichiometric composition of $70Li_2S{:}30P_2S_5$.

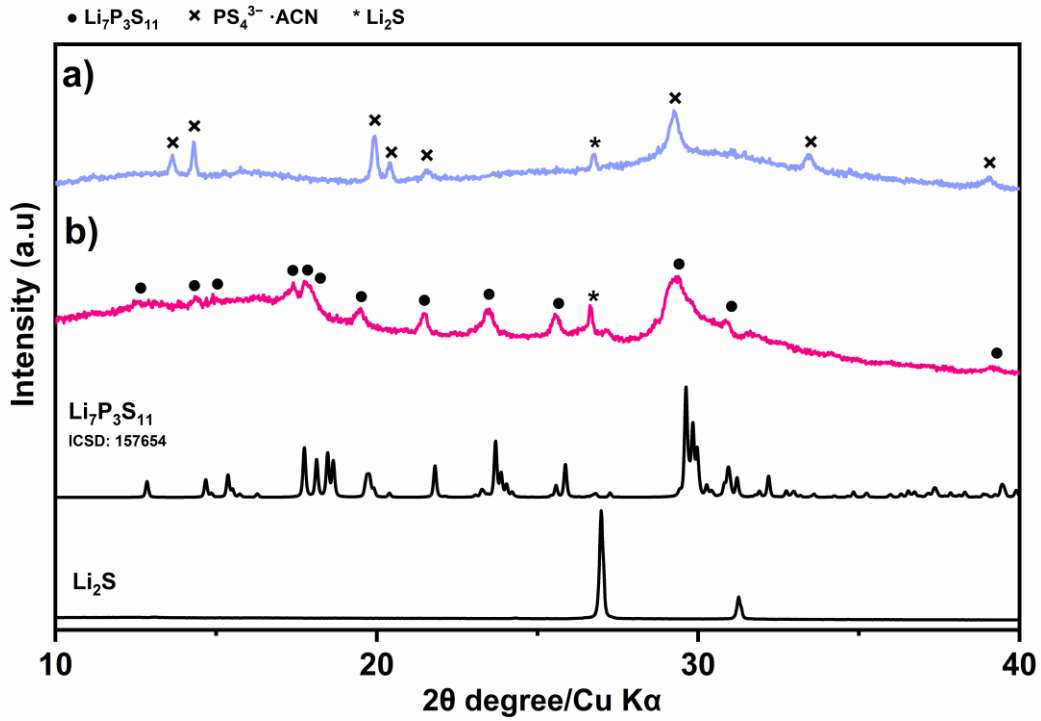

Figure 1.13 XRD patterns of the $70Li_2S{:}30P_2S_5$ solid electrolyte **a)** after the drying process at 180 °C and **b)** after subsequent heat treatment at 220 °C. The mass concentration of 5 g/L and a total ultrasonication time of 180 minutes were used in the synthesis procedure.

The time of ultrasonic irradiation necessary to complete the reaction was evaluated. It was found that: 1) The reaction proceeds at room temperature, and 2) Application of ultrasonic irradiation for 120 minutes at room temperature, is enough to obtain the PS_4^{3-}·ACN complex, with only a minor impurity corresponding to Li_2S. The difficult incorporation of Li_2S may indicate the possible formation of passivation layers that prevent its complete reaction.

4. Formation mechanism of the $Li_7P_3S_{11}$ crystal phase through liquid-phase synthesis.

The $Li_7P_3S_{11}$ crystal phase is formally obtained from Li_2S and P_2S_5 in the stoichiometric ratio of 70:30 in mol% and is formed by pyro-thiophosphate ($P_2S_7^{4-}$) and ortho-thiophosphate (PS_4^{3-}) structural units in a ratio of 1:1 [27]. In the $P_2S_7^{4-}$ and PS_4^{3-} units, the S atoms are bonded to P^V centers, sharing the oxidation state of P with the starting precursor P_2S_5.

The P_2S_5 precursor, properly described as the P_4S_{10} adamantine-like molecule, is composed of PS_4 polyhedra connected by P-S-P bridges. The incorporation of Li_2S increases the sulfur content, breaking the P-S-P bridges and introducing terminal sulfur atoms, with Li^+ acting as the counterion.

By mechanical milling, the reagents suffer an amorphization, and $P_xS_y^{z-}$ polyhedra are formed according to the Li_2S incorporation. In the Li_2S:P_2S_5 stoichiometric ratio of 75:25 mol%, Li_2S is enough to break all the P-S-P bridges in the P_4S_{10} molecule and obtain only PS_4^{3-} polyhedra, in which all sulfur atoms are terminal. For Li_2S:P_2S_5 stoichiometric ratio of 70:30 mol%, Li_2S is not enough to break all P-S-P bridges, which results in the formation of $P_2S_7^{4-}$ polyhedra. The $P_2S_7^{4-}$ polyhedron consist of two PS_4^{3-} polyhedra connected by a P-S-P bridge.

A minor presence of hypo-thiodiphosphate ($P_2S_6^{4-}$) units has been observed in glasses with different stoichiometries, with Li_2S content from 60 to 80 mol%, that had been prepared by mechanical milling [34]. However, the formation of $P_2S_6^{4-}$ units corresponds to an undesirable decomposition during the syntheses.

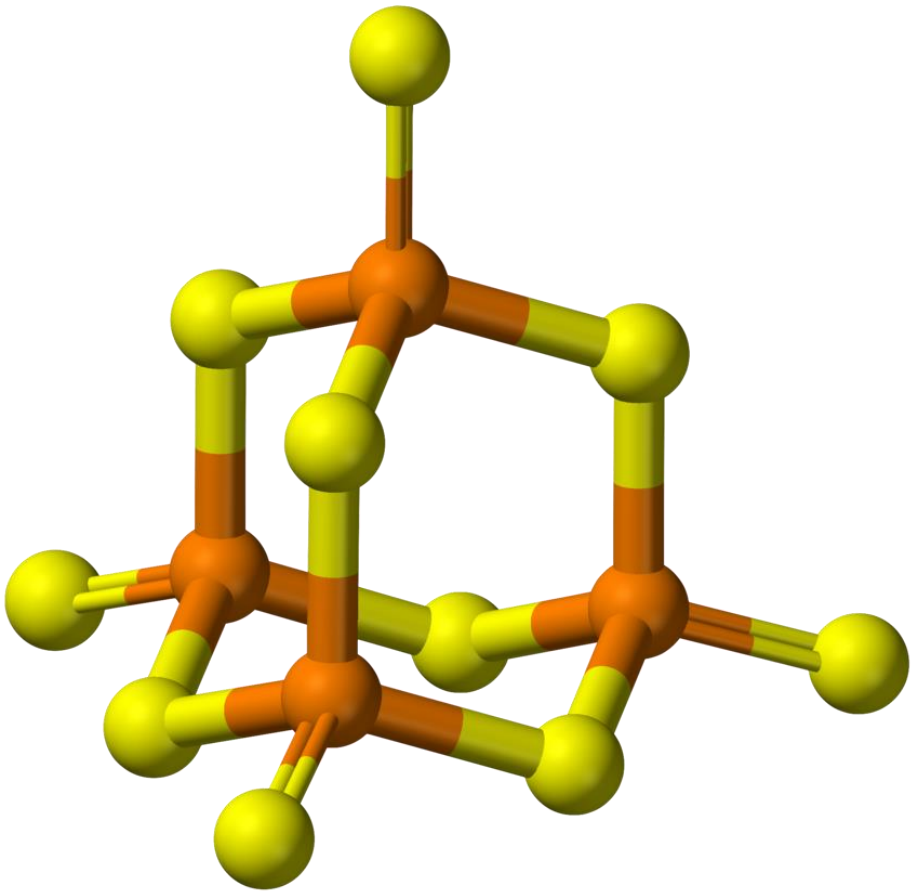

Figure 1.14 Molecular structure of Phosphorus(V) sulfide

In the common thiophosphate polyhedra, the S atoms are bonded to P^{V} centers (with the same oxidation state of P as the precursor P_4S_{10}). On the other hand, $P_2S_6^{4-}$ units contain a P-P bond with P^{IV} centers, which implies a reduction of P^{V} to P^{IV}. In the following discussion, this undesirable formation of the P-P bond will not be taken into account to maintain simplicity.

The $Li_7P_3S_{11}$ crystal phase is formed in glasses with stoichiometry composition of $70Li_2S{:}30P_2S_5$ in mol%, prepared by mechanical milling, upon heat treatment at 250 °C - 350 °C. Via liquid-phase, a different crystallization process was observed. To understand the reaction mechanisms that take place in the liquid-phase synthesis, the focus was placed first on the precursors.

Precursors solubility

Figure 1.15a displays a mixture of P_2S_5 and acetonitrile, in the same amount used for the synthesis with mass concentration of 5g/L (Table 1.3). The mixture consisted of a yellow powder and a yellowish suspension.

Figure 1.15b displays a mixture of Li_2S in acetonitrile, in the same amount used for the synthesis with mass concentration of 5g/L (Table 1.3). The mixture consisted of a white powder and a bluish suspension. The blue color in the literature has been associated with the presence of the polysulfide anion S_3^- [35, 36]. The formation of such polysulfides has been explored in the close field of Li-S batteries [37], and it also has been found that solvents such as

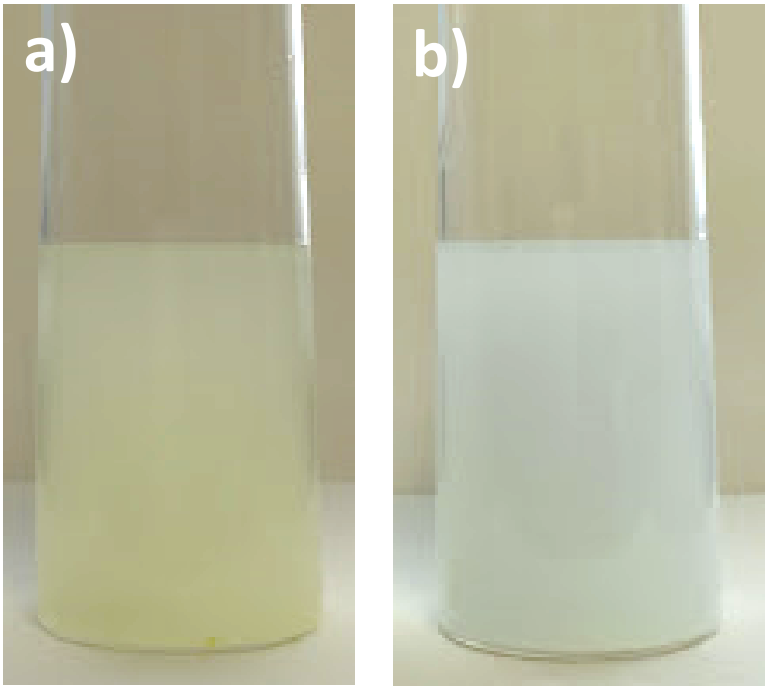

Figure 1.15 a) Mixture of P_2S_5 and acetonitrile, and **b)** mixture of Li_2S with acetonitrile

acetonitrile can stabilize them [38]. Although, deeper characterization of the solutions is necessary, the blue color observed in the mixture of Li_2S and acetonitrile, and also observed during the liquid-phase synthesis of sulfide electrolytes with acetonitrile as solvent (Figure 1.12b), can be associated to the possible formation of polysulfides as intermediates in the reaction pathway.

Figure 1.16 displays mixtures of Li_2S and P_2S_5 in acetonitrile with Li_2S:P_2S_5 stoichiometric compositions of 50:50, 60:40 and 70:30 in mol%. The mass concentration corresponds to 5 g/L. While both Li_2S and P_2S_5 exhibits negligible solubility in acetonitrile, both in the stoichiometric composition of 50:50 mol%, produced a transparent yellow solution. The further addition of Li_2S resulted in a white precipitate. Similar behavior has been observed in solvents such as ethyl propionate [39, 40].

Formation of the *meta*-thiodiphosphate $P_2S_6^{2-}$ anion

The transparent yellow solution containing Li_2S and P_2S_5 in the stoichiometric composition of 50:50 mol% was investigated. The yellow solution was dried at 180 °C under vacuum and subsequently heat treated at 220 °C. An additional sample was dried at the lower temperature of 100 °C under vacuum, for comparison. The $50Li_2S$:$50P_2S_5$ sample was characterized by X-ray diffraction and Raman spectroscopy after each step of the synthesis.

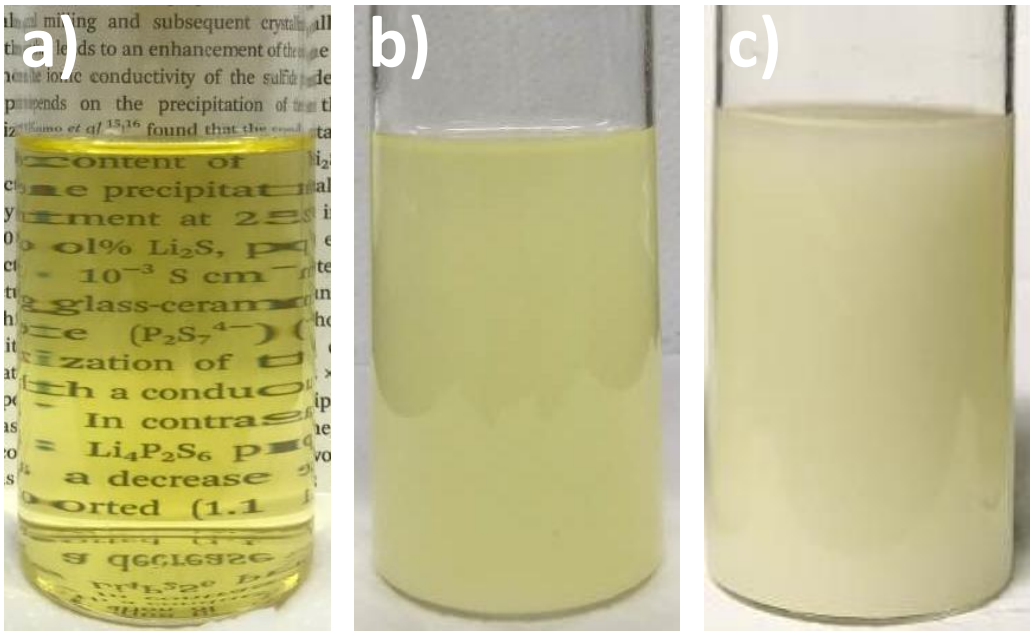

Figure 1.16 Mixtures of Li_2S and P_2S_5 in acetonitrile, in the Li_2S:P_2S_5 stoichiometric compositions of **a)** 50:50, **b)** 60:40 and **c)** 70:30 in mol%.

Figure 1.17 shows XRD patterns of the $50Li_2S:50P_2S_5$ sample after drying at 100 °C or 180 °C under vacuum and after drying at 180 °C and subsequent heat treatment at 220 °C. After drying at 100 °C, the $50Li_2S:50P_2S_5$ sample exhibited an amorphous structure. After drying at 180 °C, the sample crystallized in an unknown crystal structure. After drying at 180 °C and subsequent heat treatment at 220 °C, peaks corresponding to the $Li_2P_2S_6$ crystal phase were observed.

The local structure of the $Li_2P_2S_6$ crystal phase is formed by $P_2S_6^{2-}$ polyhedral [41]. In contrast to the $P_2S_6^{4-}$ units, containing a P−P bond, the $P_2S_6^{2-}$ units consists of two edge-sharing PS_4 tetrahedra. The $P_2S_6^{2-}$ units were reported to exhibit two Raman peaks at 421 cm^{-1} and 395 cm^{-1} [41]. The most intense peak at 421 cm^{-1} was assigned to the symmetric stretching mode of the P-S-P-S ring [41]. For a better understanding, the local structure of the $50Li_2S:50P_2S_5$ sample, here synthesized, was examined after each step of the synthesis, by using Raman spectroscopy.

Figure 1.18 shows the Raman spectra of the $50Li_2S:50P_2S_5$ sample after drying at 100 °C or 180 °C under vacuum, and after drying at 180 °C and subsequent heat treatment at 220 °C. The Raman spectrum of the sample after drying at 100 °C, exhibited a major band centered at 390 cm^{-1}, its assignment is discussed below. Raman bands centered at 235 cm^{-1}, 311 cm^{-1}, 500 cm^{-1}, 560 cm^{-1}, 585 cm^{-1}, 650 cm^{-1} and 675 cm^{-1} are not attributed to the PS_4^{3-}, $P_2S_7^{4-}$ or $P_2S_6^{4-}$ thiophosphate units, neither to Li_2S or P_2S_5 precursors. The Raman bands centered at 900 cm^{-1}, 1370 cm^{-1}, 2200 cm^{-1} and 2900 cm^{-1} are attributed to the C-C stretch, C-H bend, C≡C stretch and C-H bending vibrations of acetonitrile [24, 25].

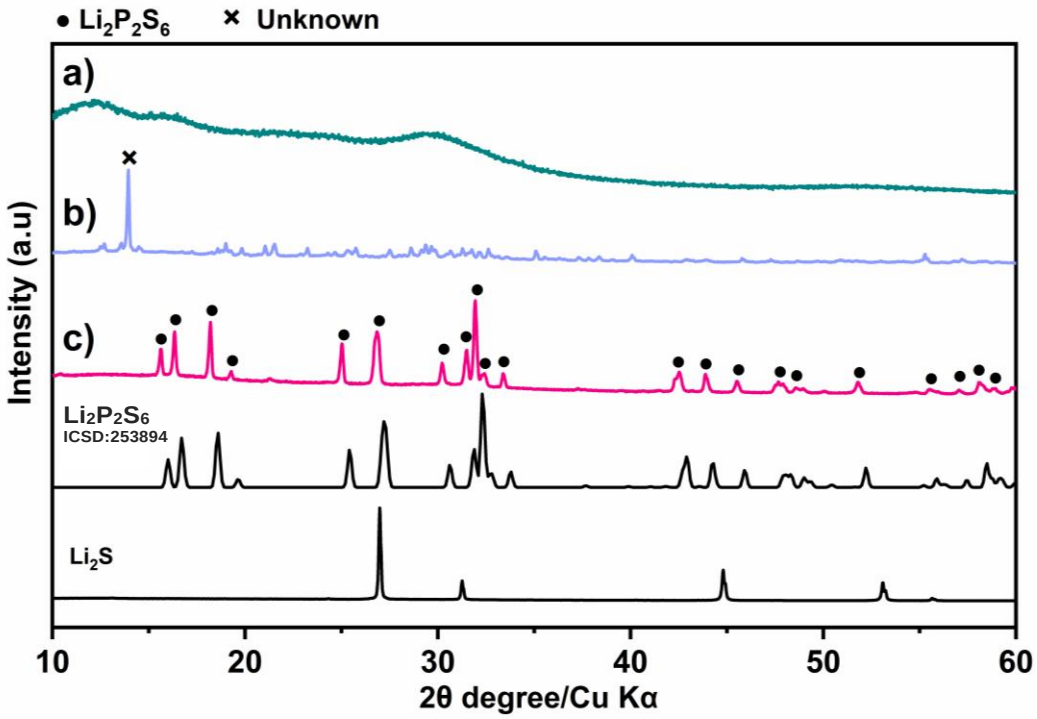

Figure 1.17 XRD patterns of the $50Li_2S{:}50P_2S_5$ sample **a)** after drying at 100 °C, **b)** after drying at 180 °C and **c)** after drying at 180 °C and subsequent heat treatment at 220 °C. Indexed diffraction pattern of the $Li_2P_2S_6$ crystal phase (ICSD:253894) is shown for comparison.

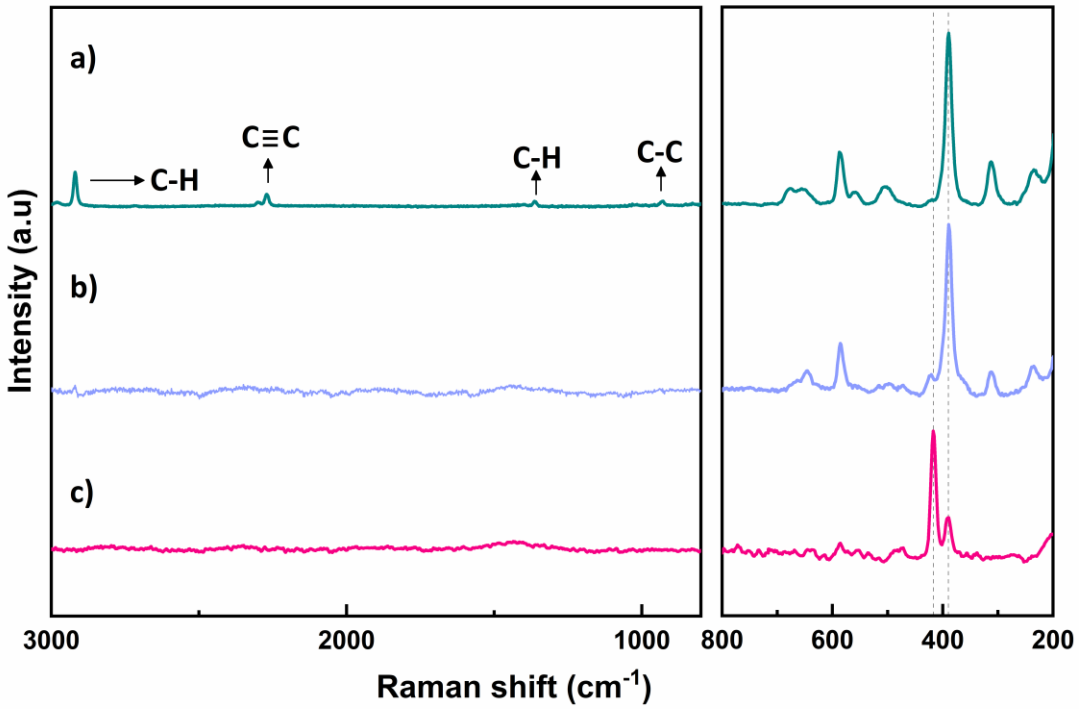

Figure 1.18 Raman spectra of the $50Li_2S:50P_2S_5$ sample **a)** after drying at 100 °C, **b)** after drying at 180 °C and **c)** after drying at 180 °C and subsequent heat treatment at 220 °C.

The Raman spectrum of the sample after drying at 180 °C, exhibited a similar spectrum to that of the sample after drying at 100 °C, at the lower Raman shift. At the higher Raman shift, the Raman bands attribute to acetonitrile were no longer observed.

The Raman spectrum of the sample after heat treatment at 220 °C, exhibited mainly two bands centered at 390 cm^{-1} and 417 cm^{-1}. In good agreement with the report of Dietrich et al. [41], the Raman spectrum of the $Li_2P_2S_6$ solid electrolyte obtained after the heat treatment at 220 °C (Figure 1.18c), exhibited an intense peak at 417 cm^{-1} and an additional peak at 390 cm^{-1}. Hence, it was confirmed that the local structure of the solid electrolyte containing the $Li_2P_2S_6$ crystal phase was composed of $P_2S_6^{2-}$ units.

The Raman band located at 417 cm^{-1}, associated to the P-S-P-S ring in the $P_2S_6^{2-}$ units, was not observed in the sample obtained after drying at 100 °C and was observed only in a small proportion in the sample obtained after drying at 180 °C. These large chemical changes in the $Li_2P_2S_6$ solid electrolyte upon crystallization has been observed before, by using NMR spectroscopy [42]. Eckert et al. suggested that the structure of a $Li_2P_2S_6$ glass, prepared by melt-quenching, was formed by corner-sharing units (PS_3^- chains), that upon crystallization, would form the $P_2S_6^{2-}$ edge-sharing units [42]. While at this moment no report on the Raman spectra of such polymerics species of corner-sharing units has been reported, under the proposed by Eckert et al. [42], the band located at 390 cm^{-1} in the Raman spectra of the $50Li_2S{:}50P_2S_5$ sample, reported in this work, could be assigned to the $(PS_3^-)_n$ polymeric chains.

The $P_2S_6^{2-}$ edge-sharing units that constitute a violation of the Zachariasen bonding principle [44] have been found possible in crystalline materials in the Li_2S-P_2S_5 [42] or Li_2S-SiS_2 [43] systems, however, the tendency to find them in the glassy state is much less pronounced. In good agreement, the Raman band at 417 cm^{-1}, attributed to the P-S-P-S ring was only observed after crystallization, and not in the amorphous material.

Scheme 1.2 illustrates the possible reaction pathway for the formation of the meta-thiodiphosphate $P_2S_6^{2-}$ anion through liquid-phase. It is generally accepted that P_4S_{10} can dissociate into the reactive P_2S_5 under the refluxing of solvents such as acetonitrile (Scheme 1.3) [44]. It is believed that in the synthesis of Li_2S-P_2S_5 sulfide electrolytes by liquid-phase using acetonitrile as the solvent, the dissociation of P_4S_{10} into P_2S_5 through acetonitrile mediation would provide the initial step for the reaction. P_2S_5 with the unfavorable $\sigma^3\lambda^5$ bonding situation is unstable unless the missing forth coordination partner is provided [45]. This is believed to be the driving force for the rapid reaction with Li_2S in 1:1 mol%. The results found in the liquid-phase synthesis of $Li_2P_2S_6$, suggest that P_2S_5 and Li_2S would react to form $(PS_3^-)_n$ chains. Heat treatment at temperatures above 220 °C would provide the necessary energy to break half of the P-S-P bonds in the $(PS_3^-)_n$ chains and form the meta-thiodiphosphate $P_2S_6^{2-}$ units.

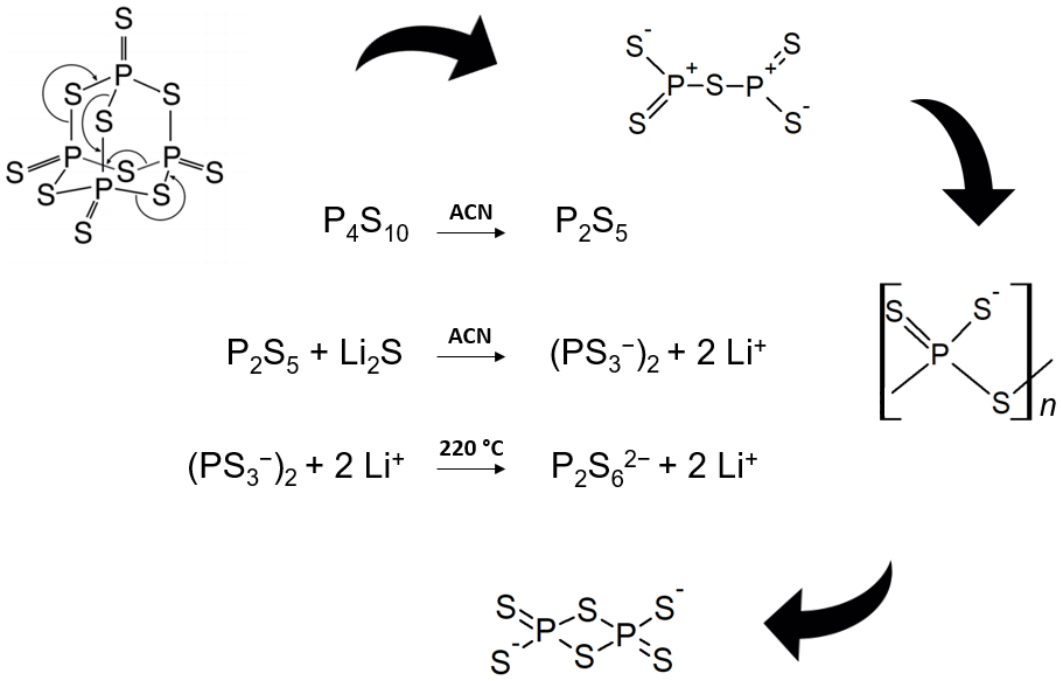

Scheme 1.2. Possible reaction pathway for the formation of the meta-thiodiphosphate $P_2S_6^{2-}$ anion.

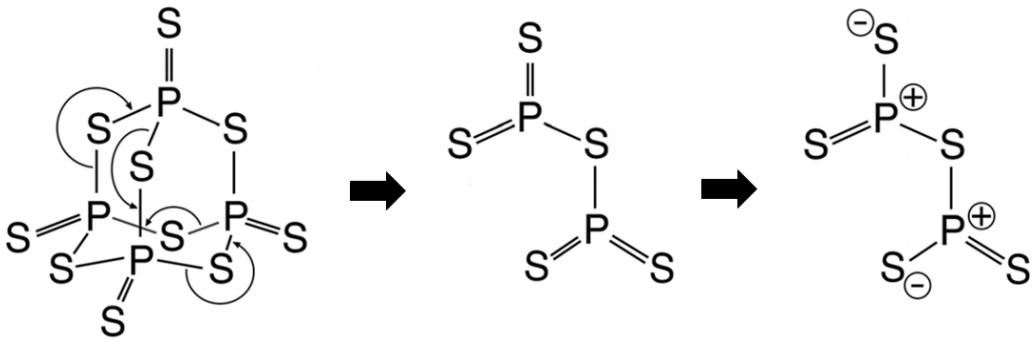

Scheme 1.3. Dissociation mechanism of P_4S_{10} [44]

Formation of the *ortho*-thiophosphate PS_4^{3-} anion

Formally, PS_4^{3-} units are formed from the stoichiometric composition $3Li_2S:1P_2S_5$ ($75Li_2S:25P_2S_5$ mol%), with an excess of Li_2S in comparison to the composition with the 1:1 molar ratio ($50Li_2S:50P_2S_5$ mol%).

It can be expected than in the first step of the synthesis, Li_2S and P_2S_5 in the 1:1 molar ratio react to form $(PS_3^-)_n$ polymeric chains. Further, the incorporation of Li_2S increase the sulfur content, breaking all P-S-P bridges and incorporating terminal sulfur with Li^+ acting as the counterion. Scheme 1.4 illustrates the possible reaction pathway for the formation of the ortho-thiodiphosphate PS_4^{3-} anion through liquid-phase.

As PS_4^{3-} units are formed, acetonitrile molecules complexed with them and form a crystalline structure as has been discussed before (Figure 1.12a). This complex formation between PS_4^{3-} units and solvent molecules is not unique to acetonitrile. Solvents such as tetrahydrofuran [10], ethyl acetate [13], dimethyl carbonate [15] and 1,2-dimethoxyethane [46] have also been reported to form complexes with PS_4^{3-} units. However, among all the solvents, acetonitrile exhibits a stronger binding with the PS_4^{3-} units. A complex of PS_4^{3-} units with THF, EA, DMC and DME solvents dissociates at temperatures around 100 °C. In the case of acetonitrile, almost double of this temperature is necessary (above 180 °C). The acetonitrile stronger binding can be attributed to its relatively high polarity and small size.

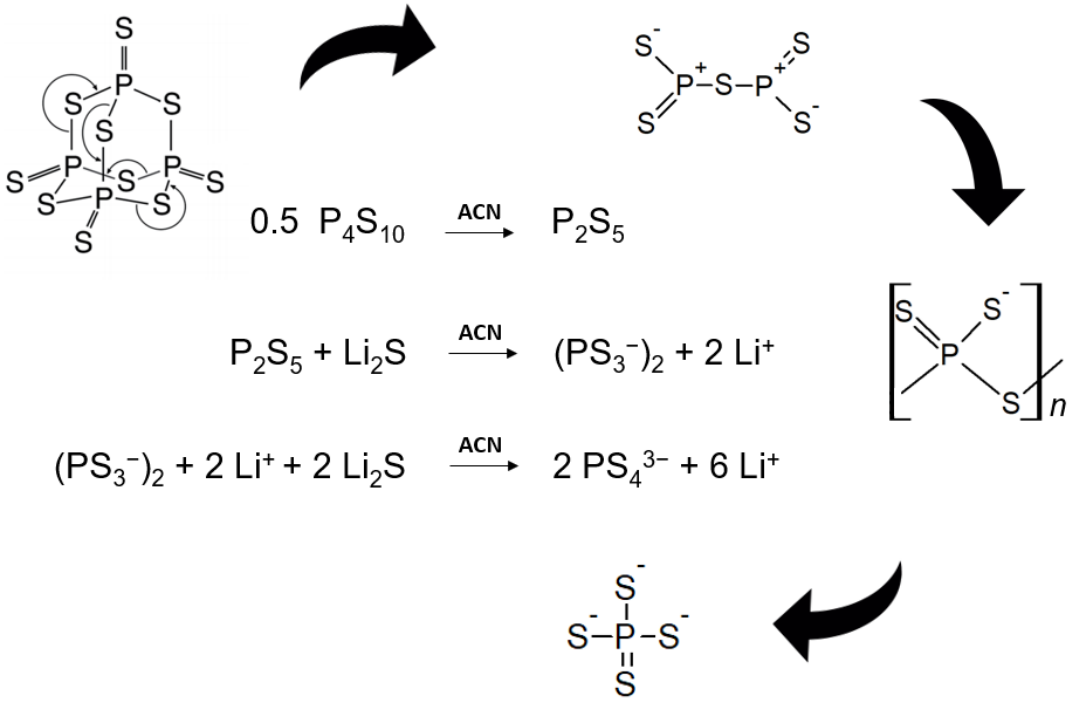

Scheme 1.4. Possible reaction pathway for the formation of the ortho-thiodiphosphate PS_4^{3-} anion.

Formation of the *pyro*-thiodiphosphate $P_2S_7^{4-}$ anion

$P_2S_7^{4-}$ units have been found in Li_2S-P_2S_5 glasses, prepared by mechanical milling, in compositions with Li_2S content from 60 to 75 mol% [34]. In the mechanical milling process, the increase in the sulfur content due to Li_2S incorporation breaks the P-S-P bridges in the P_4S_{10} molecule, and $P_xS_y^{z-}$ units are formed according to the Li_2S incorporation. On the other hand, no similar reaction process has been found in the liquid-phase synthesis.

Through liquid-phase, PS_4^{3-} units are readily formed in Li_2S:P_2S_5 compositions with Li_2S content more than 50 mol%. However, the formation of $P_2S_7^{4-}$ units has been found only after the dissociation of the PS_4^{3-}·ACN complex and heat treatments over 220 °C. Similar results have been found recently by Wang et al. [33]. In the synthesis of a $70Li_2S$:$30P_2S_5$ sample by liquid-phase using acetonitrile as the solvent, if the precipitated phase is separated from the supernatant, after heat treatment, the precipitated phase crystallizes in the β-Li_3PS_4 crystal phase, and the supernatant crystallizes in the $Li_2P_2S_6$ and $Li_4P_2S_6$ crystal phases. No formation of $P_2S_7^{4-}$ units is found in the precipitated phase neither in the supernatant [33]. These results suggest that $P_2S_7^{4-}$ units may not be stable in solution. Hence, the formation of $P_2S_7^{4-}$ units would be attributed to reactions between PS_4^{3-} units and $(PS_3^-)_n$ chains to achieve redox-equilibria upon heat treatment. Scheme 1.5 illustrates the proposed reaction pathway for the formation of the *pyro*-thiodiphosphate $P_2S_7^{4-}$ units.

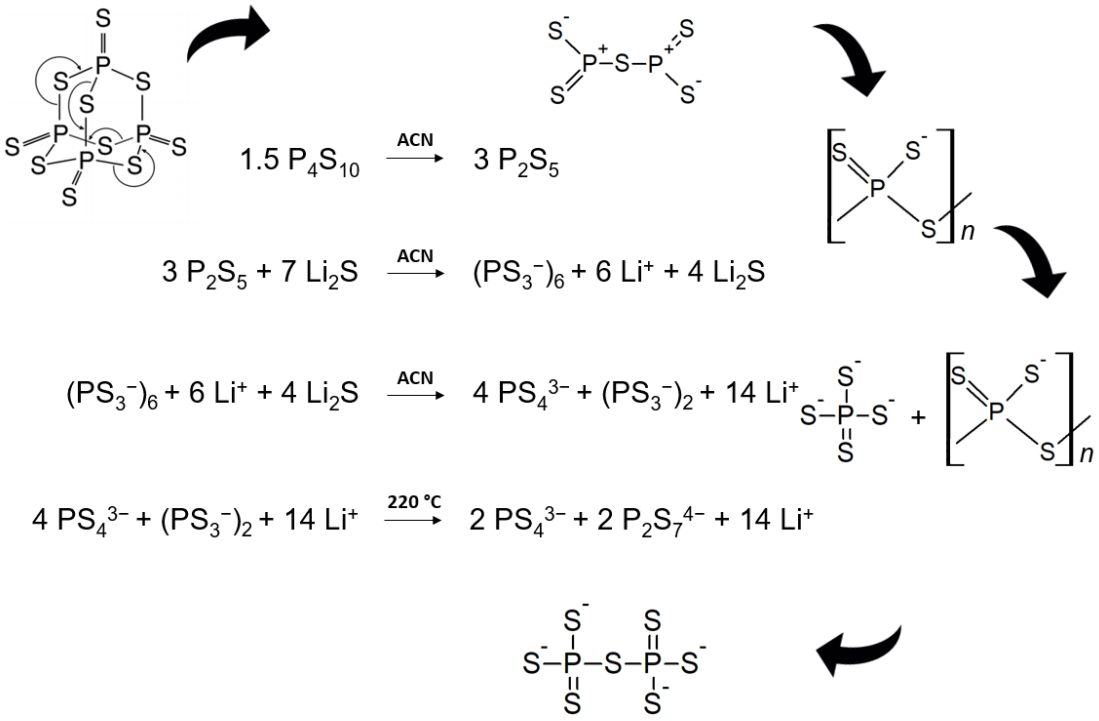

Scheme 1.5. Possible reaction pathway for the formation of the *pyro*-thiodiphosphate $P_2S_7^{4-}$ anion.

As discussed above, $(PS_3^-)_n$ chains proceed to the formation of $P_2S_6^{2-}$ units upon heat treatment. A preferable formation of the corner-sharing $P_2S_7^{4-}$ units over the edge-sharing $P_2S_6^{2-}$ units can be expected. However, the formation of $P_2S_7^{4-}$ units would require an S^0 transfer from the PS_4^{3-} units. This redox processes in the PS_4^{3-} anion has been observed before [47]. Although, only speculation at this point, the following redox reactions are proposed:

$$2\ PS_4^{3-} + 6\ Li^+ \longrightarrow P_2S_7^{4-} + 4Li^+ + S^0 + 2Li^+ \quad (1)$$

$$2\ PS_3^- + 2Li^+ + S^0 + 2\ Li^+ \longrightarrow P_2S_7^{4-} + 4Li^+ \quad (2)$$

The Li_2S-P_2S_5 materials containing PS_4^{3-} and $P_2S_7^{4-}$ units, crystallized in the high ionic conductive $Li_7P_3S_{11}$ crystal phase with heat treatment above 220 °C, similar to the findings of Mizuno et al., in the materials prepared by mechanical milling [32].

Discussion and summary

The special focus on the Li_2S and P_2S_5 precursors and their reaction in 50:50 mol% allowed the understanding of the initial chemical reactions that trigger the formation of the $P_xS_y^{z-}$ thiophosphate units.

Li_2S and P_2S_5 in the stoichiometric composition of 50:50 mol% readily dissolve in acetonitrile to form a clear yellowish solution. After the drying process at 100 °C, an amorphous structure was observed by X-ray diffraction. The amorphous structure crystallizes into an unknown structure at 180 °C and crystallized in the $Li_2P_2S_6$ crystal phase at the slightly higher temperature of 220 °C. In good agreement with the X-ray diffraction measurements, the Raman spectra of the sample exhibited large local structural changes in the sample upon crystallization.

The $Li_2P_2S_6$ crystal phase, which local structure is formed by $P_2S_6^{2-}$ units, is only observed after heat treatment at 220 °C, in good agreement, the Raman band corresponding to the P-S-P-S ring in the $P_2S_6^{2-}$ units, is clearly observed only after heat treatment. These results and previous NMR studies by Eckert et al. [42] suggest that the $50Li_2S{:}50P_2S_5$ sample is formed by polymeric chains composed of PS^{3-} units, prior to the crystallization.

The formation of such $[PS_3^-]_n$ polymeric chains with high solubility would constitute the initial step of the reaction to form the $P_xS_y^{z-}$ units. The possible reaction pathways for the formation of the meta-thiodiphosphate $P_2S_6^{2-}$, the ortho-thiodiphosphate PS_4^{3-} and the *pyro*-thiodiphosphate $P_2S_7^{4-}$ anions was hypothesized.

The increase of the Li_2S content to the $50Li_2S{:}50P_2S_5$ sample, would break the P-S-P bonds in the $[PS_3^-]_n$ polymeric chains to form PS_4^{3-} units. The formed PS_4^{3-} units complexed then with acetonitrile molecules to form a particular crystal structure. The PS_4^{3-}·ACN complex dissociates only at temperatures above 180 °C.

Although, a similar process can be expected for the formation of $P_2S_7^{4-}$ units, experimental results indicate that the $P_2S_7^{4-}$ units are not stable in the solution (slurry state). Raman bands corresponding to the $P_2S_7^{4-}$ units were observed only after heat treatments at temperatures above 180 °C. The possible formation mechanism of $P_2S_7^{4-}$ units would be associated with redox processes that take place at the dissociation of the PS_4^{3-}·ACN complex. PS_4^{3-} units would undergo redox reactions to form $P_2S_7^{4-}$ units and sulfur as a sub product. The sulfur provided by the redox reactions would react with the remaining $[PS_3^-]_n$ polymeric chains to also form $P_2S_7^{4-}$ units. The materials containing PS_4^{3-} and $P_2S_7^{4-}$ units crystallizes in the high ion conductive $Li_7P_3S_{11}$ crystal phase.

Summary

This part reported the preparation of Li_2S-P_2S_5 solid electrolytes by liquid-phase process. Li_2S and P_2S_5 were used as the precursors and acetonitrile as the medium for the reaction. The application of ultrasonic irradiation was found to enhance the reaction in comparison to the magnetic stirring method. The time for the reaction was reduced from days to minutes (30-180 min). After the application of ultrasonic irradiation, the solvent was removed at 180 °C under vacuum, and heat treatment at 220 °C was subsequently applied.

Li_2S-P_2S_5 solid electrolytes containing the $Li_7P_3S_{11}$ crystal phase were obtained for compositions with Li_2S content from 70 to 75 mol%. A Li_2S impurity was also found in all compositions. Although the $Li_7P_3S_{11}$ crystal phase was identified in all the compositions, the distribution of $P_xS_y^{z-}$ thiophosphate units (PS_4^{3-}, $P_2S_7^{4-}$ and $P_2S_6^{4-}$) in the local structure of the solid electrolytes was different for each composition. The solid electrolyte with Li_2S content of 74 mol%, exhibited a high ionic conductivity up to 10^{-3} Scm^{-1}. The presence of $P_2S_7^{4-}$ units (respect to PS_4^{3-} and $P_2S_6^{4-}$ units), in the solid electrolyte with Li_2S content of 74 mol%, was found higher compared to the other samples. It can be inferred that the high content of $P_2S_7^{4-}$ units in the structure of the Li_2S-P_2S_5 sulfide solid electrolytes resulted in the formation of high ionic conductive materials.

The crystallization process that takes place in the liquid-phase process was studied in the Li_2S-P_2S_5 solid electrolyte with Li_2S content of 74 mol%. Crystal and local structure, morphology and impedance were studied after each step of the synthesis. The formation of PS_4^{3-} units was observed, by Raman

spectroscopy, after only 30 minutes of ultrasonic irradiation. X-ray diffraction and Raman spectroscopy studies revealed the complex formation between PS_4^{3-} units and acetonitrile molecules, named here as PS_4^{3-}·ACN. The PS_4^{3-}·ACN complex was dissociated upon heat treatment at 220 °C. The dissociation of the complex was accompanied by the formation of $P_2S_7^{4-}$ units resulting in the precipitation of the $Li_7P_3S_{11}$ crystal phase. The crystallization of the high ionic conductive $Li_7P_3S_{11}$ crystal phase led to an increase in the ionic conductivity of three orders of magnitude, from 1.4 x 10^{-6} to 1 x 10^{-3} Scm^{-1}.

Particularly, the solid electrolyte exhibited a particle size of around 500 nm, more than ten times smaller compared with the particle size obtained by mechanical milling, revealing the potential of the liquid-phase process to control the morphology of the sulfide solid electrolytes.

In the effort to preserve the stoichiometry, the effect of the mass concentration and the effect of the ultrasonic irradiation time on the properties of the $70Li_2S{:}30P_2S_5$ solid electrolyte were studied. A mass concentration of 5 g/L and a longer time for ultrasonication (120 – 180 min.) was effective in obtaining a solid electrolyte containing the $Li_7P_3S_{11}$ crystal phase, with minor impurities, from the stoichiometric composition of $70Li_2S{:}30P_2S_5$ in mol%.

Finally, the formation mechanism of the $Li_7P_3S_{11}$ crystal phase through liquid-phase process was hypothesized. Contrary to the mechanical milling process, in which the incorporation of Li_2S results in the breaking of the P-S-P bridges in the P_4S_{10} molecule, forming the $P_XS_y^{z-}$ thiophosphate units; via liquid-phase, the reaction would proceed to the only formation of PS_4^{3-} units through intermediates $[PS_3^-]_n$ polymeric chains.

The possible formation mechanism of the $P_2S_7^{4-}$ units is associated to redox reactions between PS_4^{3-} units and remaining $[PS_3^-]_n$ chains, at the temperature of the PS_4^{3-}·ACN complex dissociation (> 180° C). The formation of the $P_2S_7^{4-}$ units in Li_2S-P_2S_5 solid electrolytes resulted in the crystallization of the $Li_7P_3S_{11}$ crystal phase.

References

[1] R. Mercier, J.-P. Malugani, B. Fahys, G. Robert, Superionic conduction in Li_2S-P_2S_5-LiI-glasses, Solid State Ionics 5 (1981) 663-666.

[2] R. Mercier, J. Malugani, B. Fahys, J. Douglande, G. Robert, Synthese, structure cristalline et analyse vibrationnelle de l'hexathiohypodiphosphate de lithium $Li_4P_2S_6$, J. Solid State Chem. 43(2) (1982) 151-162.

[3] R. Mercier, J.-P. Malugani, B. Fahys, G. Robert, J. Douglade, Structure du tetrathiophosphate de lithium, Acta Crystallographica Section B: Structural Crystallography and Crystal Chemistry 38(7) (1982) 1887-1890.

[4] A. Hayashi, S. Hama, H. Morimoto, M. Tatsumisago, T. Minami, Preparation of Li_2S–P_2S_5 amorphous solid electrolytes by mechanical milling, J. Am. Ceram. Soc. 84(2) (2001) 477-79.

[5] Ö.U. Kudu, T. Famprikis, B. Fleutot, M.-D. Braida, T. Le Mercier, M.S. Islam, C. Masquelier, A review of structural properties and synthesis methods of solid electrolyte materials in the Li_2S−P_2S_5 binary system, J. Power Sources 407 (2018) 31-43.

[6] F. Mizuno, A. Hayashi, K. Tadanaga, M. Tatsumisago, New lithium-ion conducting crystal obtained by crystallization of the Li_2S–P_2S_5 glasses, Electrochem. Solid-State Lett. 8(11) (2005) A603-A606.

[7] Y. Seino, T. Ota, K. Takada, A. Hayashi, M. Tatsumisago, A sulphide lithium super ion conductor is superior to liquid ion conductors for use in rechargeable batteries, Energ Environ Sci 7(2) (2014) 627-631.

[8] N. Kamaya, K. Homma, Y. Yamakawa, M. Hirayama, R. Kanno, M. Yonemura, T. Kamiyama, Y. Kato, S. Hama, K. Kawamoto, A. Mitsui, A lithium superionic conductor, Nat. Mater. 10(9) (2011) 682-686.

[9] Y. Kato, S. Hori, T. Saito, K. Suzuki, M. Hirayama, A. Mitsui, M. Yonemura, H. Iba, R. Kanno, High-power all-solid-state batteries using sulfide superionic conductors, Nat. Energy 1 (2016) 7.

[10] Z.C. Liu, W.J. Fu, E.A. Payzant, X. Yu, Z.L. Wu, N.J. Dudney, J. Kiggans, K.L. Hong, A.J. Rondinone, C.D. Liang, Anomalous High Ionic Conductivity of Nanoporous β-Li_3PS_4, J. Am. Chem. Soc. 135(3) (2013) 975-978.

[11] K. Homma, M. Yonemura, T. Kobayashi, M. Nagao, M. Hirayama, R. Kanno, Crystal structure and phase transitions of the lithium ionic conductor Li_3PS_4, Solid State Ionics 182(1) (2011) 53-58.

[12] M. Tachez, J.-P. Malugani, R. Mercier, G. Robert, Ionic conductivity of and phase transition in lithium thiophosphate Li_3PS_4, Solid State Ionics 14(3) (1984) 181-185.

[13] N.H.H. Phuc, M. Totani, K. Morikawa, H. Muto, A. Matsuda, Preparation of Li_3PS_4 solid electrolyte using ethyl acetate as synthetic medium, Solid State Ionics 288 (2016) 240-243.

[14] H. Wang, Z.D. Hood, Y.N. Xia, C.D. Liang, Fabrication of ultrathin solid electrolyte membranes of β-Li_3PS_4 nanoflakes by evaporation-induced self-assembly for all-solid-state batteries, J. Mater. Chem. A 4(21) (2016) 8091-8096.

[15] N.H.H. Phuc, K. Morikawa, M. Totani, H. Muto, A. Matsuda, Chemical synthesis of Li_3PS_4 precursor suspension by liquid-phase shaking, Solid State Ionics 285 (2016) 2-5.

[16] S. Teragawa, K. Aso, K. Tadanaga, A. Hayashi, M. Tatsumisago, Liquid-phase synthesis of a Li_3PS_4 solid electrolyte using N-methylformamide for all-solid-state lithium batteries, J. Mater. Chem. A 2(14) (2014) 5095-5099.

[17] N.H.H. Phuc, K. Morikawa, T. Mitsuhiro, H. Muto, A. Matsuda, Synthesis of plate-like Li_3PS_4 solid electrolyte via liquid-phase shaking for all-solid-state lithium batteries, Ionics 23(8) (2017) 2061-2067.

[18] A. MATSUDA, H. MUTO, N.H. PHUC, Preparation of Li_3PS_4 solid electrolyte by liquid-phase shaking using organic solvents with carbonyl group as complex forming medium, Journal of the Japan Society of Powder and Powder Metallurgy 63(11) (2016) 976-980.

[19] S. Ito, M. Nakakita, Y. Aihara, T. Uehara, N. Machida, A synthesis of crystalline $Li_7P_3S_{11}$ solid electrolyte from 1,2-dimethoxyethane solvent, J. Power Sources 271 (2014) 342-345.

[20] R.C. Xu, X.H. Xia, Z.J. Yao, X.L. Wang, C.D. Gu, J.P. Tu, Preparation of $Li_7P_3S_{11}$ glass-ceramic electrolyte by dissolution-evaporation method for all-solid-state lithium ion batteries, Electrochim. Acta 219 (2016) 235-240.

[21] X.Y. Yao, D. Liu, C.S. Wang, P. Long, G. Peng, Y.S. Hu, H. Li, L.Q. Chen, X.X. Xu, High-Energy All-Solid-State Lithium Batteries with Ultralong Cycle Life, Nano Lett. 16(11) (2016) 7148-7154.

[22] S. Chida, A. Miura, N.C. Rosero-Navarro, M. Higuchi, N.H. Phuc, H. Muto, A. Matsuda, K. Tadanaga, Liquid-phase synthesis of Li_6PS_5Br using ultrasonication and application to cathode composite electrodes in all-solid-state batteries, Ceram. Int. 44(1) (2018) 742-746.

[23] K.S. Suslick, The chemical effects of ultrasound, Sci. Am. 260(2) (1989) 80-86.

[24] C. Chen, X. Huang, D. Lu, Y. Huang, B. Han, Q. Zhou, F. Li, T. Cui, High pressure Raman spectroscopy investigation on acetonitrile and acetonitrile-water mixture, RSC Adv. 5(102) (2015) 84216-84222.

[25] J.C. Deàk, L.K. Iwaki, D.D. Dlott, Vibrational Energy Redistribution in Polyatomic Liquids: Ultrafast IR−Raman Spectroscopy of Acetonitrile, J. Phys. Chem. A 102(42) (1998) 8193-8201.

[26] F. Mizuno, A. Hayashi, K. Tadanaga, M. Tatsumisago, New, Highly Ion-Conductive Crystals Precipitated from Li_2S–P_2S_5 Glasses, Adv. Mater. 17(7) (2005) 918-921.

[27] H. Yamane, M. Shibata, Y. Shimane, T. Junke, Y. Seino, S. Adams, K. Minami, A. Hayashi, M. Tatsumisago, Crystal structure of a superionic conductor, $Li_7P_3S_{11}$, Solid State Ionics 178(15-18) (2007) 1163-1167.

[28] K. Ohara, A. Mitsui, M. Mori, Y. Onodera, S. Shiotani, Y. Koyama, Y. Orikasa, M. Murakami, K. Shimoda, K. Mori, Structural and electronic features of binary Li_2S-P_2S_5 glasses, Sci Rep 6 (2016) 1-9.

[29] A. Hayashi, K. Minami, M. Tatsumisago, Development of sulfide glass-ceramic electrolytes for all-solid-state lithium rechargeable batteries, J. Solid State Electrochem. 14(10) (2010) 1761-1767.

[30] Y. Seino, M. Nakagawa, M. Senga, H. Higuchi, K. Takada, T. Sasaki, Analysis of the structure and degree of crystallisation of 70Li(2)S-30P(2)S(5) glass ceramic, Journal of Materials Chemistry A 3(6) (2015) 2756-2761.

[31] A. Sakuda, T. Takeuchi, H. Kobayashi, Electrode morphology in all-solid-state lithium secondary batteries consisting of $LiNi_{1/3}Co_{1/3}Mn_{1/3}O_2$ and Li_2S-P_2S_5 solid electrolytes, Solid State Ionics 285 (2016) 112-117.

[32] F. Mizuno, A. Hayashi, K. Tadanaga, M. Tatsumisago, High lithium ion conducting glass-ceramics in the system Li_2S-P_2S_5, Solid State Ionics 177(26-32) (2006) 2721-2725.

[33] Y. Wang, D. Lu, M. Bowden, P.Z. El Khoury, K.S. Han, Z.D. Deng, J. Xiao, J.-G. Zhang, J. Liu, Mechanism of formation of $Li_7P_3S_{11}$ solid electrolytes through liquid phase synthesis, Chem. Mater. 30(3) (2018) 990-997.

[34] C. Dietrich, D.A. Weber, S.J. Sedlmaier, S. Indris, S.P. Culver, D. Walter, J. Janek, W.G. Zeier, Lithium ion conductivity in Li_2S–P_2S_5 glasses–building units and local structure evolution during the crystallization of superionic conductors Li_3PS_4, $Li_7P_3S_{11}$ and $Li_4P_2S_7$, J. Mater. Chem. A 5(34) (2017) 18111-18119.

[35] T. Chivers, P.J. Elder, Ubiquitous trisulfur radical anion: fundamentals and applications in materials science, electrochemistry, analytical chemistry and geochemistry, Chem. Soc. Rev. 42(14) (2013) 5996-6005.

[36] M.E. Fleet, X. Liu, X-ray absorption spectroscopy of ultramarine pigments: a new analytical method for the polysulfide radical anion S^{3-} chromophore, Spectrochimica Acta Part B: Atomic Spectroscopy 65(1) (2010) 75-79.

[37] M. Cuisinier, C. Hart, M. Balasubramanian, A. Garsuch, L.F. Nazar, Radical or not radical: revisiting lithium–sulfur electrochemistry in nonaqueous electrolytes, Adv. Energy Mater 5(16) (2015) 1401801.

[38] G. Bieker, J. Wellmann, M. Kolek, K. Jalkanen, M. Winter, P. Bieker, Influence of cations in lithium and magnesium polysulphide solutions: dependence of the solvent chemistry, Phys. Chem. Chem. Phys 19(18) (2017) 11152-11162.

[39] R. Matsuda, E. Hirahara, N.H.H. Phuc, H. Muto, H. Tsukasaki, S. Mori, A. Matsuda, Preparation of $LiNi_{1/3}Mn_{1/3}Co_{1/3}O_2/Li_3PS_4$ cathode composite particles using a new liquid-phase process and application to all-solid-state lithium batteries, J. Ceram. Soc. Jpn. 126(10) (2018) 826-831.

[40] A. Matsuda, R. Matsuda, H. Muto, N.H. Phuc, In-Situ formation of Li_3PS_4 from liquid phase on Li metal as key material for Li dendrite suppression: a short review, Materials Today: Proceedings 16 (2019) 36-41.

[41] C. Dietrich, D.A. Weber, S. Culver, A. Senyshyn, S.J. Sedlmaier, S. Indris, J.r. Janek, W.G. Zeier, Synthesis, structural characterization, and lithium ion conductivity of the lithium thiophosphate $Li_2P_2S_6$, Inorg. Chem. 56(11) (2017) 6681-6687.

[42] H. Eckert, Z. Zhang, J.H. Kennedy, Structural transformation of non-oxide chalcogenide glasses. The short-range order of lithium sulfide (Li_2S)-phosphorus pentasulfide (P_2S_5) glasses studied by quantitative phosphorus-31, lithium-6, and lithium-7 high-resolution solid-state NMR, Chem. Mater. 2(3) (1990) 273-279.

[43] H. Eckert, J.H. Kennedy, A. Pradel, M. Ribes, Structural transformation of thiosilicate glasses: 29Si MAS-NMR evidence for edge-sharing in the system Li_2S-SiS_2, J. Non-Cryst. Solids 113(2-3) (1989) 287-293.

[44] T. Ozturk, E. Ertas, O. Mert, A berzelius reagent, phosphorus decasulfide (P_4S_{10}), in organic syntheses, Chem. Rev. 110(6) (2010) 3419-3478.

[45] S. Schönberger, C. Jagdhuber, L. Ascherl, C. Evangelisti, T.M. Klapötke, K. Karaghiosoff, New Acyclic Neutral Phosphorus Sulfides and Sulfide Oxides, Z. Anorg. Allg. Chem. 640(1) (2014) 68-75.

[46] S. Ito, M. Nakakita, Y. Aihara, T. Uehara, N. Machida, A synthesis of crystalline $Li_7P_3S_{11}$ solid electrolyte from 1, 2-dimethoxyethane solvent, J. Power Sources 271 (2014) 342-345.

[47] R. Koerver, F. Walther, I. Aygün, J. Sann, C. Dietrich, W.G. Zeier, J. Janek, Redox-active cathode interphases in solid-state batteries, J. Mater. Chem. A 5(43) (2017) 22750-22760.

PART II

Application of $Li_7P_3S_{11}$ solid electrolyte as ionic conductive additive in the composite cathode of all-solid-state batteries

All-solid-state lithium batteries using inorganic solid electrolytes instead of liquid electrolytes are expected to meet the required energy density and safety needs [1]. Sulfide-based solid electrolytes exhibit high ionic conductivity comparable to liquid electrolytes, and have good deformability due to their low Young's modulus [2]. However, development of a favorable electrode-electrolyte interface in bulk-type all-solid-state batteries is still a challenge [3]. Bulk-type all-solid-state batteries use composite electrodes with a powder mixture of active materials and additives to improve both the electronic and lithium ion conduction [4]. Addition of carbon materials, such as VGCF (Vapor-grown carbon fiber), in a content of around 2 wt.% is enough to achieve sufficient electronic conduction in the composite cathode [5]. However, a rather high content of solid electrolyte (60 wt%) is necessary to provide a good enough lithium ion conduction path [4]. A large interfacial contact area between active material and electrolyte particles and efficient ion-conductive pathways are necessary to obtain a good electrochemical performance in the all-solid-state battery [3, 6]. Solid electrolyte coating on active materials by using Pulser Laser Deposition (PLD) has been proven to be effective to obtaining high capacity and good electrochemical performance in the all-solid-state-cells, due to the formation of intimate electrode-electrolyte contacts [7]. However, a scale-up of the PLD technique for commercial application may not be practical. A new approach is the use of small-sized solid electrolyte particles. It has been reported that dense and homogeneous electrode layers with an effective lithium-ion conduction pathway and a large electrode electrolyte interfacial

contact area can be formed by the use of smaller-sized solid electrolyte particles [8]. Sulfide solid electrolytes that are typically prepared by mechanical milling process, are subsequently pulverized by using smaller diameter balls [8]. However, synthesis and pulverization, carried out by the mechanical milling process requires high energy and a long time.

As described previously, a solid electrolyte containing the $Li_7P_3S_{11}$ crystal phase, with high ionic conductivity ($1x10^{-3}$ Scm^{-1} at 22 °C) and small particle size, was successfully synthesized by an efficient procedure involving a liquid-phase process under ultrasonication and low heat treatment at 220 °C. The interaction between solvent and particles during the ultrasonication and the solvent removal led to obtaining the small particle size of around 500 nm. In contrast, sulfide solid electrolytes prepared by mechanical milling have particle sizes greater than 10 µm. A solid electrolyte with high ionic conductivity and small particle size is expected to be a suitable electrolyte to obtain a good ionic conduction path and large electrode electrolyte interfacial contact area in the composite cathode of all-solid-state batteries.

In this section, the electrochemical performance of an all-solid-state battery using NCM ($LiNbO_3$-coated $LiNi_{1/3}Co_{1/3}Mn_{1/3}O_2$) as a high voltage cathode material [9], VGCF as an electronic conductive additive, favorable to form continuous electron conducting path within the electrode [4] and a solid electrolyte containing the $Li_7P_3S_{11}$ crystal phase, prepared by liquid-phase under ultrasonic irradiation, as the ionic conductor in the composite cathode, was investigated and compared it to that of the all-solid-state battery using a solid electrolyte containing the $Li_7P_3S_{11}$ crystal phase but prepared by mechanical milling.

Preparation of $Li_7P_3S_{11}$ solid electrolyte by liquid-phase

$Li_7P_3S_{11}$ was synthesized by liquid-phase, following the synthesis procedure described in the first section of the previous part. Li_2S (Mitsuwa Chemical, 99.9%) and P_2S_5 (Aldrich, 99%), in stoichiometry composition of 74:26 mol%, were mixed in anhydrous acetonitrile (Wako Pure Chemical Industries), with a mass concentration of 50 g/l. The mixture was ultrasonicated under 28 kHz using an ultrasonic bath (Shimadzu SUS-103) for 30 minutes. The ultrasonication process formed a white suspension. The suspension was dried at 180 °C for three hours under vacuum to remove the solvent and obtain solid powders. The solid electrolytes powders were manually ground, using an agate mortar. Subsequently, the powders were heat-treated at a temperature of 220 °C.

Preparation of $Li_7P_3S_{11}$ solid electrolyte by mechanical milling

$Li_7P_3S_{11}$ was synthesized by mechanical milling, following a report by Tatsumisago et al. [2]. Mixture of Li_2S (Mitsuwa Chemical, 99.9%) and P_2S_5

(Aldrich, 99%) as starting materials was put into a zirconia pot (volume = 45 mL) with 500 zirconia balls (4 mm diameter). The mixture was ball-milled at 510 rpm for 10 h using a high-energy planetary ball mill apparatus. Subsequently, the resulting powder was heat-treated at 220 °C for 1 h, corresponding to the same heating temperature for the solid electrolyte prepared by liquid-phase, to achieve similar ionic conductivity.

Preparation of $80Li_2S$-$20P_2S_5$ solid electrolyte by mechanical milling

The $80Li_2S \cdot 20P_2S_5$ (mol%) solid electrolyte was prepared by mechanical milling. A mixture of Li_2S and P_2S_5 was put into a zirconia pot (volume = 45 mL) with 500 zirconia balls (4 mm diameter) and was ball-milled at 510 rpm for 10 h.

Fabrication of all-solid-state cells

Bulk-type all-solid-state cells were constructed as follows. $LiNbO_3$-coated $LiNi_{1/3}Co_{1/3}Mn_{1/3}O_2$ (NCM) [8, 10], $Li_7P_3S_{11}$ solid electrolyte and Vapor Grown Carbon Fiber (VGCF, Showa Denko), with a weight ratio of 79:19:2 were mixed to prepare the composite cathode. $80Li_2S \cdot 20P_2S_5$ (mol%) glass and In metal (99.99% 0.1 mm thickness) were used as separator layer and anode,

respectively. Bilayer pellets (φ = 10 mm) consisting of the composite cathode (10 mg) and $80Li_2S{\cdot}20P_2S_5$ solid electrolyte (80 mg) were obtained by pressing under 360 MPa at room temperature; indium foil (40 mg) was then attached to the bilayer pellets by pressing under 240 MPa. The three-layered pellets were sandwiched between two stainless-steel rods as current collectors to fabricate two-electrode cells. All of the processes were performed in an Ar-filled glove box.

Characterization

The crystal phase and chemical composition of the solid electrolytes were studied by using X-ray diffraction (XRD) and Raman spectroscopy. XRD measurements were performed using CuKα radiation with an X-ray diffractometer (Miniflex 600, Rigaku). Diffraction data were collected at 0.01° steps from 10° to 40° in 2θ.

Raman spectroscopy was performed using a Raman spectrometer (HORIBA XploRA PLUS Scientific). Raman spectra were recorded between 500 and 300 cm^{-1}.

The morphology of the sulfide solid electrolyte particles and the prepare composite cathodes were observed by scanning electron microscopy (SEM) performed on a JIB-4600F Multibeam SEM-FIB Scanning Electron Microscope, equipped with an energy-dispersive X-ray spectroscopy (EDX) system.

Electrochemical impedance spectroscopy measurements of the all-solid-state cells were performed using an impedance analyzer (SI 1260, Solartron) coupled with a potentiostat/galvanostat device (SI 1287, Solartron), in the frequency range from 0.1 Hz to 1 MHz at the amplitude of 80 mV.

Charge-discharge performance of the cells was evaluated under a constant current (CC) mode at 25 °C, under Ar atmosphere, using a charge-discharge measuring device (580 battery type system, Scribner Associates).

1. $Li_7P_3S_{11}$ solid electrolyte prepared by mechanical milling and liquid-phase

The structure and properties of the sulfide solid electrolytes prepared by the liquid-phase and mechanical milling processes were studied by using X-ray diffraction, Raman spectroscopy, scanning electron microscopy and electrochemical impedance spectroscopy.

Crystal phase and local structure

Figure 2.1a shows the XRD patterns of the synthesized sulfide solid electrolytes, prepared by liquid-phase and mechanical milling. The main peaks corresponding to the $Li_7P_3S_{11}$ phase were observed in both samples. The peak at $2\theta = 27°$ in the sample prepared by liquid-phase could be assigned to the Li_2S phase.

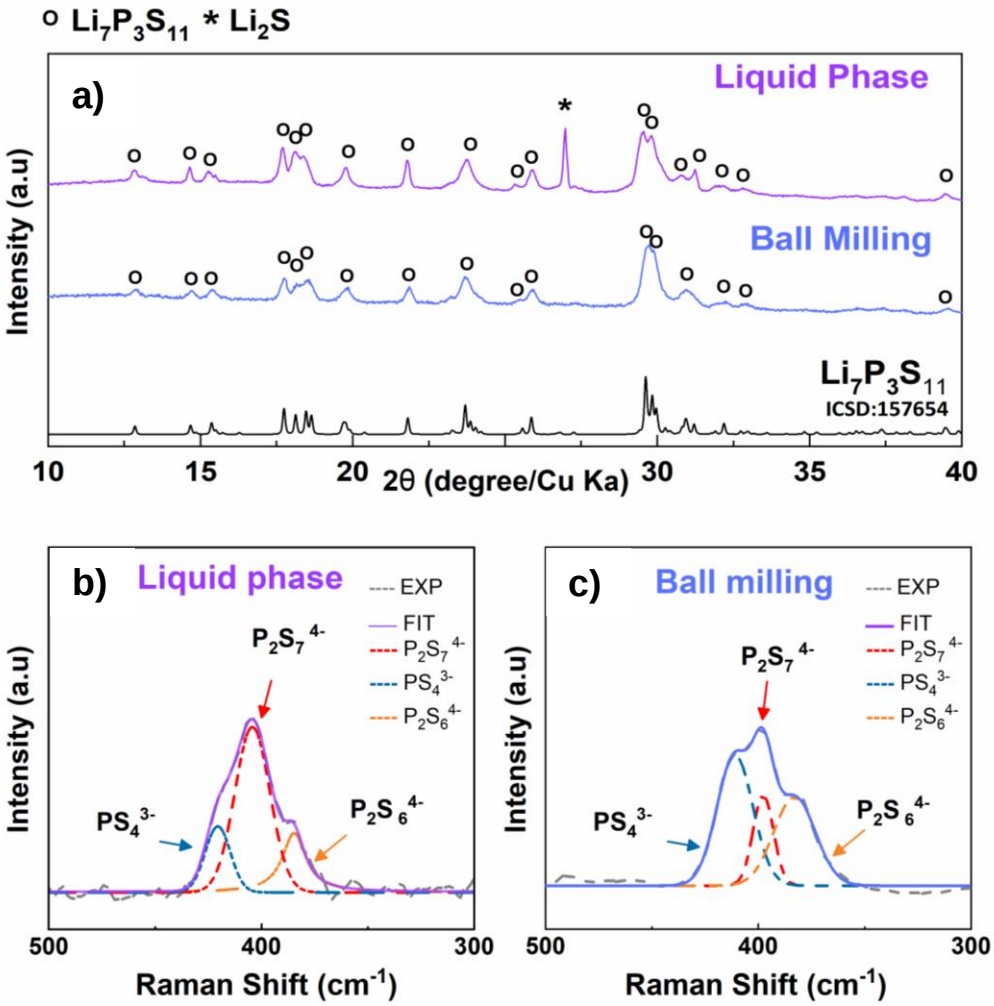

Figure 2.1 a) XRD patterns of the sulfide solid electrolytes prepared by liquid-phase and mechanical milling. **b)** and **c)** Spectral deconvolution of Raman spectra of the sulfide solid electrolytes prepared by the liquid-phase and mechanical milling processes, respectively. Spectra deconvolution was performed by using a Gaussian-Lorentzian function.

Figures 2.1b and 2.1c show the deconvolution of the Raman spectra of the sulfide solid electrolytes prepared by the liquid-phase and mechanical milling processes, respectively. Deconvolution of Raman spectra was performed by using a Gaussian–Lorentzian function. Both Raman spectra displays a wide band centered around 401 cm^{-1}. Deconvolutions shows that the wide bands were composed by three bands centered around 420 cm^{-1}, 401 cm^{-1} and 385 cm^{-1} attributed to PS_4^{3-} (orthothiophosphate), $P_2S_7^{4-}$ (pyro-thiophosphate) and $P_2S_6^{4-}$ (hypo-thiodiphosphate) units, respectively.

Morphology

Figure 2.2a shows the morphology of the sulfide solid electrolyte prepared by liquid-phase. Irregular particles with particle size around 500 nm were observed. As discussed above, the particle size and morphology can be attributed to the interaction between solvent and particles during ultrasonication and solvent removal. The particle disaggregation produced during the ultrasonication process and the surfactant function that acetonitrile plays during the solvent removal may have led to obtaining the small individual particles. Figure 2.2b shows the morphology of the sulfide solid electrolyte prepared by mechanical milling. A particle size larger than 10 µm was observed.

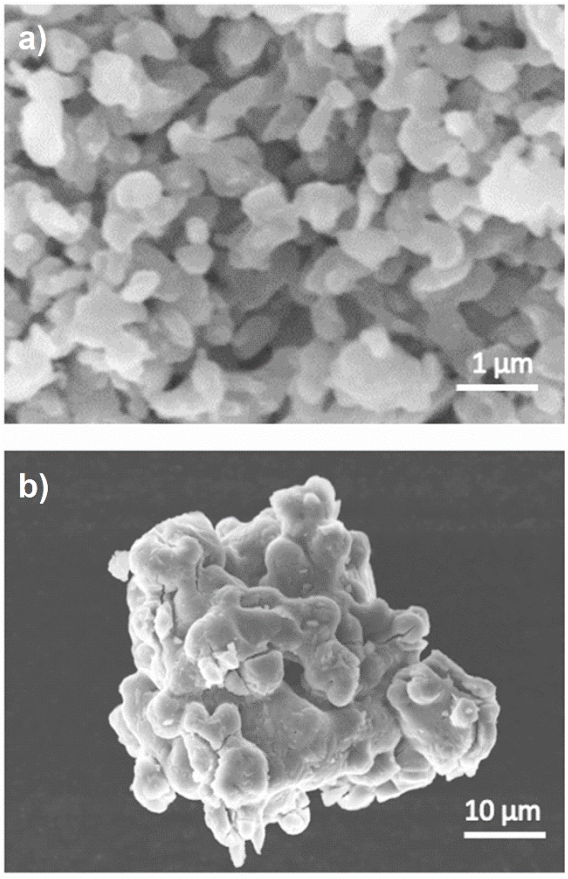

Figure. 2.2.SEM micrographs of $Li_7P_3S_{11}$ solid electrolyte prepared by the **a)** liquid-phase and **b)** mechanical milling processes.

Impedance analysis

Figure 2.3 shows the impedance spectra of the pelletized samples. Both samples exhibited only a capacitive tail at high frequencies, which is attributed to the contribution of the interface between the solid electrolyte and the blocking stainless steel electrodes. Each resistance was estimated by the value of *Z*' at the intercept with the real axis obtained by linear fitting. The total ionic conductivity at room temperature of $Li_7P_3S_{11}$ solid electrolyte obtained by liquid-phase and mechanical milling, attained 1×10^{-3} Scm^{-1} and 1.9×10^{-3} Scm^{-1}, respectively.

Discussion and summary

The evaluation of the prepared solid electrolytes by X-ray diffraction exposed the formation of $Li_7P_3S_{11}$ as the main crystal phase in both samples. Raman spectroscopy indicated that structural units of PS_4^{3-}, $P_2S_7^{4-}$ and $P_2S_6^{4-}$ are contained in the structure of the solid electrolytes prepared by both processes. Although a similar wide Raman band was observed in both samples, the deconvolution of the Raman bands elucidates a different distribution of the $P_xS_y^{z-}$ units. The major fraction corresponds to $P_2S_7^{4-}$ units when the solid electrolyte was prepared by liquid-phase and PS_4^{3-} units when the solid

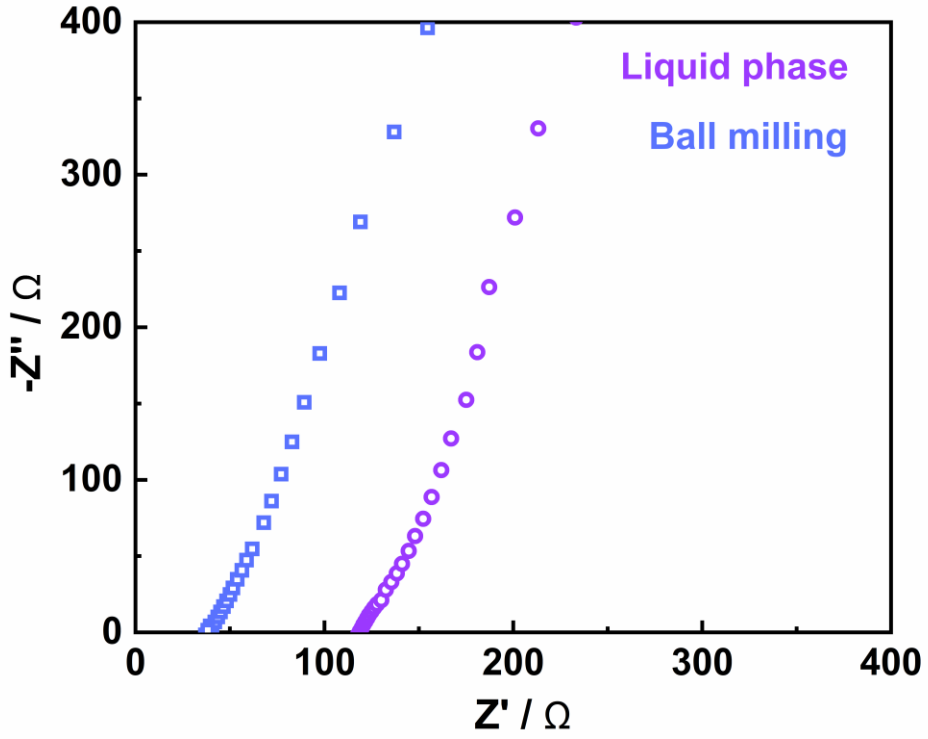

Figure. 2.3. Impedance spectra of pelletized $Li_7P_3S_{11}$ solid electrolytes prepared by liquid-phase (purple circles) and mechanical milling (blue squares).

electrolyte was prepared by mechanical milling. Differences in the local structure can be due to the different reaction and crystallization mechanisms that take place by the liquid-phase and mechanical milling processes.

Evaluation of the morphology by SEM shows that the particle size obtained by the liquid-phase process is more than 10 times smaller than that of the particle size obtained by the mechanical milling process. Even though there is a significant difference in particle size between both solid electrolytes, the ionic conductivity evaluated by EIS showed that both exhibited a comparable ionic conductivity over 10^{-3} S cm^{-1}. Sulfide solid electrolytes possess a Young's moduli of about 20 GPa [11], which is around 10 times lower than that of the oxides solid electrolytes (about 200 Gpa [12, 13]). The low Young's moduli enable a room temperature pressure sintering, and therefore, the resistance of pelletized sulfide solid electrolytes is not largely influenced by the particle size. The slightly higher ionic conductivity of the solid electrolyte prepared by mechanical milling may be due to the different distribution of $P_xS_y^{z-}$ units in the local structure.

Both solid electrolytes exhibited the $Li_7P_3S_{11}$ crystal phase attaining comparable high ionic conductivity over 10^{-3} S cm^{-1}, and a different morphology. High ionic conductivity and a favorable morphology is necessary to obtain an effective lithium-ion pathway in the composite cathode, and therefore a good electrochemical performance in the bulk-type all-solid-state batteries. Thus, the influence of both $Li_7P_3S_{11}$ solid electrolytes, prepared by liquid-phase and mechanical milling processes, as the ionic conductor in the composite cathode for bulk-type all-solid-state batteries was investigated.

2. Morphology of the electrode composites

Figure 2.4 shows SEM images and energy-dispersive X-ray spectroscopy (EDX) elemental mappings for oxygen (O), manganese (Mn), phosphorous (P) and sulfur (S) of cross-sections of the composite cathode layers prepared by a simple mixture of NCM as cathode material, VGCF as electronic conductive additive and $Li_7P_3S_{11}$ synthesized by mechanical milling and liquid-phase processes as ionic conductive additive. The EDX elemental mappings of O and Mn show the distribution of NCM and the EDX elemental mappings of P and S show the distribution of the solid electrolyte. SEM and EDX images of the composite cathode with $Li_7P_3S_{11}$ prepared by mechanical milling (Figure 2.4a), show large agglomerations of NCM particles, and large aggregates of solid electrolyte, greater than 20 µm. The poor distribution of the solid electrolyte in the composite cathode was expected due to its large particle size (Figure 2.2b). To obtain a good dispersion of solid electrolyte with large particle size is difficult due to the rather high active material content in the composite cathode. The SEM image of the composite cathode with $Li_7P_3S_{11}$ prepared by liquid-phase (Figure 2.4b), does not allow the identification of the solid electrolyte in the composite cathode. However, EDX analysis shows that the solid electrolyte was located between the NCM particles. A better distribution of the solid electrolyte through the composite cathode was observed, which is attributed to the small particle size of the solid electrolyte.

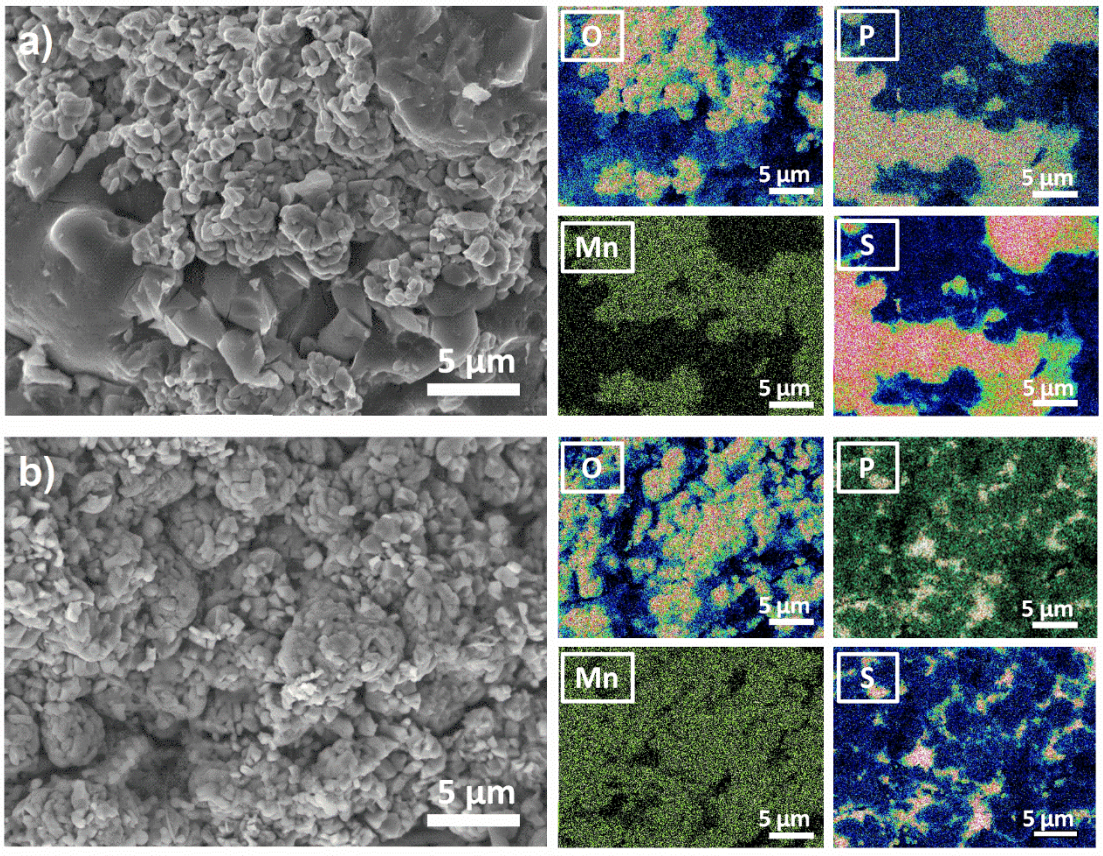

Figure 2.4. SEM images and EDX elemental mappings for O, P, Mn and S of cross-section of the positive composite electrode layer using NCM as active material and solid electrolyte containing the $Li_7P_3S_{11}$ crystal phase prepared by **a)** mechanical milling and **b)** liquid-phase processes as the ionic conductor.

3. Electrochemical characterization of the all-solid-state cells

Galvanostatic measurements

Figure 2.5 shows the first charge-discharge curves and cycle performance of all-solid-state cells with composite cathode fabricated with NCM, VGCF and $Li_7P_3S_{11}$ prepared by liquid-phase and mechanical milling processes. The measurements were conducted using a constant current (CC) mode at a current density of 0.13 mA cm^{-2} and cut-off voltages of 3.8 and 2 V. The all-solid-state cell constructed using $Li_7P_3S_{11}$ prepared by the mechanical milling process had an initial discharge capacity of 46 mAh g^{-1}. The inhomogeneous distribution of NCM and solid electrolyte in the composite cathode layer (Figure 2.4a) resulted in a poor interfacial contact area between active material and electrolyte particles, and therefore in limited lithium ion-conductive pathways, which led to a deficient use of the active material. In contrast, the all-solid-state cell constructed using $Li_7P_3S_{11}$ prepared by the liquid-phase process, had an initial discharge capacity of 154 mAh g^{-1}, more than three times higher than that of the all-solid-state cell using $Li_7P_3S_{11}$ obtained by the mechanical milling process. These results show that the better distribution of the solid electrolyte in the composite cathode, due to the small particle size of the $Li_7P_3S_{11}$ prepared by the liquid-phase, was effective in achieving more favorable lithium ion pathways to the NCM particles, and therefore achieving a larger discharge capacity.

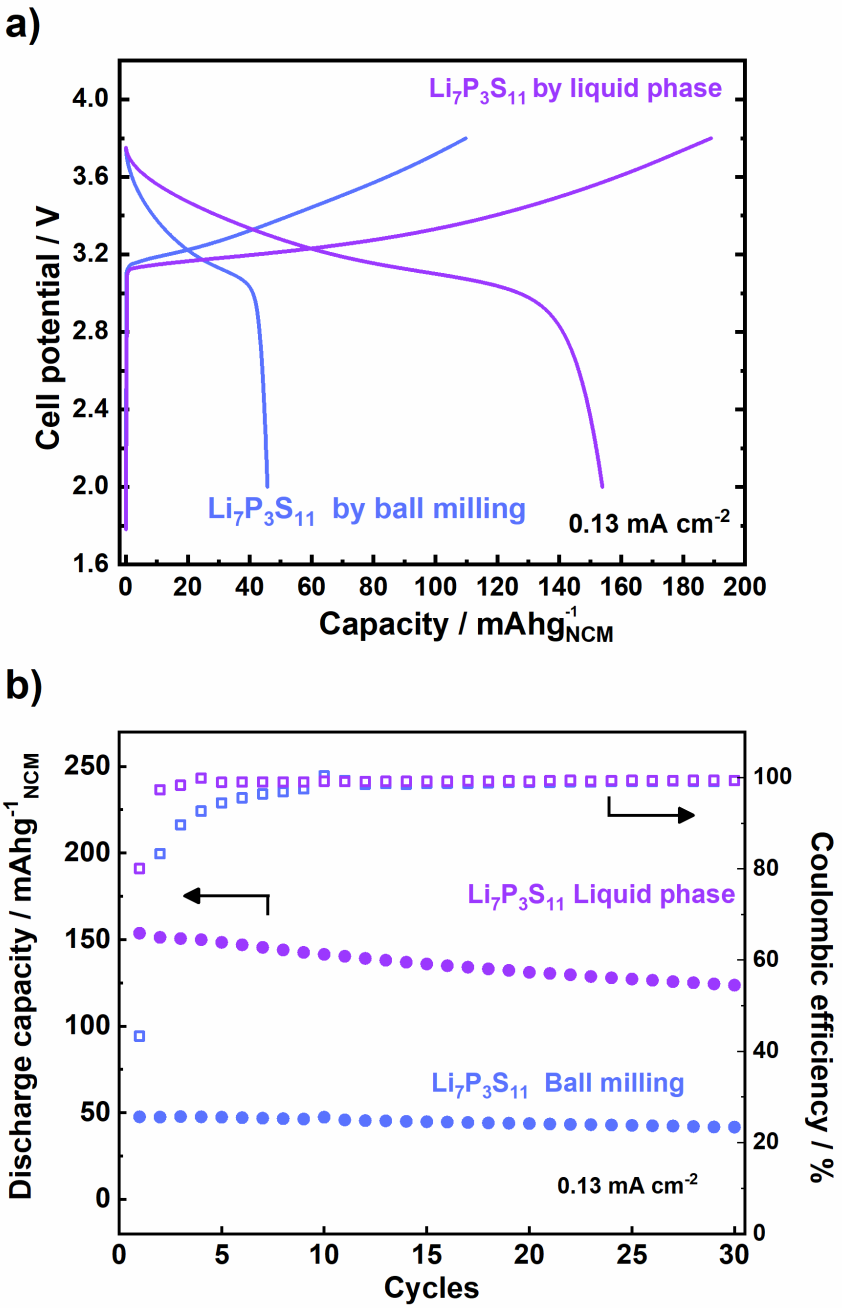

Figure 2.5. a) First charge-discharge curves and **b)** cycle performance of the all-solid-state cells using NCM as active material and $Li_7P_3S_{11}$ prepared by liquid-phase and mechanical milling processes as the ionic conductor in the composite cathode.

The all-solid-state cell with the composite cathode containing $Li_7P_3S_{11}$, prepared by liquid-phase, exhibited a capacity retention of 81% after 30 cycles, and a coulombic efficiency over 99% after the first 3 cycles. The all-solid-state cell with the composite cathode containing $Li_7P_3S_{11}$ prepared by mechanical milling, exhibited a capacity retention of 87% after 30 cycles, and a coulombic efficiency over 99% after the first 10 cycles.

Impedance analysis

Figure 2.6a and b shows the impedance profiles of the all-solid-state cells of Figure 2.5 before charging and after the 30^{th} cycle in the charged state. Before charging, both impedance profiles consist of an incomplete semicircle, due to the lower resistance, at high frequency (1 MHz) and a capacitive tail at low frequency (100KHz), corresponding to the total resistance (Bulk and grain boundary) of the $80Li_2S{\cdot}20P_2S_5$ solid electrolyte used as separator layer (ca. 120 Ω), and the electrode interfaces (composite cathode and indium anode), respectively. After 30 cycles, two additional semicircles are observed in the impedance profiles. The top frequencies of the semicircles are 1 kHz and 1 Hz. The resistance observed at the medium (1 kHz) and low frequency (1 Hz) regions have been attributed to the resistances in the positive electrode layer and the negative electrode layer, respectively [14]. Fitting results of the impedance profiles (solid line in Figure 2.6a and b) using the equivalent circuit of Figure 2.6c are shown in Table 2.1.

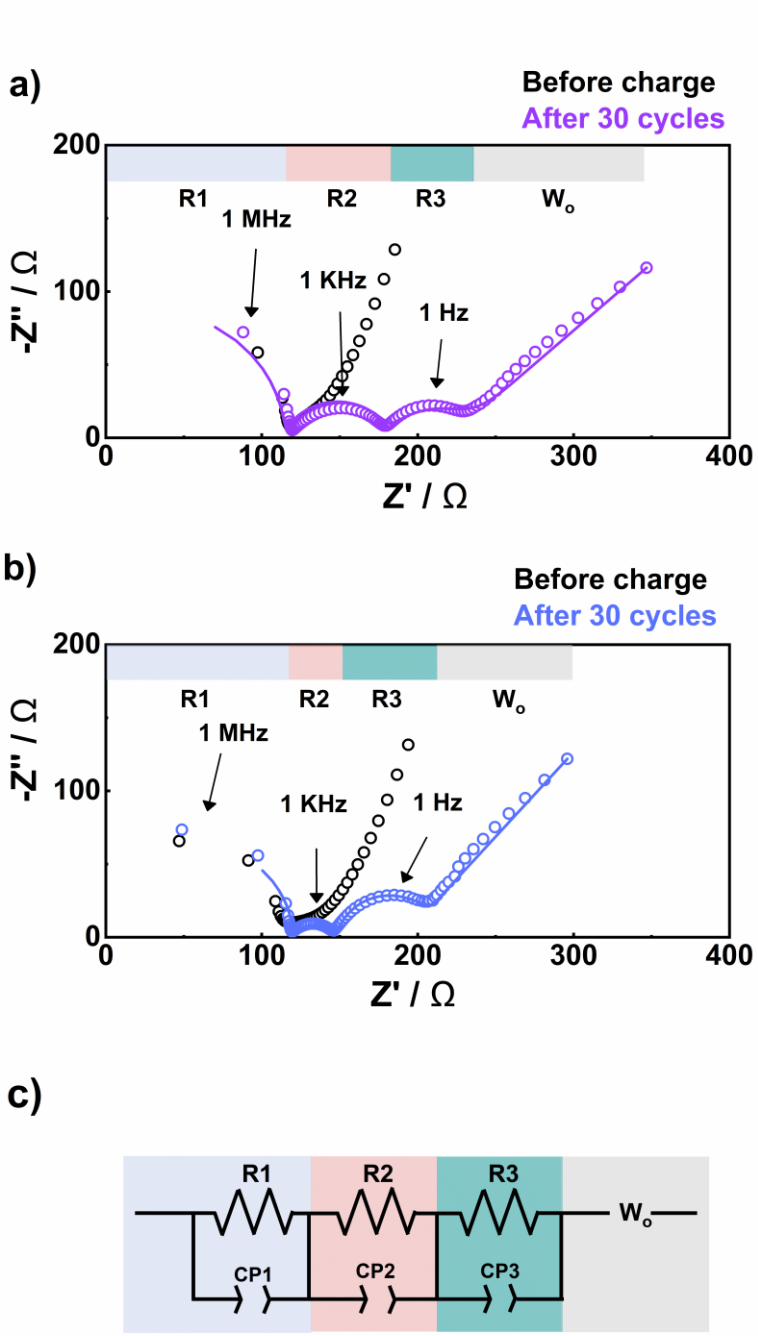

Figure 2.6 Nyquist plot of the impedance profiles of the all-solid-state cells using NCM as active material and $Li_7P_3S_{11}$ prepared by **a)** liquid-phase and **b)** mechanical milling processes as the ionic conductor in the composite cathode, before charge and after the 30th charge. Open circles represent the measured data, and solid lines indicated the fit of the data. **c)** Equivalent circuit for the impedance profiles fitting.

Table 2.1. Fitting Results of the EIS Spectra of the all-solid-state cells using NMC as active material and $Li_7P_3S_{11}$ prepared by the liquid-phase and mechanical milling processes as ionic conductive additive in the composite cathode

Cell	R1	R2	R3
NCM/ $Li_7P_3S_{11}$ (liquid-phase) before charge	119.6	-	-
NCM/ $Li_7P_3S_{11}$ (liquid-phase) after 30 cycles	119.6	67	46
NCM $Li_7P_3S_{11}$ (mechanical milling) before charge	119.6	-	-
NCM/ $Li_7P_3S_{11}$ (mechanical milling) after 30 cycles	119.7	25	48

The resistance at the high frequency region exhibited a similar value to that of before the battery cycling (ca. 120 Ω), in both cells. The high frequency resistance is essentially independent of the battery cycling since it corresponds to the lithium transport in the solid electrolyte used as separator layer. At the low frequency region (1Hz), no remarkable difference is observed between both cells (ca. 47 Ω). These results corroborate that both cells are equal at the separator and negative electrode layers, and that the different electrochemical behavior can be assigned to differences at the electrode-electrolyte interface at the positive electrode layer. The resistances at the medium frequency were determined to be 67 Ω and 25 Ω for the composite cathodes containing $Li_7P_3S_{11}$ prepared by liquid-phase and mechanical milling processes, respectively. The resistance in the positive electrode layer has been explained by two possible mechanisms: formation of a space-charge layer at the interfaces [15] and interfacial chemical reactions that involves elements mutual diffusion between the oxide cathode materials and sulfide electrolytes [14]. Oxide coatings on cathode materials has been found to suppress the interfacial resistance [16]. However, development of completely uniform coating layers without any gap is difficult [10]. Thus, formation of the high-resistance interfaces in the positive electrode can be expected. From these results, the capacity decay observed in both cells may be attributed to the formation of the high-resistance interfaces. The larger resistance corresponding to the positive electrode layer that was found in the all-solid-state cell with the composite cathode containing $Li_7P_3S_{11}$ prepared by liquid-phase, could be related to the possible presence of remaining organic complexes in the solid electrolyte due to the liquid-phase

synthesis [17], and the larger interfacial contact area between active material and electrolyte particles.

4 Electrochemical characterization under high charge-end voltage

The electrochemical behavior of the all-solid-state cell with composite cathode containing $Li_7P_3S_{11}$ prepared by liquid-phase was investigated under high-charge-end voltages.

Galvanostatic measurements

After the first 30 charge-discharge cycles (cut-off voltages of 3.8 and 2 V), the all-solid-state cell was charged and discharged with cut-off voltages of 3.9 and 2 V for 10 cycles and subsequently with cut-off voltages of 4 and 2 V for 10 cycles. All measurements were conducted using a constant current (CC) mode at a current density of 0.13 mA cm^{-2}. Figure 2.7a shows the 30^{th}, 40^{th} and 50^{th} discharge curves, corresponding to measurements performed with charge-end voltages of 3.8, 3.9 and 4 V, respectively. Figure 2.7b shows the corresponding cycle performance. The coulombic efficiency maintained at a value of around 99% for all cycles. According to the coulombic efficiency, a continuous capacity decay was observed.

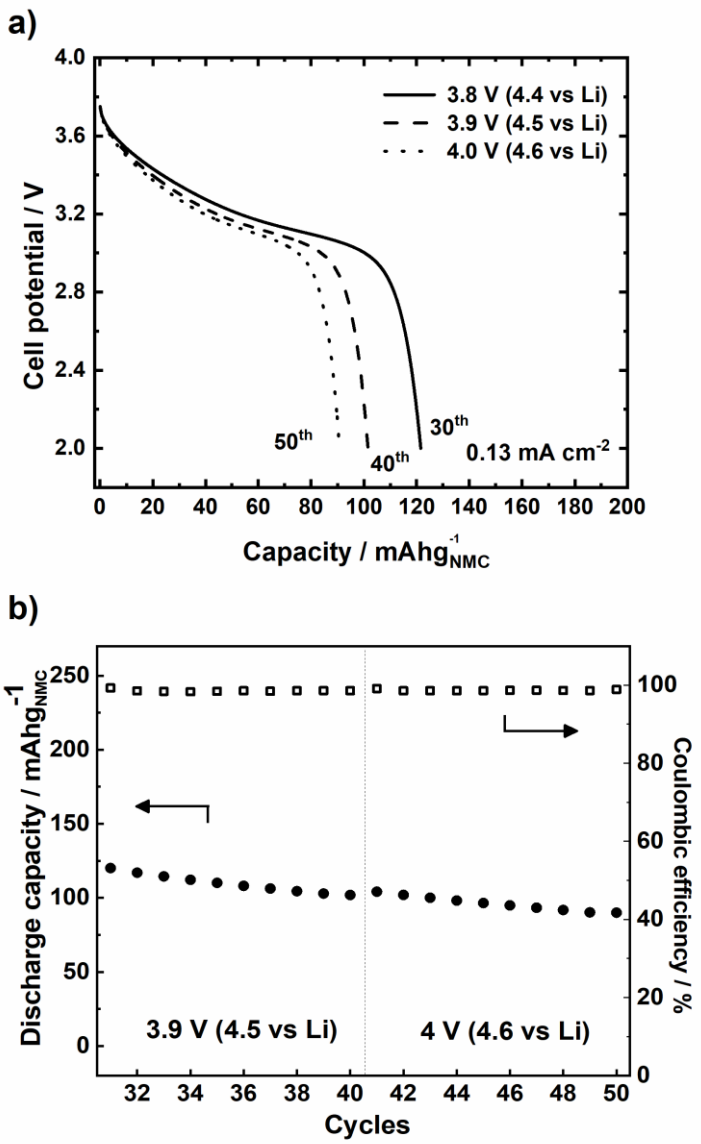

Figure 2.7. a) 30th, 40th and 50th discharge curves of the all-solid-state cell using NCM as active material and $Li_7P_3S_{11}$prepared by the liquid-phase process as the ionic conductor in the composite cathode, corresponding to measurements performed with charge-end voltages of 3.8, 3.9 and 4 V, respectively. **b)** Cycle performance corresponding to the charge-discharge measurements performed with charge-end voltages of 3.9 and 4 V.

Impedance analysis

Figure 2.8 shows the impedance profiles measured after the 40th (cut-off voltage of 3.9V) and 50th (cut-off voltage of 4V) charges of the all-solid-state cell of Figure 2.7. The impedance profiles are similar to that obtained after the 30th charge (Figure 2.6a). Two semicircles are observed, and the frequencies at the top of the semicircles are 1 kHz and 1 Hz. The resistances observed at the medium (1 kHz) and low frequency (1 Hz) regions correspond to the resistance in the positive and negative electrode layers, respectively, as discussed above. Fitting results of the impedance profiles (solid line in Figure 2.8) using the equivalent circuit of Figure 2.6c are shown in Table 2.2. A clear increase in the resistance at the medium frequency was observed after charge-discharge measurements with charge-end voltages of 3.9 V (4.5 V vs Li) and 4 V (4.6 V vs Li), attaining 145 Ω and 318 Ω, respectively. The higher interfacial resistance in the positive electrode layer could be explained by the possible degradation of the active material and sulfide electrolytes, due to the applied high charge-end voltages. It has been observed that NCM cathode material can undergo lattice volume changes upon charge, and that most pronounced changes occur at high charge-end voltages above 4.4 V [18, 19]. It has also been observed that sulfide solid electrolytes can undergo decomposition at the interfaces, above 4.5 V during charging process, which would result in the formation of isolating layers [20].

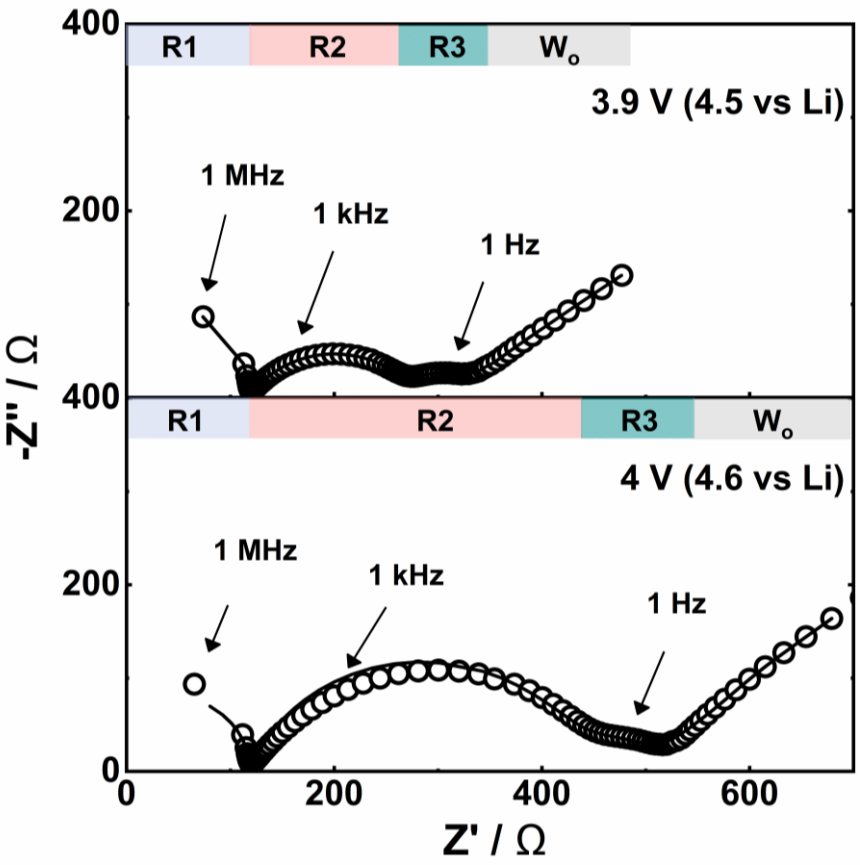

Figure 2.8. Nyquist plot of the impedance profiles of the all-solid-state cell using NCM as active material and $Li_7P_3S_{11}$ prepared by the liquid-phase process as the ionic conductor in the composite cathode, after the 40th and 50th charge. Open circles represent the measured data, and solid lines indicated the fit of the data.

Table 2.2 Fitting Results of the EIS Spectra of the all-solid-state cell using NMC as active material and $Li_7P_3S_{11}$ prepared by the liquid-phase process as ionic conductive additive in the composite cathode

Charge-end Voltage	R1	R2	R3
3.9 V	119.7	145	57
4 V	119.7	318	63

5. Study of the local structure stability of the solid electrolyte

To investigate the possible degradation of the $Li_7P_3S_{11}$ solid electrolyte, the local structure of the solid electrolyte was analyzed by using ex-situ Raman spectroscopy after the charge-discharge measurements with high charge-end voltages. Ex-situ Raman spectroscopy was obtained for the composite cathode layer after the 50th cycle corresponding to the last measurement with charge-end voltage of 4 V (4.6 V vs Li). Figure 2.9b shows the deconvolution of the measurements average (900 points), by using a Gaussian–Lorentzian function. Two main peaks centered at 405 cm^{-1} and 420 cm^{-1}, corresponding to $P_2S_7^{4-}$ and PS_4^{3-} units were observed. Although no peak corresponding to the $P_2S_6^{4-}$ units was adjusted by the deconvolution, a scarce presence of these units was observed in the experimental data. Figure 2.9a shows the deconvolution of the Raman spectra corresponding to the as-prepared composite cathode for comparison. Solid electrolytes containing the $Li_7P_3S_{11}$ crystal phase can go through changes in its structure under some input energy [21, 22]. For example, under heating at temperatures as high as 250 °C, structural changes proceeds to the formation of $P_2S_6^{4-}$ units which conduces to low ionic conductivity [22]. However, in the present study no additional formation of $P_2S_6^{4-}$ units in the structure of the $Li_7P_3S_{11}$ solid electrolyte, was found after charge-discharge measurements with high charge-end voltages. These results suggest that the $Li_7P_3S_{11}$ solid electrolyte did not suffer a significant structural change and that no degradation of the ionic conductivity can be expected after the charge-discharge processes, even at high charge-end voltages.

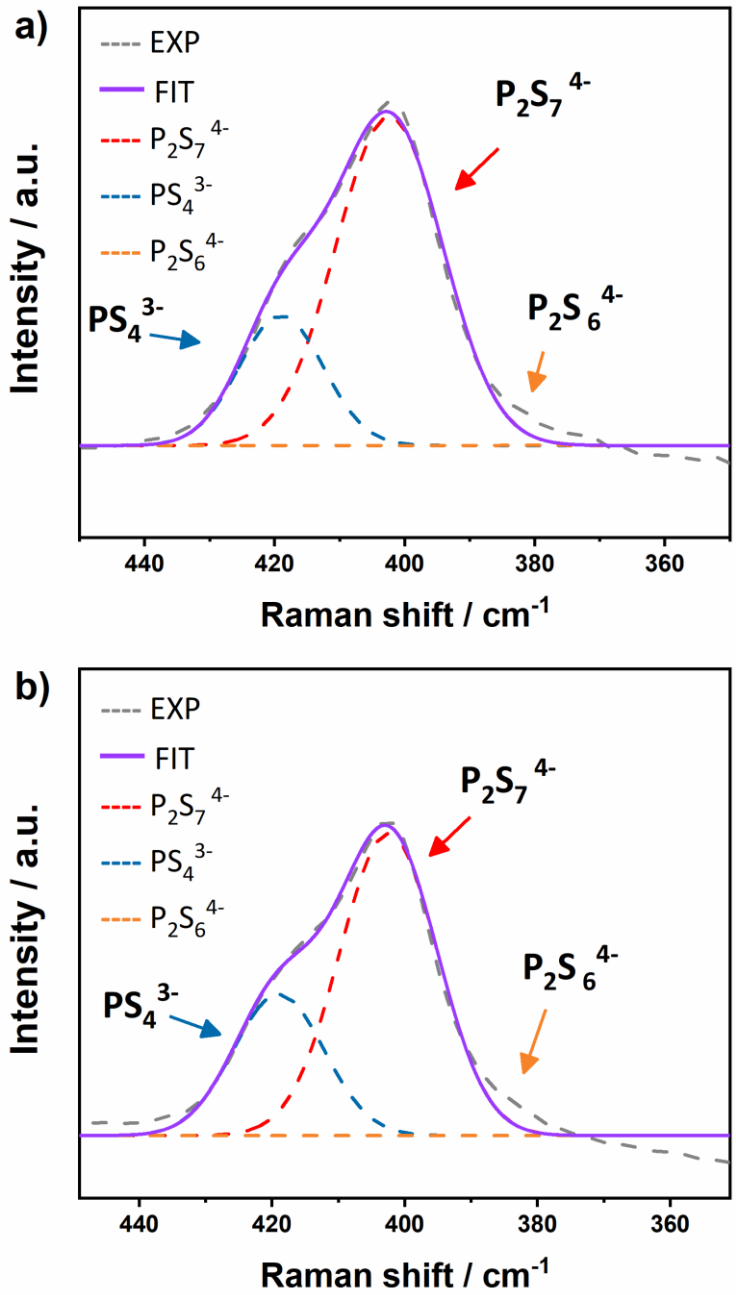

Figure 2.9. Spectral deconvolution of Raman spectra of **a)** the as-prepared composite cathode and **b)** the composite cathode layer after the 50th cycles (charge-end voltage of 4 V), by using a Gaussiane Lorentzian function.

Hence, the formation of high-resistance interfaces in the positive electrode layer may be attributed to volume changes of the NCM material due to the use of the high charge-end voltage.

Summary

$Li_7P_3S_{11}$ sulfide solid electrolyte was prepared by using liquid-phase and mechanical milling processes. Both solid electrolytes exhibited the formation of $Li_7P_3S_{11}$ as the main phase, and local structure composed by PS_4^{3-}, $P_2S_7^{4-}$ and $P_2S_6^{4-}$ units. A particle size around 500 nm and 10 µm was obtained by the liquid-phase and mechanical milling processes, respectively. Both solid electrolytes presented a comparable ionic conductivity over 10^{-3} Scm^{-1}.

The application of the prepared solid electrolytes as the ionic conductor in the composite cathode of all-solid-state batteries was investigated. It was found that the particle size of the solid electrolyte largely influences the morphology of the composite cathode electrode. A non-homogenous distribution of solid electrolyte and active material particles was found in the composite cathode by using the solid electrolyte prepared by the mechanical milling, due to the large particle size. In contrast, the small particle size of the solid electrolyte prepared by the liquid-phase enabled a better distribution of the solid electrolyte between the active material particles.

The all-solid-state cells using the NCM cathode material and the $Li_7P_3S_{11}$ sulfide solid electrolyte prepared by the liquid-phase and mechanical milling processes, exhibited a first discharge capacity of 154 mA h g^{-1} and 46 mA h g^{-1}, respectively. This suggests that the use of small-sized solid electrolytes is effective to obtain favorable lithium ion pathways in the composite cathode electrode, and therefore to achieve a better electrochemical performance in the all-solid-state battery.

The structure of the $Li_7P_3S_{11}$ solid electrolyte, prepared by liquid-phase, in the composite cathode after charge-discharge measurements was investigated by using ex-situ Raman spectroscopy. Although, $Li_7P_3S_{11}$ can undergo structural changes, which proceeds to the formation of $P_2S_6^{4-}$ units, with some energy input, formation of $P_2S_6^{4-}$ units was not found after charge-discharge measurements with high charge-end voltages. This indicates that the $Li_7P_3S_{11}$ solid electrolyte is stable against charge-discharge measurements.

References

[1] Y. Kato, S. Hori, T. Saito, K. Suzuki, M. Hirayama, A. Mitsui, M. Yonemura, H. Iba, R. Kanno, High-power all-solid-state batteries using sulfide superionic conductors, Nat. Energy 1 (2016) 7.

[2] A. Sakuda, A. Hayashi, M. Tatsumisago, Sulfide Solid Electrolyte with Favorable Mechanical Property for All-Solid-State Lithium Battery, Sci Rep 3 (2013) 1-5.

[3] A. Sakuda, A. Hayashi, M. Tatsumisago, Recent progress on interface formation in all-solid-state batteries, Current Opinion in Electrochemistry 6(1) (2017) 108-114.

[4] F. Mizuno, A. Hayashi, K. Tadanaga, M. Tatsumisago, Design of composite positive electrode in all-solid-state secondary batteries with Li_2S-P_2S_5 glass–ceramic electrolytes, J. Power Sources 146(1-2) (2005) 711-714.

[5] M. Tatsumisago, F. Mizuno, A. Hayashi, All-solid-state lithium secondary batteries using sulfide-based glass–ceramic electrolytes, J. Power Sources 159(1) (2006) 193-199.

[6] A. Hayashi, A. Sakuda, M. Tatsumisago, Development of sulfide solid electrolytes and interface formation processes for bulk-type all-solid-state Li and Na batteries, Frontiers in Energy Research 4 (2016) 25.

[7] Y. Ito, M. Otoyama, A. Hayashi, T. Ohtomo, M. Tatsumisago, Electrochemical and structural evaluation for bulk-type all-solid-state batteries using Li_4GeS_4-Li_3PS_4 electrolyte coating on $LiCoO_2$ particles, J. Power Sources 360 (2017) 328-335.

[8] A. Sakuda, T. Takeuchi, H. Kobayashi, Electrode morphology in all-solid-state lithium secondary batteries consisting of $LiNi_{1/3}Co_{1/3}Mn_{1/3}O_2$ and Li_2S-P_2S_5 solid electrolytes, Solid State Ionics 285 (2016) 112-117.

[9] H. Kitaura, A. Hayashi, K. Tadanaga, M. Tatsumisago, Electrochemical performance of all-solid-state lithium secondary batteries with Li–Ni–Co–Mn oxide positive electrodes, Electrochim. Acta 55(28) (2010) 8821-8828.

[10] N. Ohta, K. Takada, I. Sakaguchi, L.Q. Zhang, R.Z. Ma, K. Fukuda, M. Osada, T. Sasaki, $LiNbO_3$-coated $LiCoO_2$ as cathode material for all solid-state lithium secondary batteries, Electrochem. Commun. 9(7) (2007) 1486-1490.

[11] A. Sakuda, A. Hayashi, M. Tatsumisago, Sulfide Solid Electrolyte with Favorable Mechanical Property for All-Solid-State Lithium Battery, Sci Rep 3 (2013) 5.

[12] Y.H. Cho, J. Wolfenstine, E. Rangasamy, H. Kim, H. Choe, J. Sakamoto, Mechanical properties of the solid Li-ion conducting electrolyte: $Li_{0.33}La_{0.57}TiO_3$, J. Mater. Sci. 47(16) (2012) 5970-5977.

[13] G. Bucci, T. Swamy, Y.M. Chiang, W.C. Carter, Modeling of internal mechanical failure of all-solid-state batteries during electrochemical cycling, and implications for battery design, Journal of Materials Chemistry A 5(36) (2017) 19422-19430.

[14] A. Sakuda, A. Hayashi, M. Tatsumisago, Intefacial Observation between $LiCoO_2$ Electrode and Li_2S-P_2S_5 Solid Electrolytes of All-Solid-State Lithium Secondary Batteries Using Transmission Electron Microscopy, Chem. Mat. 22(3) (2010) 949-956.

[15] K. Takada, N. Ohta, Y. Tateyama, Recent Progress in Interfacial Nanoarchitectonics in Solid-State Batteries, Journal of Inorganic and Organometallic Polymers and Materials 25(2) (2015) 205-213.

[16] N. Ohta, K. Takada, L.Q. Zhang, R.Z. Ma, M. Osada, T. Sasaki, Enhancement of the high-rate capability of solid-state lithium batteries by nanoscale interfacial modification, Adv. Mater. 18(17) (2006) 2226-+.

[17] S. Chida, A. Miura, N.C. Rosero-Navarro, M. Higuchi, N.H.H. Phuc, H. Muto, A. Matsuda, K. Tadanaga, Liquid-phase synthesis of Li_6PS_5Br using ultrasonication and application to cathode composite electrodes in all-solid-state batteries, Ceramics International 44(1) (2018) 742-746.

[18] A.O. Kondrakov, A. Schmidt, J. Xu, H. Gesswein, R. Monig, P. Hartmann, H. Sommer, T. Brezesinski, J. Janek, Anisotropic Lattice Strain and Mechanical Degradation of High- and Low-Nickel NCM Cathode Materials for Li-Ion Batteries, J. Phys. Chem. C 121(6) (2017) 3286-3294.

[19] N. Yabuuchi, Y. Makimura, T. Ohzuku, Solid-state chemistry and electrochemistry of $LiCo_{1/3}Ni_{1/3}Mn_{1/3}O_2$ for advanced lithium-ion batteries III. Rechargeable capacity and cycleability, J. Electrochem. Soc. 154(4) (2007) A314-A321.

[20] G. Oh, M. Hirayama, O. Kwon, K. Suzuki, R. Kanno, Bulk-Type All Solid-State Batteries with 5 V Class $LiNi_{0.5}Mn_{1.5}O_4$ Cathode and $Li_{10}GeP_2S_{12}$ Solid Electrolyte, Chem. Mat. 28(8) (2016) 2634-2640.

[21] Y. Aoki, K. Ogawa, T. Nakagawa, Y. Hasegawa, Y. Sakiyama, T. Kojima, M. Tabuchi, Chemical and structural changes of $70Li_2S$-$30P_2S_5$ solid electrolyte during heat treatment, Solid State Ionics 310 (2017) 50-55.

[22] M. Calpa, N.C. Rosero-Navarro, A. Miura, K. Tadanaga, Preparation of sulfide solid electrolytes in the Li_2S-P_2S_5 system by a liquid phase process, Inorganic Chemistry Frontiers 5(2) (2018) 501-508.

General conclusions

This thesis focused on the liquid-phase synthesis of sulfide solid electrolytes in the Li_2S-P_2S_5 system for the application to all-solid-state batteries. Li_2S-P_2S_5 sulfide solid electrolytes were prepared by a liquid-phase process under ultrasonic irradiation and using acetonitrile as the medium for the reaction. The studies on the crystallization process and the special focus on the precursors and the initial reactions between them allowed the understanding of the main reaction mechanisms governing the liquid-phase synthesis. The advantages of the Li_2S-P_2S_5 sulfide solid electrolytes prepared by liquid-phase were demonstrated by their application to the all-solid-state battery.

The following results and considerations were obtained.

1. Li_2S-P_2S_5 sulfide solid electrolytes were prepared by a liquid-phase process under ultrasonic irradiation, using acetonitrile as the medium for the reaction. The use of ultrasonic irradiation was effective in promoting the reaction, and reduce the reaction time from days to minutes. Particularly, the Li_2S-P_2S_5 solid electrolyte with Li_2S content of 74 mol% exhibited the high ionic conductivity of 10^{-3} Scm^{-1} and a small particle size below 500 nm.

2. The crystallization process that took place in the liquid-phase synthesis was elucidated by examining the crystal and local structure, morphology and ionic

conductivity of the solid electrolyte after each step of the synthesis. It was found that the ultrasonic irradiation provides enough energy for the formation of PS_4^{3-} units after only 30 min. X-ray diffraction and Raman spectroscopy studies revealed the complex formation between PS_4^{3-} units and acetonitrile. The complex between PS_4^{3-} units and acetonitrile only dissociated at temperatures over 180 °C. The dissociation of the complex was accompanied by the formation of $P_2S_7^{4-}$ units resulting in the precipitation of the high ionic conductive $Li_7P_3S_{11}$ crystal phase.

3. Focus on the Li_2S and P_2S_5 precursors and their reaction in 50:50 mol% allowed the understanding of the initial chemical reactions that trigger the formation of the $P_xS_y^{z-}$ thiophosphate units in the liquid-phase process. As well, the possible reaction pathway for the formation of the high ionic conductive $Li_7P_3S_{11}$ crystal phase in $Li_2S–P_2S_5$ solid electrolytes synthesized by liquid-phase.

4. The liquid-phase derived solid electrolyte containing the $Li_7P_3S_{11}$ crystal phase and small particle size bellow 500 nm, was used as the ionic conductive additive in the composite cathode of all-solid-state batteries. The all-solid-state cell using the solid electrolyte prepared by liquid-phase exhibited better electrochemical performance than that using a solid electrolyte containing the $Li_7P_3S_{11}$ crystal phase but prepared by mechanical milling. The better electrochemical performance was attributed to the formation of large electrode-electrolytes interfaces and favorable ion conductive pathways in the composite

cathode because of the small particle size of the solid electrolyte. These results clearly demonstrated the advantages of the sulfide solid electrolytes prepared by the facile liquid-phase synthesis.

5. The structural stability of the solid electrolyte containing the $Li_7P_3S_{11}$ crystal phase, prepared by liquid-phase, and used in the composite cathode of an all-solid-state cell, was analyzed after charge-discharge measurements with high charge-end voltages. The results indicated that the solid electrolyte did not suffer significant structural changes and that no degradation of the ionic conductivity can be expected after the charge-discharge processes at high charge-end voltages as 4.6 V vs. Li.

This thesis provides a new approach for the liquid-phase synthesis of sulfide solid electrolytes by using ultrasonic irradiation to enhance chemical reactivity in the solid-liquid system. Ultrasonic irradiation was demonstrated to be a useful technique to reduce the necessary time for the reaction, from days to minutes.

Moreover, this thesis provides deeper insights into the reaction mechanisms governing the liquid-phase synthesis. The author hopes that the better understanding of the formation mechanism of the $P_xS_y^{z-}$ thiophosphate anions that generally compose the structure of sulfide solid electrolytes, can be used as a guide on the designing of new reaction pathways for the synthesis of sulfide solid electrolytes with superior characteristics.

List of publications

(1) “Instantaneous preparation of high lithium-ion conducting sulfide solid electrolyte $Li_7P_3S_{11}$ by a liquid phase process”

Marcela Calpa, Nataly Carolina Rosero-Navarro, Akira Miura and Kiyoharu Tadanaga,

RSC advances, 2017, 7, 46499-46504.

(2) “Preparation of sulfide solid electrolytes in the $Li_2S–P_2S_5$ system by a liquid phase process”

Marcela Calpa, Nataly Carolina Rosero-Navarro, Akira Miura and Kiyoharu Tadanaga,

Inorganic Chemistry Frontiers, 2018, 5, 501-508.

(3) “Electrochemical performance of bulk-type all-solid-state batteries using small-sized $Li_7P_3S_{11}$ solid electrolyte prepared by liquid phase as the ionic conductor in the composite cathode”

Marcela Calpa, Nataly Carolina Rosero-Navarro, Akira Miura and Kiyoharu Tadanaga,

Electrochimica Acta, 2019, 296, 473-480.

Acknowledgments

I would like to express my deep gratitude to Professor Kiyoharu Tadanaga for giving me the opportunity to do this doctorate in his working group and for his fruitful guidance, suggestions and discussions.

I would also like to express my sincere appreciation to Assistant professor Carolina Rosero for her valuable guidance especially during the beginning of this work, and Assistant Professor Akira Miura for his valuable suggestions and helpful comments toward this Thesis.

I wish also to acknowledge the work of past and present members of the Laboratory of Inorganic Synthesis Chemistry at Hokkaido University.

I would also like to thank my family for their unconditional love, support and encouragement. They gave me everything I needed for this Thesis to be possible.

My last thanks to my husband Eduardo Narváez for having accompanied me the entire path to the end of this Thesis. Our scientific discussions, concerns and laughs have always encouraged me to be a better researcher.